NON-DESTRUCTIVE DEPTH PROFILING USING VARIABLE KINETIC ENERGY- X-RAY PHOTOELECTRON SPECTROSCOPY WITH MAXIMUM ENTROPY REGULARIZATION

by

James J. Krajewski

A dissertation submitted to the Faculty of the University of Delaware in partial fulfillment of the requirements for the degree of Doctor of Philosophy in Material Science and Engineering

Spring 2016

© 2016 James J. Krajewski
All Rights Reserved

ProQuest Number: 10157861

All rights reserved

INFORMATION TO ALL USERS
The quality of this reproduction is dependent upon the quality of the copy submitted.

In the unlikely event that the author did not send a complete manuscript
and there are missing pages, these will be noted. Also, if material had to be removed,
a note will indicate the deletion.

ProQuest 10157861

Published by ProQuest LLC (2016). Copyright of the Dissertation is held by the Author.

All rights reserved.
This work is protected against unauthorized copying under Title 17, United States Code
Microform Edition © ProQuest LLC.

ProQuest LLC.
789 East Eisenhower Parkway
P.O. Box 1346
Ann Arbor, MI 48106 – 1346

NON-DESTRUCTIVE DEPTH PROFILING USING VARIABLE KINETIC ENERGY- X-RAY PHOTOELECTRON SPECTROSCOPY WITH MAXIMUM ENTROPY REGULARIZATION

by

James J. Krajewski

Approved: ____

Darrin J. Pochan, Ph.D.
Chair of the Department of Materials Science and Engineering

Approved: ____

Babatunde A. Ogunnaike, Ph.D.
Dean of the College of Engineering

Approved: ____

Ann L. Ardis, Ph.D.
Senior Vice Provost for Graduate and Professional Education

I certify that I have read this dissertation and that in my opinion it meets the academic and professional standard required by the University as a dissertation for the degree of Doctor of Philosophy.

Signed: ____

Robert Opila, Ph.D.
Professor in charge of dissertation

I certify that I have read this dissertation and that in my opinion it meets the academic and professional standard required by the University as a dissertation for the degree of Doctor of Philosophy.

Signed: ____

Joshua Zide, Ph.D.
Member of dissertation committee

I certify that I have read this dissertation and that in my opinion it meets the academic and professional standard required by the University as a dissertation for the degree of Doctor of Philosophy.

Signed: ____

Ryan Zurakowski, Ph.D.
Member of dissertation committee

I certify that I have read this dissertation and that in my opinion it meets the academic and professional standard required by the University as a dissertation for the degree of Doctor of Philosophy.

Signed: ____

Juejun Hu, Ph.D.
Member of dissertation committee

ACKNOWLEDGMENTS

I have many people to thank for helping me complete this dissertation so late in life, without whom I would never have finished. First and foremost, I would like to thank Dr. Robert Opila, who has encouraged and motivated me with his enthusiasm, guidance and patience over the years. During my research studies, I have had the great fortune to learn from and be mentored by a great set of remarkable professionals including Drs. Conan Weiland, Dr. Jonathan Church, Dr. Anoop Mathew, Dr. Korhan Demirkan and Fang Fang. I would like to thank Dr. T. Gustafsson of Rutgers University for the MEIS results and the late Dr. Leszek S. Wielunski for RBS measurements who all helped me understand the analytical tools and computational algorithms needed to complete this work. Thank you Dr. Ryan Zurakowski for helping me understand Maximum Entropy and Bayesian Inference Process.

Technical support for sample synthesis from American Air Liquide and use of the National Synchrotron Light Source, Brookhaven National Laboratory, that was supported by the U.S. Department of Energy, Office of Science, Office of Basic Energy Sciences, under Contract No. DE-AC02-98CH10886.

I would also like to thank the members of my thesis committee, Professor Zide, Professor Zurakowski and Professor Hu for their guidance and time.

I would like to thank my family and friends for their support, especially for my wife, Linda, who encouraged me to embark on this journey and finish this project to finally earn my PhD.

TABLE OF CONTENTS

LIST OF TABLES viii
LIST OF FIGURES ix
ABSTRACT xiii

Chapter

1 INTRODUCTION 1

1.1 Background 1
1.2 Literature Search 9
1.3 Objective and Metrics for Success 10

2 EXPERIMENTAL 11

2.1 Sample Description – TiO_2 Films 11
2.2 Deposition Technique – Atomic Layer Deposition 11
2.3 Experimental Approach 12
2.4 Variable Kinetic X-Ray Photoemission Spectroscopy 13
2.5 Brookhaven National Laboratory Light Source - Synchrotron Parameters 14

3 ALTERNATE THIN FILM TECHNIQUES 17

3.1 Introduction - Why Alternate Techniques? 17
3.2 X-Ray Photoelectron Spectroscopy (XPS) 17
3.3 Angle Resolved Photoelectron Spectroscopy (AR-XPS) 19
3.4 Sputtered Angle Resolved X-Ray Photoelectron Spectroscopy (AR-XPS) 20
3.5 Auger Electron Spectroscopy (AES) 27
3.6 Average Thickness of TiO_2 layer. Å =34 Å (3.4nm) 30
3.7 Focused Ion Beam (FIB) & Transmission Electron Microscopy (TEM) 33
3.8 Variable Angle Spectroscopic Ellipsometry 38

4 METHODOLOGY 42

4.1 Introduction - Data Collection 42
4.2 Information Entropy 42

4.3 Slab Model 44
4.4 Depth Profile Regularization Technique 46

4.4.1 Transformation Matrix 48
4.4.2 Inelastic Mean Free Path - IMFP (λ) 50
4.4.3 Python Algorithms – Program Flow Diagrams 52
4.4.4 Specific Regularization Functions 54

4.5 Atomic Concentration Measurements for VKE Spectra 56

4.5.1 Measurement Parameters 57
4.5.2 Photoionization Cross-section and Sensitivity Factors 58
4.5.3 Peak Intensity Measurements 59

5 RESULTS AND DISCUSSION 64

5.1 Simulated Data 64

5.1.1 Initial Model – Data Generation 64
5.1.2 Beam Energies 68
5.1.3 Depth Profiles 69
5.1.4 Ent-model: Maximum Entropy 74
5.1.5 Initial Model – The Starting Point 78
5.1.6 Noise Level vs. Goodness of Fit 80
5.1.7 Selection of Regularization Parameter – Weighting Factor 82

5.2 Experimental Data: Thin and Thick Films 85

5.2.1 Comparison to Models (Carbon in/on Films) 85
5.2.2 Model Description 87
5.2.3 Thin TiO_2 Films (2.5 nm) 88
5.2.4 Thick TiO_2 Films (25nm) 90
5.2.5 Maximum Entropy Applied to Actual VKE-XPS Data 91
5.2.6 L-Curves-Residual Norm vs Solution Norm 91
5.2.7 Concentration Depth Profile of Measured Data 100
5.2.8 Limitations of the Technique 102

5.3 Conclusions 103

6 FUTURE WORK 105

6.1 Alternate Regularization Models 105

REFERENCES 107

Appendix

A PYTHON COMPUTER PROGRAMMING.. 115
B PERMISSION E-MAIL TO RE-USE DATA AND FIGURES…………….122

LIST OF TABLES

Table 4.1: IMFP values for simulated VKE data. All values in nm. 52

Table 4.2: Regularization functions used in this study. For all equations, n_{ij} represents the atomic concentration of element "i" at depth "j", m_{ij} is the atomic concentration of the initial model, and <n>is the average value. 56

Table 4.3: Photoionization cross-sections extrapolated from calculated values 58

Table 4.4: Peak positions for collecting XPS data for both the thick and thin TiO_2 films 60

Table 4.5: Calculated binding energies. 60

Table 4.6: Binding Energy Shifts........................ 61

Table 4.7: Transmission Function, T. 61

Table 4.8: Peak Areas - Thick TiO_2 Film. 61

Table 4.9: Normalized Areas – Thick TiO_2 Films 62

Table 4.10: Areas Thin TiO_2 Film, A. 62

Table 4.11: Normalized Areas Thin TiO_2 Film, [A]. 62

Table 4.12: Inelastic Mean Free Path, λ. 63

Table 4.13: Sigma, σ. 63

Table 4.14: Photoemission of the reference material, R. 63

Table 5.1: χ^2 results different regularization routines for thin (2.5 nm) and thick (25 nm) TiO_2 films deposited on silicon 95

LIST OF FIGURES

Figure 1.1: X-Ray energy (hv) = Kinetic Energy (Ek) + Binding energy (Eb) + Work Function. 2

Figure 1.2 Angle Dependence XPS showing different depth probing. 4

Figure 1.3: VKE-XPS with three input x-ray energies and constant angle. 2KeV(red), 4KeV (green) and 6KeV (black) and depth excited atoms in respective colors. λ = IMFP. 5

Figure 2.1 Atomic Layer Deposition. 12

Figure 2.2: Comparison of Angle Resolved -XPS, showing the shorter IMFP (λ) vs. Variable Kinetic Energy-XPS showing the variable and longer IMFP. 14

Figure 2.3: Beamline X24A at the National Synchrotron Light Source at Brookhaven National Lab (BNL). Photos: JJK 16

Figure 3.1: Angle Dependence XPS showing different depth probing. 20

Figure 3.2: C1 signal from the entire sequence of Sputtered AR-XPS. 22

Figure 3.3: Si substrate signal - entire sequence of Sputtered AR-XPS. 22

Figure 3.4: Ti signal from the entire sequence of Sputtered AR-XPS 23

Figure 3.5: Oxygen signal - entire sequence of Sputtered AR-XPS. 23

Figure 3.6: Average Thickness of TiO_2 layer: Å=34 Å (3.4nm) 24

Figure 3.7: Sputtering of the 25nm film from the surface (red) to below the surface (blue) of Si2P, C1s, O1s and Ti2P peaks. 26

Figure 3.8: Angle dependence of sputtering of ~25nm film. Dark curve is 24° (surface sensitive) and the red curve is 81° (depth sensitive). Note the carbon presence throughout the film in upper left plot. 27

Figure 3.9: Auger process. a) Illustrates the generation of a core state electron hole, 1s level (now an unstable atom) b) Hole filled by higher energy electron (2p orbital) and this energy difference can be coupled to another 2p electron, which will be emitted and detected, if the energy exceeds the orbital binding energy. 28

Figure 3.10: Auger Spectroscopy depth profile of thin (~ 2.5nm) TiO_2 film. 29

Figure 3.11: RBS layer model. 30

Figure 3.12: RBS raw data of the “thin” TiO_2 film. 32

Figure 3.13: RBS data of TiO_2 thin film fitted with a model for 2.586nm thick film (simulation solid line). 33

Figure 3.14: FIB (top) TEM (bottom) - University of Delaware, Newark, Delaware, Photo JJK. 34

Figure 3.15: Schematic of Focused Ion Beam and TEM principles. 35

Figure 3.16: Top: FIB/TEM Sample Mount. Bottom: Scanning Electron Microscopy image of an FIB trench being carved to produce a small sample of the TiO_2 film for TEM imaging. Photo JJK. 36

Figure 3.17: TEM image of the thin (~3nm) TiO_2 film. 37

Figure 3.18: Schematic of the Variable Angle Spectroscopic Ellipsometry principles. 38

Figure 3.19: VASE data Top: Ψ plotted against wavelength. Middle Δ plotted against wavelength. Bottom: Optical constant vs. eV. 41

Figure 4.1: AR-XPS slab model. λ= Inelastic Mean Free Path (IMFP) 45

Figure 4.2: VKE-XPS Slab model: Non-destructive depth sensitive composition information on a sample by detecting excited electrons from deeper and deeper into the film with increasing beam energy. 47

Figure 4.3: Flow of program logic in reconstructing the depth profile of the TiO_2 on Silicon from VKE-XPS data and Maximum Entropy Algorithm. 53

Figure 4.4: Optimizing N-matrix for depth sensitive concentration. 54

Figure 5.1: Top: Initial Homogeneous Model of 7.5nm film. Bottom: 7.5nm simulated film for Ti2p, O 1s and Si 1s. Ref.82. 65

Figure 5.2: VKE-XPS Relative Intensity for simulated films (points), and the resulting regularization results (lines). For "Ent-Model", the initial model is shown in dashed lines. Ref 82. 67

Figure 5.3: Dependence of "Goodness of fit",χ^2, on number of beam energies used for VKE-XPS. Ref. 82. 69

Figure 5.4: Depth profiles resulting from Ent-Mod and TVA regularization routines (solid lines). Initial Model: Dotted lines. Simulated films: Dashed lines. Ref. 82. 72

Figure 5.5: Depth profiles resulting from Curves and Slopes regularization routines (solid lines). Simulated films: Dashed lines. Ref. 82. 73

Figure 5.6: Dependence of χ^2 on the initial model thickness for the Ent-mod performed on a simulated 7.5 nm thick film. Ref. 82. 74

Figure 5.7: Plot of fractional composition for the initial model thickness of 3nm for the Ent-model routine performed on a simulated 7.5 nm thick film. 76

Figure 5.8: Plot of fractional composition of the initial model thickness of 8nm for the Ent-model routine performed on a simulated 7.5 nm thick film. 76

Figure 5.9: Plot of fractional composition for the initial model thickness of 10nm for the maximum entropy routine performed on a simulated 7.5 nm thick film. 77

Figure 5.10: "Slopes" depth profile from 7.5nm simulated TiO_2 film. Homogeneous initial model (pluses in blue); 8nm 1:1 Ti:O initial model (diamonds); 2 nm 1:1 Ti:O initial model (crosses); Simulated film structure (dash line). Ref. 82. 79

Figure 5.11: "Goodness of fit",χ^2, results for the different regularization functions at different simulated film thicknesses. Ref. 82. 83

Figure 5.12: Goodness of fit, χ^2, for profiles produced using a 7.5 nm generated TiO_2 film at all values for α. The α values selected by the program are highlighted by the outlined symbol. Ref. 82. 84

Figure 5.13: Photoemission of 2.5nm TiO_2 film on Si collected at various beam energies. Ref. 82. 86

Figure 5.14: Photoemission of 25nm TiO_2 film on Si collected at various beam energies. Ref. 82. 87

Figure 5.15: Atomic concentration v. depth for **2.5** nm TiO_2 films on Si. Error bars are estimated from the signal to noise ratio of the photoemission peaks. 89

Figure 5.16: Atomic concentration v. depth for **25** nm TiO_2 films on Si. Error bars are estimated from the signal to noise ratio of the photoemission peaks. 90

Figure 5.17: L-Curve for thin (2.5nm): carbon modeled on the surface 93

Figure 5.18: L-Curve for thick (25nm): carbon modeled on the surface 93

Figure 5.19: L-Curve for thin (2.5nm): carbon modeled in the film. 94

Figure 5.20 L-Curve for thick (25nm): carbon modeled in the film. 94

Figure 5.21: Depth Profiles found using Ent-model regularization. Model:1nm C on surface of a 2.5nm homogenous Si-O:Ti:O film. χ^2=0.660 96

Figure 5.22: Depth Profiles found using Ent-model regularization. Model: C thru film-2.5nm - homogenous Si-O:Ti:O film. χ^2= 0.445 96

Figure 5.23: Depth Profiles – using TVA regularization on 2.5nm film. No initial model. χ^2= 0.27 97

Figure 5.24 Ent-model: 1 nm C on surface- 25nm homogenous Si-O:Ti:O film. χ^2= 0.075. Ref. 82. 98

Figure 5.25: Ent-model: C thru film-25nm - homogenous Si-O:Ti:O film. χ^2=0.060. Ref. 82. 98

Figure 5.26: TVA regularization 25nm film.χ^2=0.058. Ref. 82. 99

Figure 5.27: Measured and calculated VKE data for Si-O signal from 25 nm film. The error bars are estimated from the signal to noise ratio in the data. Ref. 82. 102

Figure 6.1: Hill Function on left; Logistic Function in center; Slopes Regularization used in this VKE-XPS study [106]. 105

ABSTRACT

This study will describe a nondestructive method to determine compositional depth profiles of thicker films using Variable Kinetic Energy X-ray Photoelectron Spectroscopy (VKE-XPS) data by applying proven regularization methods successfully used in Angle-Resolved X-ray Photoelectron Spectroscopy (AR-XPS). To demonstrate the applicability of various regularization procedures to the experimental VKE-XPS data, simulated TiO_2/Si film structures of two different thicknesses and known compositional profiles were "created" and then analyzed. It is found that superior results are attained when using a maximum entropy-like method with an initial model/prior knowledge of thickness is similar to the simulated film thickness. Other regularization functions, Slopes, Curvature and Total Variance Analysis (TVA) give acceptable results when there is no prior knowledge since they do not depend on an accurate initial model. The maximum entropy algorithm is then applied to two actual films of TiO_2 deposited on silicon substrate. These results will show the applicability of generating compositional depth profiles with experimental VKE-XPS data. Accuracy of the profiles is confirmed by subjecting these actual films to a variety of "alternate" analytical thin film techniques including Sputtered Angle Resolved Photoelectron Spectroscopy, Auger Electron Spectroscopy, Rutherford Backscattering Spectroscopy, Focused Ion Beam Spectroscopy, Transmission and Scanning Electron Spectroscopy and Variable Angle Spectroscopic Ellipsometry. Future work will include applying different regularizations functions to better fit the MaxEnt composition depth profile other than those described in this study.

Chapter 1

INTRODUCTION

1.1 Background

X-ray photoelectron spectroscopy (XPS) is a surface sensitive that can be used to study depth profiles and chemical bonding states of thin films. TiO_2 is being used in a variety of applications such as electronics, sensors, antireflection coatings and photo catalysts due to its high dielectric constant, high refractive index, good optical transmittance and will be the film of choice in this study [1, 2]. Consequently, the need for exact layer thickness measurements and chemical depth profiles of these unique films is becoming a common requirement for the thin film and coatings industry. As a consequence, there is a strong interest in developing a quantitative non-destructive method to verify chemical composition and concentration throughout the film. With the ever-increasing cost and complexity of these devices, a technique is needed to determine if the desired film has the correct profile, desired chemical composition and structure long before the costly fabrication process is completed. One techniques that lends itself to these requirements is XPS.

XPS involves flashing monochromatic X-rays on a sample and depending on the energy of the x-rays, atoms in the sample are photo-ionized, i.e. atoms at some depth in the sample receive enough energy from the x-rays that it emits electrons that can migrate through and out of a sample to be detected by an energy spectrometer. This detector measures the kinetic energy distribution of these emitted photoelectrons. Computer software analyzes the data and normalizes the intensities of the elemental

peaks of the spectrum that are used to determine atomic composition, bonding chemistry and concentration depth profiles within the sampling volume of the film. See figure 1.1 for a schematic of the photoionization process.

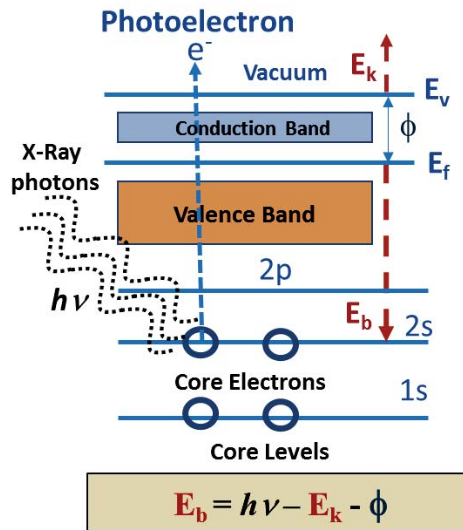

Figure 1.1: X-Ray energy (hv) = Kinetic Energy (Ek) + Binding energy (Eb) + Work Function.

The relationship between the electron kinetic energy E_k, measured in the spectrometer for a given binding energy E_b that is characteristic of the particular element and work function is denoted as ϕ,, is given by the following relationship and discussed further in section 3.2:

$$Eb = (h\nu - Ek - \phi) \quad (1.1)$$

One version of XPS is *soft* x-ray photoelectron spectroscopy, or low energy XPS, also named Angle-Resolved X-ray Photoelectron Spectroscopy (AR-XPS). It

can determine chemical depth profiles and compositions of very thin films by varying the detector angle in capturing the excited photoelectrons, see Figure 1.2. AR-XPS combined with a regularization technique has been successfully employed in industry to non-destructively measure the compositional depth profile of various *thin* film structures of several nanometers. [3, 4, 5, 6, 7, 8]. Further knowledge of thicker films will be done by sputtering (removing) layer by layer of the film with intermittent measurement of the escaping photoelectrons. This technique can give adequate results about film thickness but is suspect for depth profiling due to the complicated the spectrum resulting from inherent damage that the sputtering ions can do to the sample through atomic rearrangements, uncontrolled secondary chemical reactions or ions embedding in the film.

Due to the limited nature of the photoelectron inelastic mean free path (IMFP), XPS data analysis can result in producing valuable information about the chemical profiles and interface states in the film. The IMFP is the length that an electron travels before being scattered inelastically. Too short and it will not have enough energy to escape the film and be detected. The IMFP is directly dependent on the incoming x-ray energy, i.e. the higher the kinetic energy, the longer is the electron travel length before it loses energy. It can still be detected just not at that energy. A constant input x-ray energy allows for generating depth profiles of relatively thin films by changing the angle of detection. A shallow take-off angle of x-rays (at constant energy) samples atoms near the surface of the film, while a steeper angle of collection (again at constant energy) penetrates a little deeper into the film, see Figure 1.2. Note the different depths, d, from the surface of the film that can be detected by varying the angle from 90° (deeper into the film) to 20° (more surface sensitive).

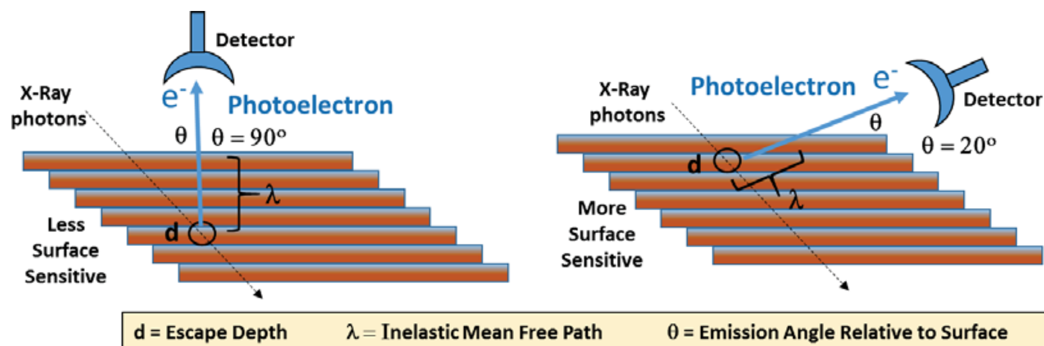

Figure 1.2 Angle Dependence XPS showing different depth probing.

AR-XPS is basically a surface technique (2-4nm into the film) due to low photoelectron kinetic energies (short IMFP). Because the electrons that were originally excited near the surface or at some shallow depth in the film lose energy during their path out of the film, this torturous path through the sample complicates the data analysis for profile determination and will be a focal point of the modeling in this study (see section 3.3 for more details).

Soft X-Ray Photoelectron Spectroscopy, with $h\nu$ energies in the 1.2-1.4KeV range can only probe surface and near surface atoms but Hard X-ray Photoelectron Spectroscopy (HA-XPS), with its variable excitation energies, $h\nu$, spans the range from 1-6KeV. HA-XPS can excite atoms deep in the film and because of the longer IMFP can generate chemical profiles in films up to 30nm, see figure 1.3. [9, 10, 11, 12, 13].

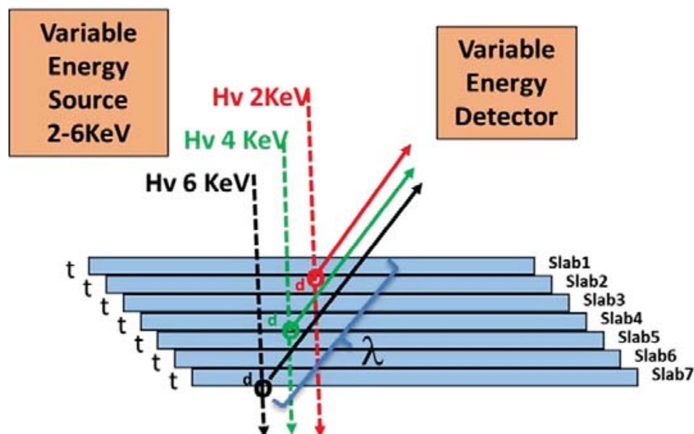

Figure 1.3: VKE-XPS with three input x-ray energies and constant angle. 2KeV(red), 4KeV (green) and 6KeV (black) and depth excited atoms in respective colors. λ = IMFP.

A powerful source for HAXPES is a synchrotron light source at the Brookhaven National Labs, which offers exceptional brightness, tunable beam energy, and high energy resolution. Here varying the kinetic energy of the x-rays leads to collecting spectra from excited atoms deep in the film and generating depth sensitive composition information, without destroying the valuable sample Figure 1.3. However, to date VKE-XPS analysis has not focused on TiO_2 and is usually *qualitative* in nature, i.e. no modeling of the chemical concentrations and depth profiles [14, 15, 16].

This work expands on the established low energy XPS technique to include higher energies and more robust modeling. Regardless of the type of XPS technique implemented, no unique reconstruction model exists to correctly transform the raw data directly into composition depth profiles since there are many depth profiles that are possible solutions to the collected data. This implies that simple curve fitting of the data such as least squares technique is not sufficient to determine an accurate

concentration profile. The techniques to study thicker films using VKE-XPS also have the same limitation of not directly translating the raw XPS data into a unique chemical depth profile. Since quantification of VKE-XPS spectra is complicated by the relationship between the intensity of a photoelectron signal and the depth from which it originates, the distribution of species with depth can greatly affect measured intensity ratios using standard quantification techniques [17, 18, 19, 20,21].

XPS analysis involves solving an ill-posed problem where there are a high number of depth profile configurations that fit the VKE-XPS data. Maximum Entropy (MaxEnt) methodology is applied to the VKE-XPS data coupled with a variety of regularization techniques (see below) to model the data and generate a viable depth profile of relatively thick films. MaxEnt is a powerful data resolution tool with principles rigorously based on logic and statistical theory. Any prior knowledge of the film i.e. thickness, composition or other parameters can be included as constraints in the model but are not necessarily needed. The MaxEnt methodology is a technique used to confidently reconstruct the most probable depth profile from noisy and limited XPS data. The Principle of MaxEnt states "*Subject to known constraints, the probability distribution (depth profile) that best represents the current state of knowledge (what is known) but leaves the largest uncertainty (assume nothing about what is unknown) is the depth profile with the least assumptions"* [21].

This MaxEnt process is applied through a variety of regularization techniques, an introduction of known constraints (regularizations or prior knowledge) to limit the range of possible solutions to those based in reality. Using a regularization function, balances the best fit to the data (keep a high "goodness of fit (χ^2) with minimal

smoothing) without over fitting the data (keeping the complexity of the data without fitting the noise).

This analytical tool has been successfully applied to clarifying and analyzing data from radio telescopes, Laplace transforms, photo correction spectroscopy, particle light scattering, x-ray crystallography, electrospray mass spectroscopy, pulse fluorescence measurements, electron spectroscopy and NMR [22].

The technique of probing multilayer high-k dielectric TiO_2 films with VKE-XPES and analyzing the data with a regularized Maximum Entropy Algorithm with cross-correlation to other destructive depth profile techniques (discussed later) will lead to understanding the key constraints and critical limitations of the model as applied to more complex film structures. Ultimately, the goal is to develop a reliable and more accurate *non-destructive* method to determine compositional depth profiles of thicker films without relying on additional input from other destructive or less accurate depth profiling techniques.

This work will initially characterize the two TiO_2 films with a variety of alternate thin film characterization tools with the goal of reaching a consensus on the thickness of the two films and elemental composition. These thickness measurements and elemental compositions will aid in supplying additional "prior' information (regularizations) to the depth profile model. These alternate techniques will also be studied to outline the advantages and disadvantages of each techniques and compare them to the VKE-XPS. The techniques will include Angle Resolve – XPS (AR-XPS), Auger Spectroscopy (AES), Rutherford Back Scattering Spectroscopy (RBS), Variable Angle Spectroscopic Ellipsometry (VASE), Focused Ion Beam (FIB) and

Transmission Electron Microscopy (TEM) to fully characterize these thin films (see Chap. 3).

It is common to have some prior knowledge of the film (chemical elements, approximate thickness, substrate preparation, etc.) and this allows for the technique to optimize the methodology and model. As stated earlier, this optimization will allow for the calculation of new, complex, multi-element chemical depth profiles by assigning a distribution of possible profiles, subject to given constraints (regularizations), and then maximizing the information entropy to resolve any ambiguity in the data.

Initially the MaxEnt methodology will be applied to a fully understood *simulated* spectra comparing different regularization methods. Then, using the optimized parameters acquired from the simulated spectra, apply the technique to actual VKE-XPS data of two TiO_2 films. The scientific and technological impact of non-destructive characterization of complex TiO_2 dielectric films is critical to understanding the high k-dielectric as a viable substitution to SiO_2.

XPS data processing is based in the science of uncertainties and probability theory, that is, there is always a "trade-off" between uncertainty of the profile and depth resolution. There are a variety of algorithms with various pros and cons that can be used to achieve better resolution of the data. The algorithms range from least-squares fitting to the Tikhonov regularization to maximum entropy methods [19]. A good review of the techniques and their strengths/weaknesses can be found in the paper by Paynter [23].

The commonly used depth profile technique for thin films combines Angle Resolved (AR-XPS) data and a maximum entropy model to convert angle resolved

data into a profile of “concentration vs. depth” [19, 21, 24, 25, 26, 27]. Reconstructing the depth profile from the angle-resolved data is a classic example of an under-determined problem, i.e. the data collected is insufficient to identify the ‘correct” or “actual” depth profile from a distribution of all possible profiles. The challenge is to select the best reconstruction that would fit the ARXPS data (or VKE-XPS data in this study) by minimizing any artificial correlations in the data while making only minimal assumptions about the sample structure.

MaxEnt model still has resolution issues because there are many solutions to either the angle dependent or energy dependent data that produce broad interfaces. This can be crucial in understanding a 3nm film where the interface may dominate the structure. This effect is incorporated in the model assumptions that the surface is ‘smooth” and any roughness would negatively affect the interface signal. The model also uses a three-point smoothing package, which also broadens the interface. Perhaps a different regularization function, such as a sigmoidal Hill Function would be more applicable to films with sharp interfaces (common in ALD films) and step function concentration gradients (see Future Work in Chapter 6).

Ultimately, this research will produce an accurate depth profile, as confirmed by other more destructive techniques that reflect the chemical composition, film thickness and bonding states located near the interfaces.

1.2 Literature Search

Much work has been done in the area of VKE-XPS but none specifically addressing TiO_2 thin films with VKE-XPS and correlating the results with other analytical techniques. The characterization of TiO_2 films has been studied extensively describing the deposition techniques, energy bandgaps, and electron affinity, leakage

current and dielectric properties [28, 29, 30, 31, 32, 33 34, 35, 36, 37, 38, 39, 40, 41, 42, 43, 44, 45, 46, 47, 48, 49, 50]. Likewise, there has been extensive research done on TiO_2 films with Variable Angle Spectroscopic Ellipsometry [51, 52, 53, 54, 55, 56], Rutherford Backscattering Spectroscopy [57] and Focused Ion Beam [58, 59, 60].

The Maximum Entropy Model [20, 21, 24, 61, 62, 63, 64, 65, 66, 67] has been applied to a wide variety of data resolution projects and is beginning to be applied to the peak resolution in VKE-XPS and HA-XPS [9, 10, 11, 12, 14, 15, 68, 69, 70, 71, 72, 73, 74, 75, 76, 77, 78, 79]. We will build on this past research and apply the Ent-model to HA-XPS for thin TiO_2 dielectric films. Cumpson [19] also reviewed the limitations of depth profile reconstructions from angle resolved photoemission. It was noted that the quality of the depth resolution was limited to approximately twice the escape depth due to poor signal strength beyond 2λ.

1.3 Objective and Metrics for Success

The objective of this work is to use high energy XPS and maximum entropy regularization to develop a procedure to accurately determine a chemical depth profile that correlates with measurements from a variety of analytical techniques of the same thin (3nm) and thick (25nm) TiO_2 thin films. As stated earlier, some of these alternate analytical techniques are destructive in nature thus not allowing for real time measurements in the electronics fabrication “clean room” environment. Using the data generated by these other techniques (thickness, chemical constituents, uniformity) allow for the conformation of the depth profile and to use this information as “prior” knowledge into the optimization of the model.

Chapter 2

EXPERIMENTAL

2.1 Sample Description – TiO_2 Films

Using atomic layer deposition (ALD), two TiO_2 films of approximately 3nm and 25nm thicknesses were deposited on (100) silicon substrates, with no prior cleaning or acid stripping of any native oxide, typically 1-2nm. This interface oxide is important to measure and model because it is important to the ultimate understanding of the film's properties such as adhesion, delamination or substrate leakage current. [1]. The films were not annealed after deposition so any intrinsic strain or defects as the result of the deposition remain present. The films were stored in an Argon purged glove box but no special treatment was given to the samples arriving in the lab to prevent ambient oxidation.

2.2 Deposition Technique – Atomic Layer Deposition

The TiO_2 films were made from a proprietary, organic precursor using Atomic Layer Deposition (ALD) system. ALD is a chemical gas phase method involving sequential saturating, self-limiting surface reactions on to a substrate. It involves alternate pulses of precursors separated by purge steps allowing for the detailed control of layer thickness, see figure 2.1. ALD has several advantages over other more energetic techniques including accurate thickness control at the monolayer level, large, uniform area and batch capabilities, and excellent conformity including good reproducibility, ability to use precursors with high mutual reactivity, and the ability to

deposit high quality films at low deposition temperatures [40, 80]. These advantages make ALD the chosen method for depositing these high- k dielectrics. Details of the precursors and exact deposition chamber specifications are proprietary.

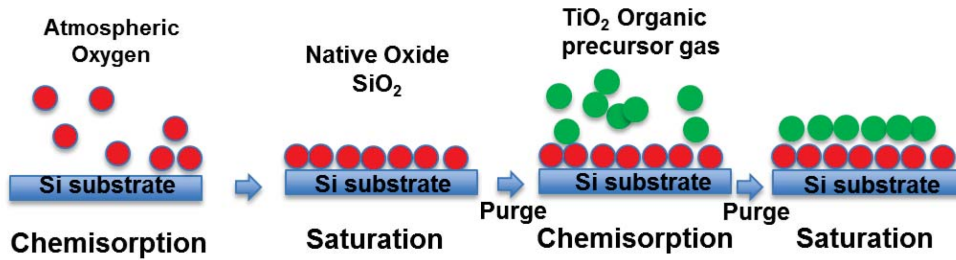

Figure 2.1 Atomic Layer Deposition.

2.3 Experimental Approach

We plan to accurately measure a compositional depth profile of two TiO_2 films using a series of analytical techniques and compare the results to VKE-XPS model and the regularized maximum entropy algorithm. Many of these depth profiling techniques are destructive because sputtering off layers of the film needs to be performed for further depth analysis. Rutherford Backscattering Spectroscopy (RBS) can also give non-destructive profiles but they have limited sampling depths and are better at detecting atoms with greater mass (see chapter 3).

It's important to accurately know the thickness of the film in order to optimize the maximum entropy model, so we will use RBS, Variable Angle Spectroscopic Ellipsometry (VASE) and Focused Ion Beam (FIB), Transmission Electron Microscopy (TEM) and Scanning Electron Spectroscopy (SEM) to measure thickness and other input parameters. Once the model parameters have been optimized using known thicknesses, this technique can be applied to unknown film thicknesses to

generate accurate compositional depth profiles. The extremely destructive technique of Focused Ion Beam will be used to visually measure the thickness and uniformity of the interface by raster an ion beam across the sample to sputter a deep trench for measurement and fabricate a small, thin sliver of the film for TEM cross-sections analysis (see figure 3.17). This will be compared to the depth profile generated by VKE-XPS. A comparative analysis of all of these techniques to VKE-XPS output will be described throughout this work.

2.4 Variable Kinetic X-Ray Photoemission Spectroscopy

Variable Kinetic X-Ray Photoemission Spectroscopy (VKE-XPS), also called Hard X-Ray Photoelectron Spectroscopy (HA-XPS), is a technique that follows the same concept as AR-XPS except the collection angle is held constant while the data is collected as various energies. It can probe up to a 30 nm thick film nondestructively to generate an accurate depth profile which is impossible by other techniques such as AR-XPS and Sputtered AES due to their near surface sensitivity, see figure 2.2.

Higher energy (hard) XPS technique can determine the uniformity of thickness and the chemical composition of thicker films. As opposed to low energy (soft) XPS which is limited to surface studies with small escape depths of the excited electrons, Hard X-Ray Photoelectron Spectroscopy (HAXPS or VKE-XPS) allows for studying depth profiles of thicker films, in the range from 20 to 30 nm and thicker. Typical low energy XPS has kinetic energies in the soft x-ray regime on the order of 15 to 1500 eV, as opposed to HAXPS generated by synchrotron-based light sources on the orders of 2000-6000 eV. Both techniques can use the maximum entropy algorithm for data clarification, but varying the kinetic energy (VKE-XPS) is an excellent technique to study buried interfaces within the film stack [81].

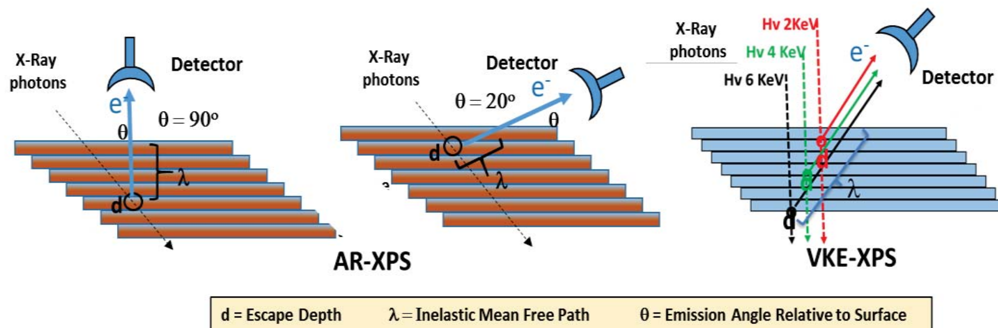

Figure 2.2: Comparison of Angle Resolved -XPS, showing the shorter IMFP (λ) vs. Variable Kinetic Energy-XPS showing the variable and longer IMFP.

In contrast, to AR-XPS, which varies the take-off (collection) angle of the escaping electrons thus changing the sampling depth, depth profiling in VKE-XPS is achieved by varying the excitation x-ray energy at a constant photoelectron emission angle (See eq. 1). Since the inelastic mean free path of the electron is dependent on the electron kinetic energy, increasing the x-ray energy will increase the kinetic energy of the emitted electron i.e., from different escape depths. Electrons emitted from the sample greater that IMFP are likely to scatter inelastically than to escape the film without energy loss [81].

2.5 Brookhaven National Laboratory Light Source - Synchrotron Parameters

VKE-XPS measurements on the TiO_2 films were performed at the National Institute of Standards and Technology (NIST) beamline X24A at the National Synchrotron Light Source at Brookhaven National Laboratory, New York. Beam energies between 2 and 6 keV are available, selected using a double crystal Si (111) monochromator. The beamline contains a pre-monochromator vertically collimating mirror and entrance slits to both obtain optimal energy resolution and reduce the

thermal load on the monochromator. The monochromator is a water-cooled constant-offset double Si (111) crystal design. The post-monochromatic beam is horizontally focused using a toroidal mirror and the beam spot is defined by exit slits, typically 0.5 mm horizontally and vertically, just upstream of the analysis chamber [81]. The beamline end-station is equipped with a hemispherical electron detector mounted at 90o with respect to the beam axis. Spectra were recorded using a pass energy of 200 eV and a 0.3 mm detector aperture, with the sample mounted at a 5o angle between sample normal and detector. Under these conditions, energy resolution was found to be limited by the X-ray line width of 0.27 eV. An Ag specimen was used to calibrate the energy scale of the detector. To account for thermal changes in the first monochromator crystal, a three-axis feedback system drives monochromator and mirror alignment to maintain a constant beam position; however, the changing second mirror angle results in beam focus drift along the beam axis. Pressure in the end-station was maintained below 2 x 10-8 Torr. All spectra for each sample at a given energy were acquired in alternate cycles to account for any drift in X-ray intensity and energy [82].

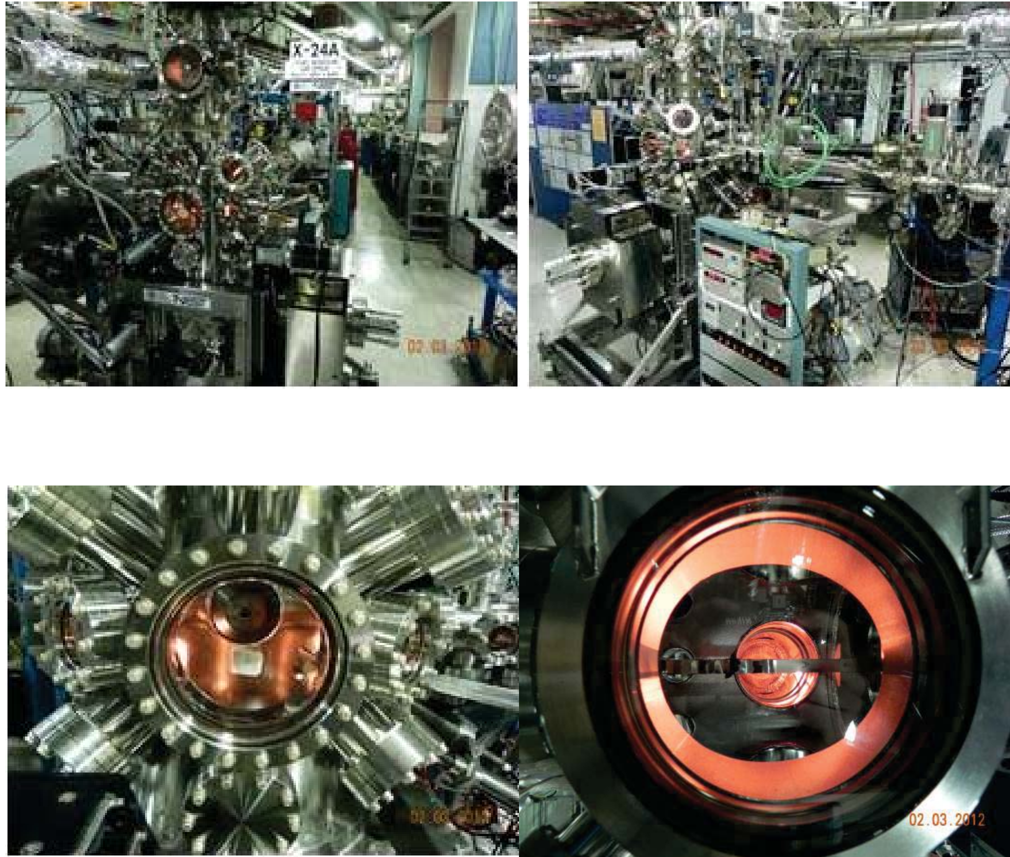

Figure 2.3: Beamline X24A at the National Synchrotron Light Source at Brookhaven National Lab (BNL). Photos: JJK

The left upper photo in figure 2.3 is directed at the sample chamber to the light source (storage ring) and the upper right photo is the ring back to the sample chamber. It can be seen that the system is a complex array of chambers, feedthroughs, valves, pumps, gauges, meters, detectors with computers controlling everything from pumping limits to sample loading and manipulation. The lower photos are close-ups of the sample chamber with the sample mounted in the center. All data collection software is owned and maintained by the NIST/BNL staff.

Chapter 3

ALTERNATE THIN FILM TECHNIQUES

3.1 Introduction - Why Alternate Techniques?

Alternate thin film thickness techniques are used to confirm the TiO_2 film thickness deposited in developing a model for application of the maximum entropy regularization as well as compare it to the accuracy of the other regularization functions studied in this work. Since this study develops a straight-forward methodology to identify key parameters in determining chemical depth profiles of an unknown film, it is important to fully characterize a set of "standard" films so as to determine through modeling the key parameters for the maximum entropy technique. In this light, we use various analytical techniques, many destructive, to verify the thickness of the two films studied in this work and for comparison, determine the chemical composition of the film.

These techniques will include Auger Electron Spectroscopy (AES), Rutherford Backscattering Spectroscopy (RBS), Variable Angle - Spectroscopic Ellipsometry (VASE), Focused Ion Bean Spectroscopy (FIB) and Transmission Electron Spectroscopy (TEM) and Scanning Electron Spectroscopy (SEM).

3.2 X-Ray Photoelectron Spectroscopy (XPS)

X-ray photoelectron spectroscopy detects the excitation of the electrons from a core level atom excited by incident x-ray photon of energy, $h\nu$, and is then analyzed by the electron spectrometer, plotting the intensity of the detected electron versus

electron energy see figure 1.1). The kinetic energy (E_k) of the electron is measured by the spectrometer and is dependent on the photon energy of the incident x-ray source and is not an intrinsic property of the material. What specifically identifies the electron is the binding energy (E_b). The binding energy is equal to the photon energy (incident) minus the kinetic energy (measured) minus the specific work function (ϕ) of the spectrometer.

$$E_b = h\nu - E_k - \Phi \tag{3.1}$$

This equation shows that the binding energy of the core electrons can be determined using monochromatic x-rays and all parameters on the right side of the equation are measured [83]. These excited photoelectrons in the film travel a short distance before undergoing inelastic scattering and all electrons with a binding energy less than the photon energy will be in the spectrum. Those electrons, which are excited and escape the film with minimal energy loss, contribute to the characteristic peaks in the spectrum and those that undergo inelastic scattering have some energy loss thus contributing to the background. After emission the atom is ionized and must relax by emitting an x-ray photon (x-ray fluorescence) or an Auger electron. One aspect of photoelectron spectroscopy is the intensity of this photoelectron signal (I) as a function of sample depth (z) and can be approximated by:

$$I = Io \exp(-z/\lambda \cos\theta) \tag{3.2}$$

where θ = the collection angle of the emitted photoelectron with respect to the surface normal and λ is the attenuation length of the photoelectrons in the thin-film [8, 21]. At

these low energies, typical escape depths, range from 1 nm to 3 nm. Chemical shifts occur in the photoelectron spectroscopy due to initial state affects and to relaxation effects of the electrons nearby. These effects must be taken into account when analyzing the data. Additional peaks in the spectrum can be due to shake up, multiplet splitting, and plasmons.

3.3 Angle Resolved Photoelectron Spectroscopy (AR-XPS)

As mentioned earlier, a very common analytical technique to measure “thin” films is Angle-Resolved Photoelectron Spectroscopy (AR-XPS). AR-XPS is a quantitative spectroscopic technique that can determine the elemental composition, empirical formula, chemical and electronic states and spatial distribution of the materials in three dimensions within very thin film. XPS data is acquired by exposing the sample to x-rays while at the same time measuring the kinetic energy and number of electrons (intensity) that escape from the top few nanometers of the material. Angle resolved XPS relies on the fact that x-rays penetrate through the film in the μm range and the photoelectron escape in the nm range; at low collection angles most of the detected electrons originate near the surface whereas at higher angles more of the photoelectrons will originate from atoms deeper within the film [1, 19, 21, 84]

As illustrated in the figure 3.1, we can exploit this fact that photoelectrons travel only a short distance in the film, called the attenuation length, and this attenuation length establishes the sample depth of the photoelectron spectroscopy. So collecting spectra with a normal collection angle (left side of figure 3.1), the specimen is probed more deeply. Collecting the photoelectrons with a glancing angle (right side of figure 3.1), the spectrum reflects the outer surface of the specimen. This is shown in figure 3, where the same x equals the attenuation length for the photoelectron, but

depending on the collection angle, the electrons originate from different depths, d, within the sample. The geometry of the XPS system along with accurate goniometers ensure that the sampling depth $d_1>d_2$ when $\theta_1<\theta_2$. The intensity of the photoelectron signal as a function of depth is related to the cosine of the collection angle [20].

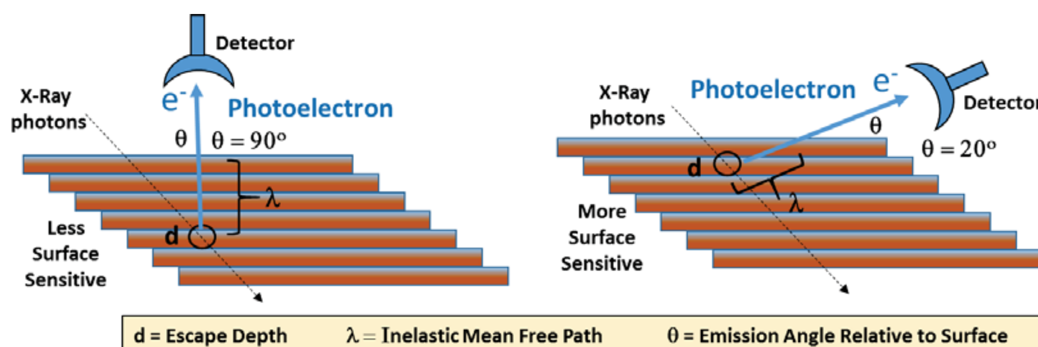

Figure 3.1: Angle Dependence XPS showing different depth probing.

3.4 Sputtered Angle Resolved- X-Ray Photoelectron Spectroscopy (AR-XPS)

College of Nanoscale Science and Engineering - University of Albany

Relja Vasic, Gangadhara Raja Muthinti, Alain Diebold

Low energy spectroscopies result in shallow detection depths, so a depth profile is usually generated by ion sputtering atomic layers off the material. This destructive composition-depth profiling technique uses ion bombardment to remove thin sections of the sample, then the sample is probed with XPS. The sample is then ion sputtered again to remove some known amount of surface layers and the XPS collection process is repeated. The XPS system used in this study has a fixed area detector while the sample is fixed on horizontal sample stage. In sputtering depth profiling, the sequence is: measure-sputter-measure-sputter, in the "angle integrated mode" where area detector collects the photoelectrons in different angles in 16 steps of 3.75^o between 24.88^o and 81.13^o. Initially, sputtering rates must be calculated for a

given energy through the TiO_2 film. All XPS measurements were performed on the TiO_2/Si sample by Thermo VG Scientific Theta Probe lab tool, with a monochromatized Al Kα source at 1486.7 eV. The 2-dimensional detector in the Thermo-VG Scientific XPS system allows simultaneous collection of spectral data from all angles without tilting the sample. The angle dependent depth profile for the TiO_2 film was computed using Avantage software. This technique produces a satisfactory depth profile but may result in implantation of the sputtering species or mixing of surface atoms in the film, typical drawback of any sputtering technique.

The ARXPS depth profiles are similar to the results of Variable Angle Spectroscopic Ellipsometry indicating the total thickness is about 6 nm including the native SiO_2 layer. The average thickness of the TiO_2 layer is 3.4nm, see figure 3.6. As reported from the University of Albany, the film is mostly composed of Ti and O, except the presence of a small amount of carbon that was detected on the surface. The carbon contamination is shown to be present on the surface of the TiO_2 film because the C1 signal decreases with continued Ar^+ ion sputtering but the carbon signal disappears after a few sputter cycles (figure 3.2).

The SiO_2 is present near the surface with a 4eV chemical shift from the Si substrate (figure 3.3). It appears that the TiO_2 reduces to Ti metal as the sputtering approaches the substrate with a chemical shift of 6eV. The O1s spectrum also decreases in intensity and is shifted to higher binding energy with additional sputtering time. The shape of the O1s, Si2p and Ti2p peaks is indicative of a variety of bonding configuration, possibly Ti-Si-Ox.

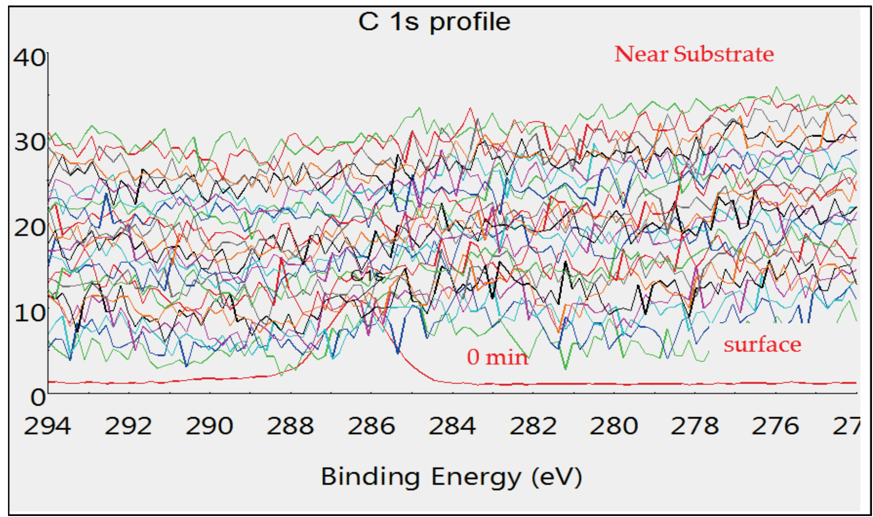

Figure 3.2: C1 signal from the entire sequence of Sputtered AR-XPS.

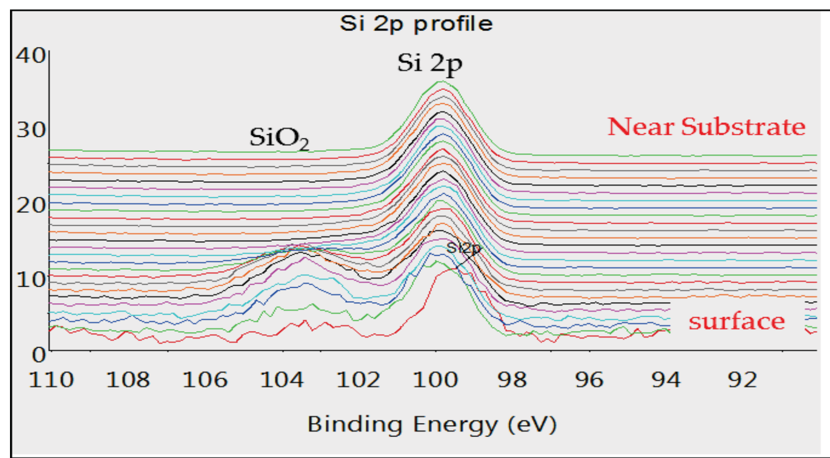

Figure 3.3: Si substrate signal - entire sequence of Sputtered AR-XPS.

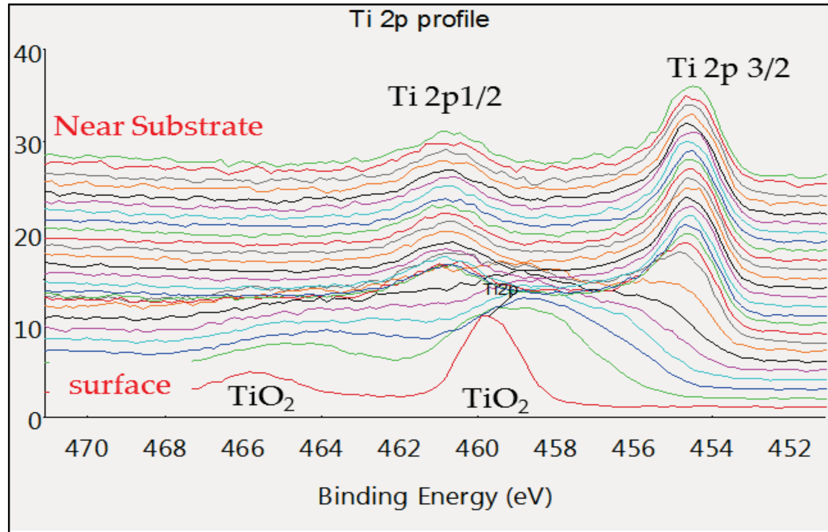

Figure 3.4: Ti signal from the entire sequence of Sputtered AR-XPS.

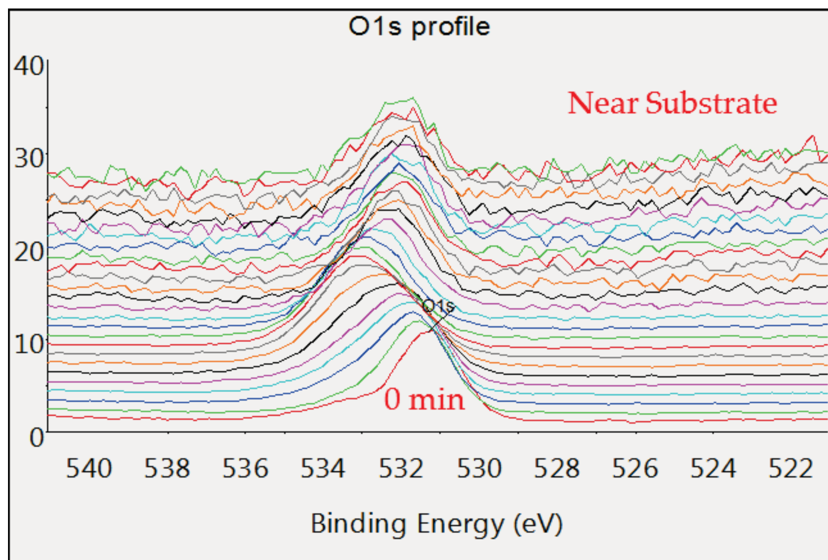

Figure 3.5: Oxygen signal - entire sequence of Sputtered AR-XPS.

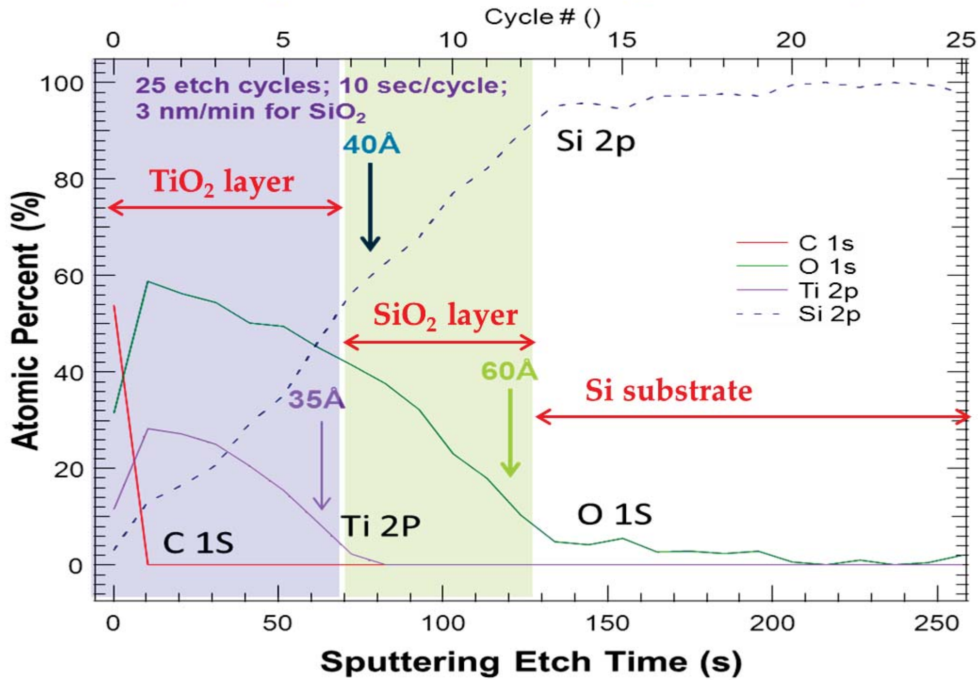

Figure 3.6: Average Thickness of TiO_2 layer: Å=34 Å (3.4nm)

As shown in figure 3.4, at the end of sputtering cycle, at the highest Ar^+ flow, the Ti^{4+} (TiO_2) component has vanished near the substrate, but is present on the virgin surface, while the reduced forms Ti^{3+} and Ti^{2+} emerge with sputtering. At the highest Ar^+ sputtering rate, the Ti^{4+} component has vanished (No TiO_2). This is due to the actual sputtering itself resulting in reduction of the TiO_2 over time (depth). In the x-ray photoelectron spectrum of TiO_2 thin film, Ti 2p doublet, shown in figure 3.4, consisted of $2p_{1/2}$ peak at E_B of 459.6 eV and $2p_{3/2}$ peak at E_B of 465.31 eV corresponding to the Ti^{4+} species in O–Ti–O bonding. A separation of about 5.8 eV between $2p_{1/2}$ and $2p_{3/2}$ is reasonably close to the 5.70 eV reported in literature for pure titania.

The additional components indicate the coexistence of different O chemical bonds, because Si and Ti cations compete strongly for O ions, resulting in the formation of mixed-oxide states at the interface. The Si-O-Ti component is assigned to Si- O-Ti cross-link bonds between the SiO_x layer and the TiO_2 over-layer. The growth toward higher binding energy can be due to the decrease in the number of Ti-O bonds due to the formation of Si-O bonds when Ti-O-Ti bonds are replaced by Ti-O-Si bonds. As Si is more electronegative than Ti, this difference shifts toward the higher binding energy. All of this rearrangement may be due to sputtering damage, i.e. unwanted chemical reactions, scrambling of the surface atoms or incorporation of the charged ions into the film. These results may complicate the calculated Maximum Entropy profiles as discussed in later chapters.

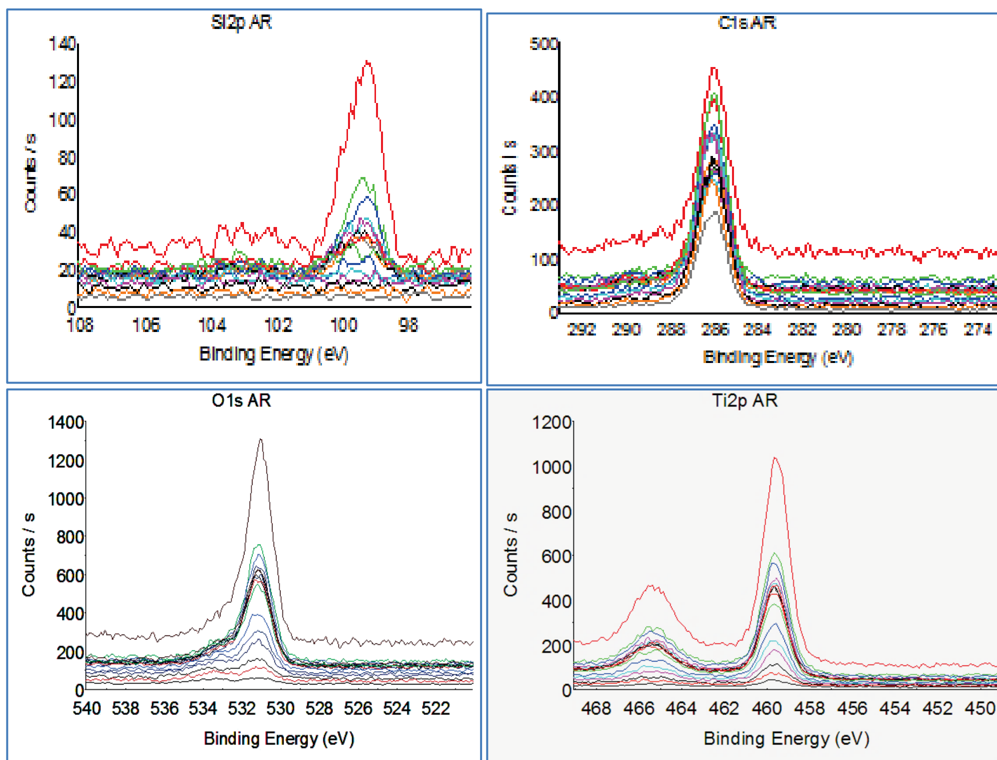

Figure 3.7: Sputtering of the 25nm film from the surface (red) to below the surface (blue) of Si2P, C1s, O1s and Ti2P peaks.

The thicker deposited film (~25-30nm) is mainly composed of Ti and O, except a constant amount of carbon throughout the film, which may result from the ex situ preparation process, the transfer process of the sample into the UHV chamber or residue on the surface from the organic precursor used to make the film. The C contamination occurs throughout the TiO_2 film, because the intensity of the C1s signal only decreases slightly with Ar ion sputtering, and C signal is still detected after the sputtering cycle is complete, see figure 3.7. This suggests that C is incorporated into

the TiO_2 film and is in agreement with the AR-XPS Lab data and the VKE-XPS data (figure 3.8).

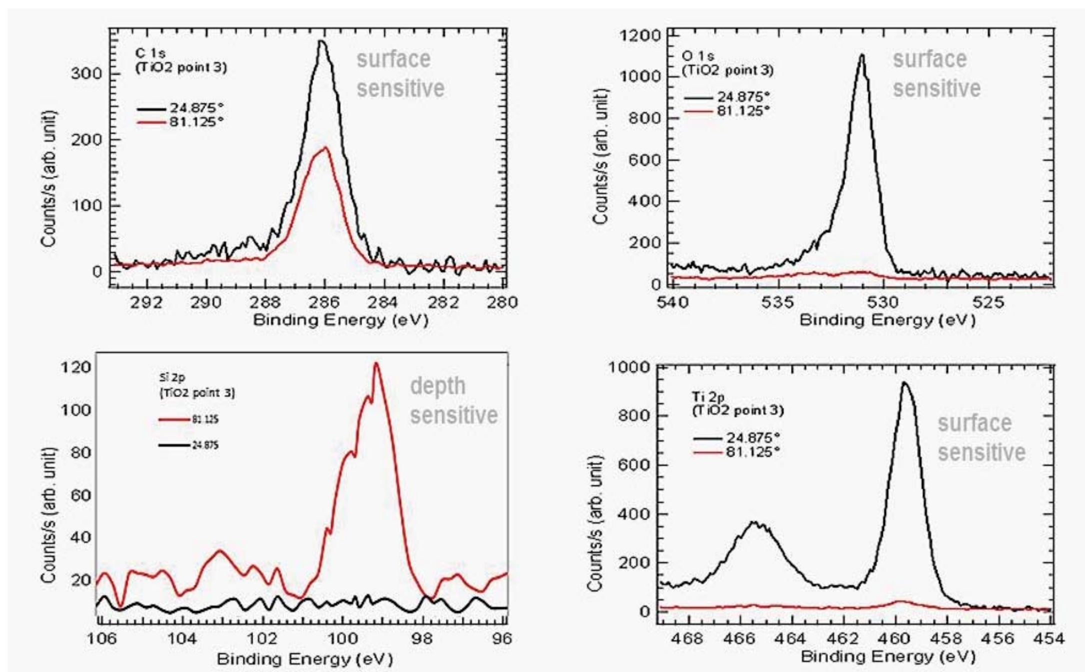

Figure 3.8: Angle dependence of sputtering of ~25nm film. Dark curve is 24° (surface sensitive) and the red curve is 81° (depth sensitive). Note the carbon presence throughout the film in upper left plot.

3.5 Auger Electron Spectroscopy (AES)
University of Delaware, Newark, Delaware

AES is an analytical technique used to determine the elemental composition and chemical state of the atoms in the surface region of a solid material. Radiation, ranging from 2 – 10keV, is incident on the sample and displaces a core electron, which results in a hole and thus an unstable atom in a high energy configuration, figure 3.9. This ionized atom lowers its energy state via electron transitions from higher energy

level to a lower energy level releasing energy of that transition in the form of X-ray fluorescence or an emitted Auger electron [85, 86, 87, 88].

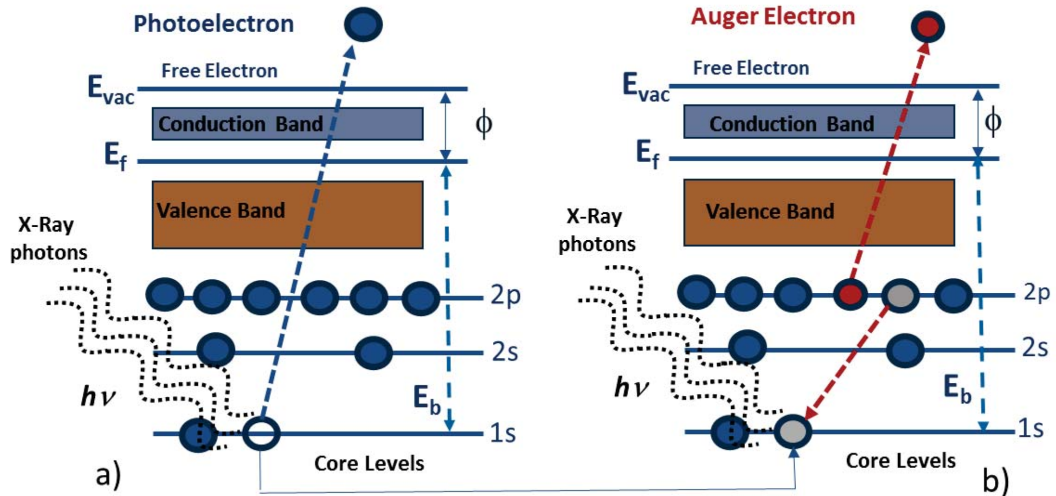

Figure 3.9: Auger process. a) Illustrates the generation of a core state electron hole, 1s level (now an unstable atom) b) Hole filled by higher energy electron (2p orbital) and this energy difference can be coupled to another 2p electron, which will be emitted and detected, if the energy exceeds the orbital binding energy.

a core state electron can be removed leaving behind a hole. As this is an unstable state, the core hole can be filled by an outer shell electron, whereby the electron moving to the lower energy level loses an amount of energy equal to the difference in orbital energies. The transition energy can be coupled to a second outer shell electron, which will be emitted from the atom if the transferred energy is greater than the orbital binding energy. Auger spectroscopy relies upon the measurement of the kinetic energies of these emitted electrons and is based on the analysis of energetic electrons emitted from an excited atom after a series of internal relaxation events (conservation

of energy). The kinetic energy, E_{AE} of the K, L_1, L_2 Auger electron can be written as: $E_{AE} = E_K - E_{L1} - E_{L2} - \Delta$ where E_K, E_{L1} and E_{L2} are the binding electrons in the K, L_1 and L_2 energy levels and Δ is a work function of the spectrometer [85]. It is the energy of this Auger electron that is characteristic of the material that emitted it, irrespective of the primary beam energy, electrons, x-rays or ions or their energy. The short inelastic mean free path of these electrons guarantees it to be a surface sensitive technique.

Initial survey definitely shows the titanium and oxygen in the film. Carbon exists on the surface as shown in figure 3.10, with the signal rapidly diminishing with sputter time. The carbon stays at a low level (never zero) as the sputtering continues (sampling deeper into the film) until the substrate is reached. The thickness for three measurements areas on the film was approximately 3nm.

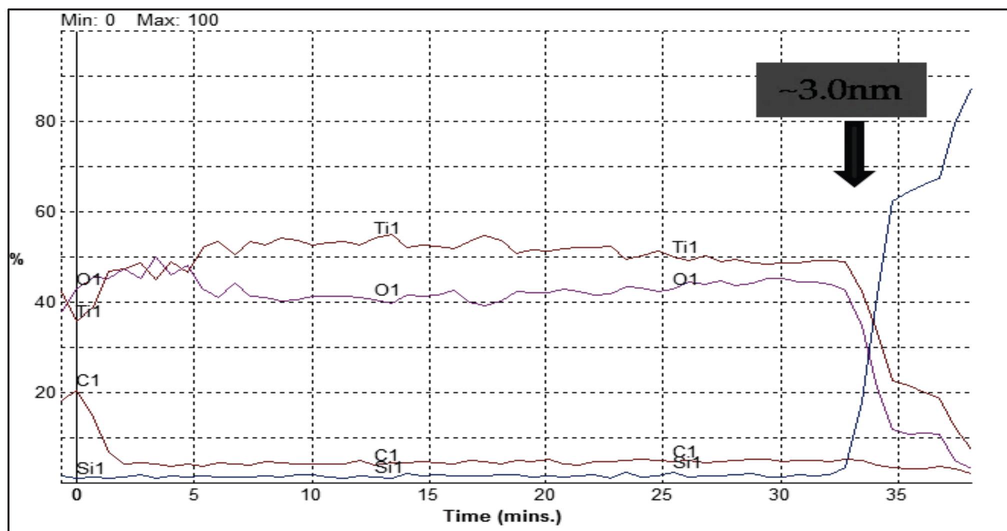

Figure 3.10: Auger Spectroscopy depth profile of thin (~ 2.5nm) TiO_2 film.

3.6 Rutherford Backscattering Spectroscopy (RBS)
Rutgers University, New Brunswick, New Jersey. L. Wielunski

Rutherford backscattering spectrometry (RBS) is an analytical technique also called High-Energy Ion Scattering (HEIS) Spectrometry and is used to determine the structure and composition of materials by measuring the backscattering of a beam of high energy ions (MeV) of low mass ions, impinging on a sample. The small ions have the ability to penetrate deep into the film, on the order of microns. The incident ions do not sputter the surface atoms or cause mixing of the atomic layers but they lose their energy through electronic excitation and ionization of the target atoms. Because these collisions are plentiful, the energy loss is continuous with depth. These fast-moving He^+ ions usually penetrate the atomic electron cloud and undergo close-impact collisions with the nuclei of the heavier target (film) atoms. This Coulomb repulsion between the incident ion and the film atoms is Rutherford scattering and is excellent for film analysis because of this classical two-body elastic scattering [57].

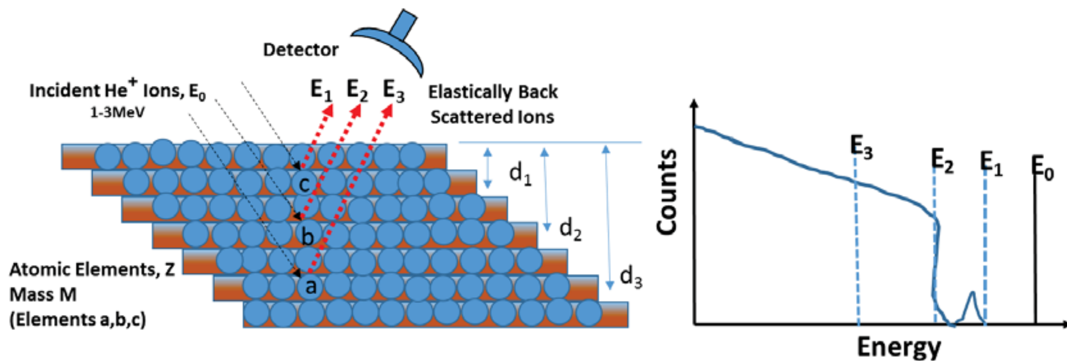

Figure 3.11: RBS layer model.

An incident ion of mass M_o and energy E_o is incident on to the film and an elastic collision between the ion and the surface atoms M, resulting is a rebounding ion energy of E_1. The collision is independent of the electronic configuration or chemical bonding of the target atoms but depends only on the masses and energies involved in the collision. Conservation of energy and momentum must be satisfied by:

$$E_1 = K_m E_o \quad (3.3)$$

Where K_m is the kinematic factor and can be calculated. Once the incident ion of $^4He^+$ at mass M_o=4 amu and energy E=2 MeV and the angular position of the ion detector are selected, usually $\theta = 170^o$, Km depends on the atomic weight of the films atoms. If a He ion scatters off a Si surface, the He ion energy will be reduced from 2MeV to 1.13MeV as described in [57, 89]. The depth profile can be determined from an RBS N(E) measurement. The elements contained by a sample can be determined from the positions of peaks in the energy spectrum. Depth can be determined from the width and shifted position of these peaks, and relative concentration from the peak heights (figure 3.12). This is especially useful for the analysis of a multilayer sample or for a sample with a composition which varies more continuously with depth.

After measuring the energy of the He ions and their number, the information is quantitative and results in elemental concentrations and depth distributions and it requires no standards. It is especially good for heavy elements within a lighter matrix.

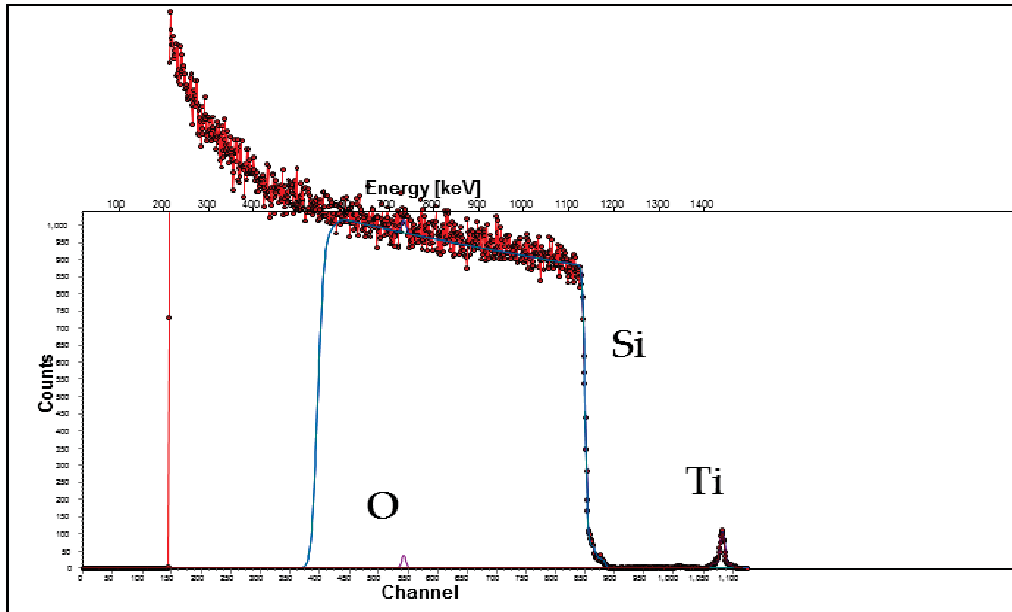

Figure 3.12: RBS raw data of the “thin” TiO_2 film.

Using RBS modeling and simulations and applying them to the RBS data above, a thickness of 2.586nm was determined (see figure 3.13), matching closely the estimated thickness of 3.0nm from the ALD growth rate target.

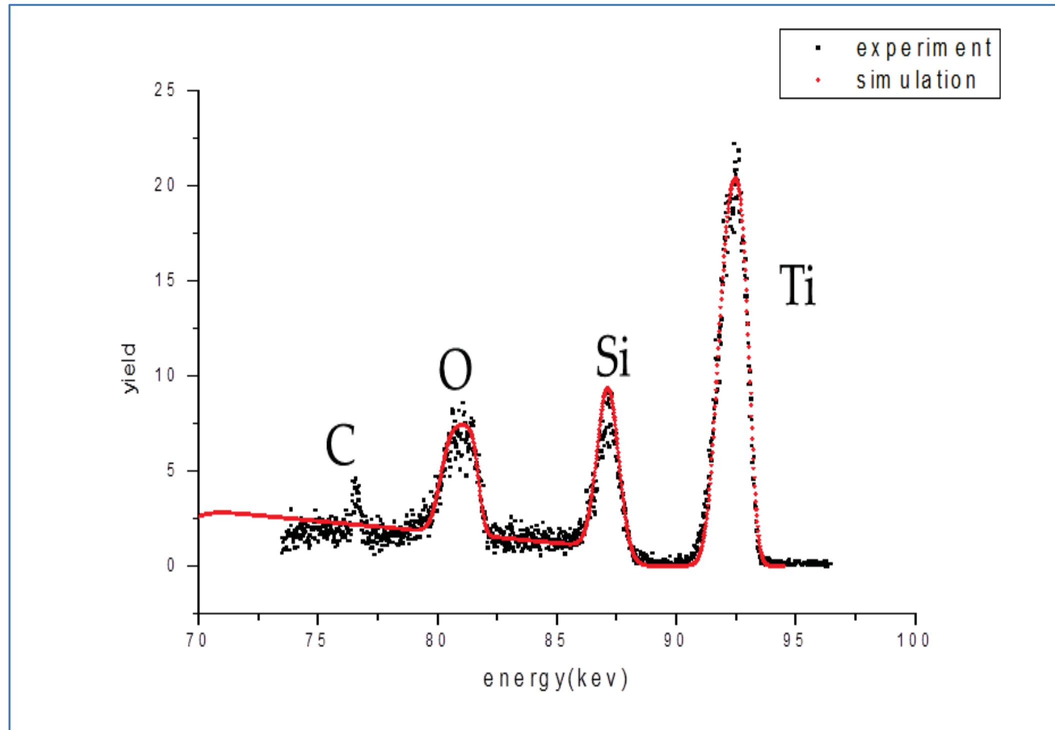

Figure 3.13: RBS data of TiO_2 thin film fitted with a model for 2.586nm thick film (simulation solid line).

3.7 Focused Ion Beam (FIB) & Transmission Electron Microscopy (TEM)

University of Delaware, W.M. Keck Electron Microscopy Facility

Focused Ion Beam (FIB) is associated with Scanning Electron Microscopy (SEM) and Transmission Electron Microscopy (TEM), except that FIB uses Ga^+ ions to raster over the surface of a film rather than electrons as in SEM/TEM (figure 3.14).

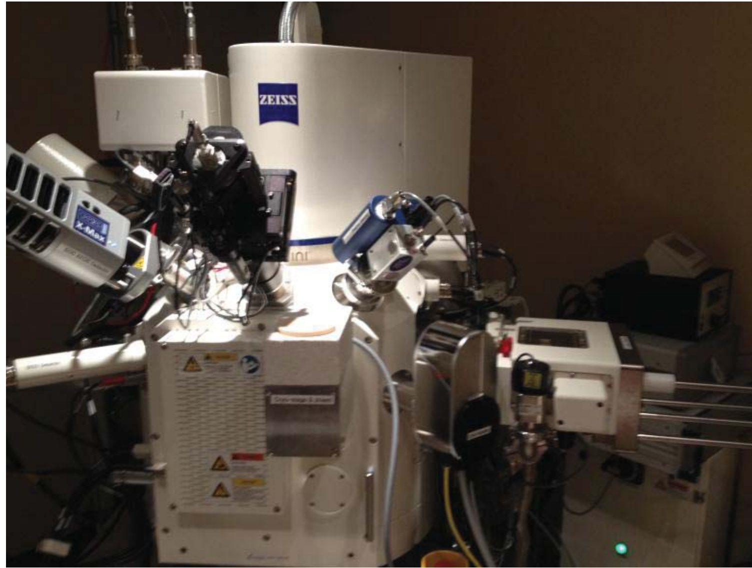

Figure 3.14: FIB (top) TEM (bottom) - University of Delaware, Newark, Delaware, Photo JJK.

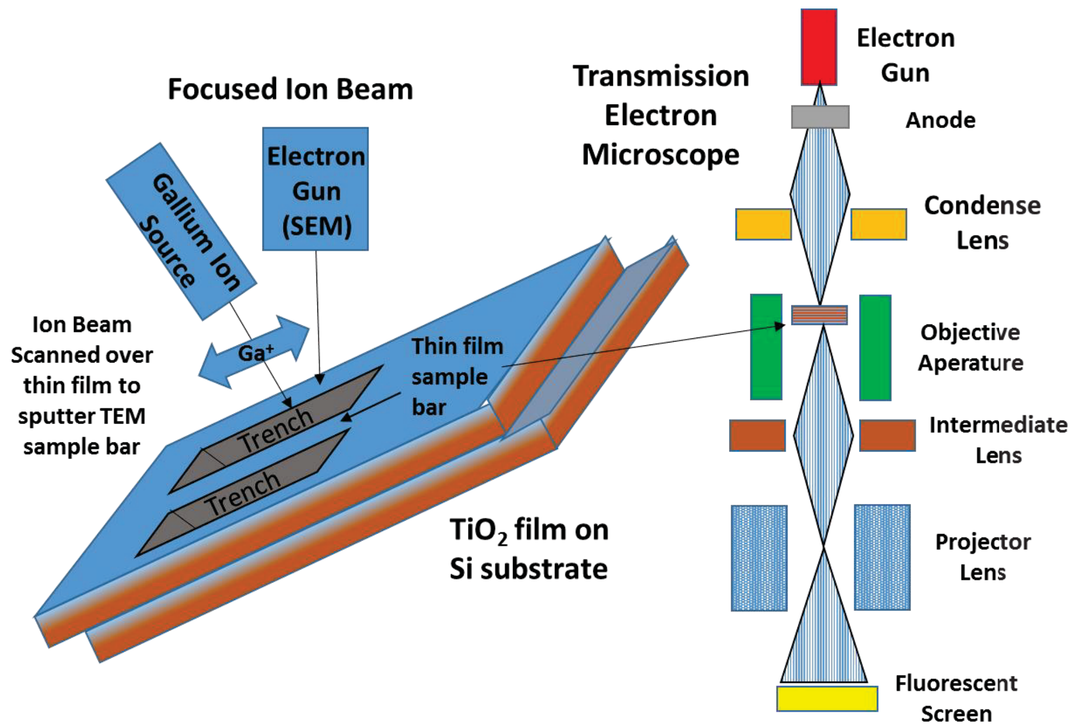

Figure 3.15: Schematic of Focused Ion Beam and TEM principles.

As shown in figure 3.15, the gallium (Ga^+) primary ion beam hits the sample surface and sputters a small amount of material, which leaves the surface as either secondary ions (i^+ or i^-) or neutral atoms (n^0). The primary beam also produces secondary electrons (e^-). As the primary beam is rastered over the sample surface, the signal from the sputtered ions or secondary electrons is collected to form an image [58, 59]. This technique also permits the drilling of small holes or trenches in the film at specific sites, allowing for the development of cross-sectional images of the structure (figure 3.16). Most systems are a combination of SEM/TEM and FIB and typically the ion beam is used for milling and the electron beam used for imaging. As opposed to RBS, the FIB technique is destructive but allows for higher magnification

images with better resolution and more accurate control of the milling site [59, 90, 91, 92].

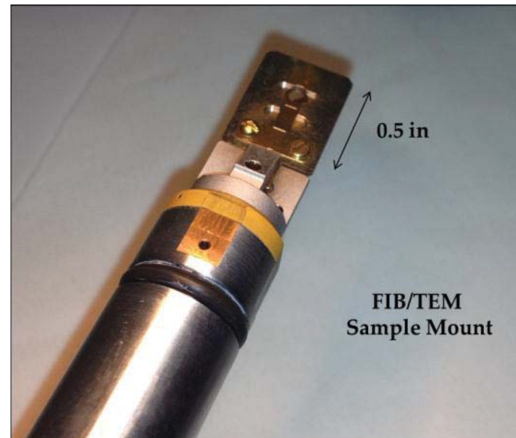

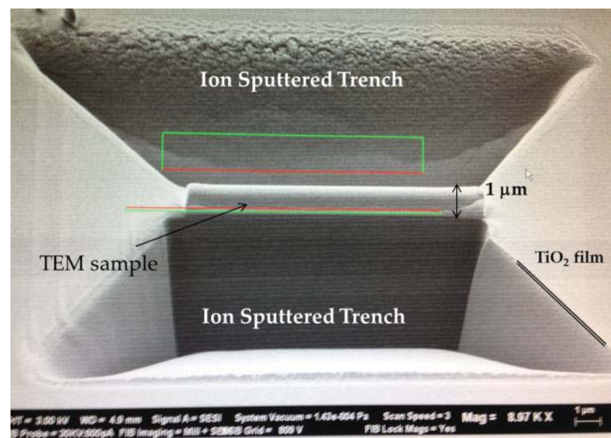

Figure 3.16: Top: FIB/TEM Sample Mount. Bottom: Scanning Electron Microscopy image of an FIB trench being carved to produce a small sample of the TiO_2 film for TEM imaging. Photo JJK.

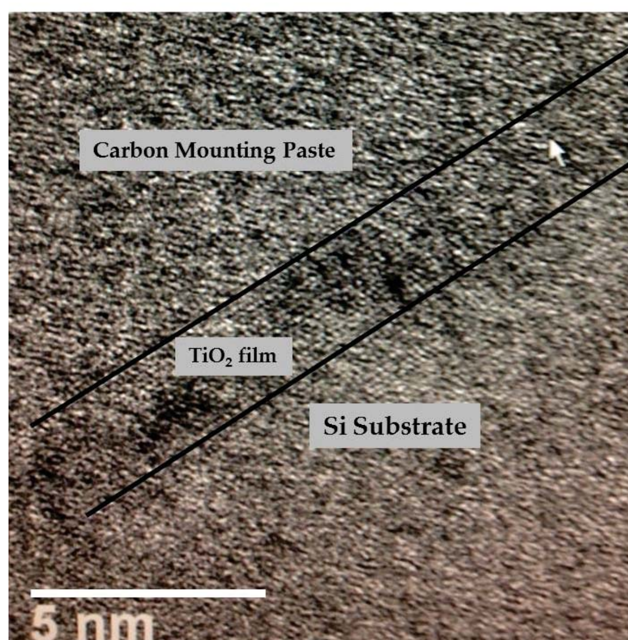

Figure 3.17: TEM image of the thin (~3nm) TiO_2 film.

At low primary beam currents, very little material is sputtered and modern FIB systems can easily achieve 5 nm imaging resolution (imaging resolution with Ga^+ ions is limited to ~5 nm by sputtering and detector efficiency). At higher primary currents, a great deal of material can be removed by sputtering, allowing for precision milling of the specimen down to a sub-micron or even a nanoscale levels.

The TEM measurements show a TiO_2 film of ~3nm but the interface appears to be non-uniform (figure 3.17). This may be due to the high energy of the FIB Ga^+ ions used to fabricate the TEM sample. The thick TiO_2 film (~25nm) was not measured with the TEM.

3.8 Variable Angle Spectroscopic Ellipsometry

University of Albany, New York, College of Nanoscale Science and Engineering

The technique of ellipsometry consists of measuring and interpreting the change in polarization that occurs when a polarized light beam is incident on a non-normal angle for the surface of a film (figure 3.20) [51, 52, 53, 56]. This optical technique is excellent in investigating dielectric properties and complex refractive indexes of thin films and is used extensively in the semiconductor and microelectronics industry because of its non-destructive nature.

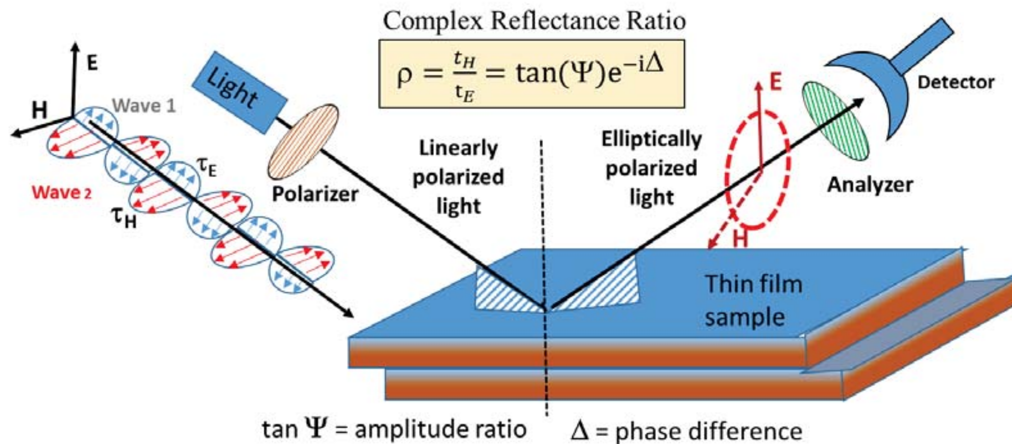

Figure 3.18: Schematic of the Variable Angle Spectroscopic Ellipsometry principles.

The polarization state of the light incident upon the sample may be decomposed into an E component (wave 1) and a H component (wave 2) with the E component oscillating perpendicular to the plane of incidence and the H component oscillating at right angles to E. (figure 3.18) The amplitudes of the E and H components, after reflection and normalized, are denoted by τ_E and τ_H, respectively.

Ellipsometry measures the complex reflectance ratio, ρ, which is the ratio of H amplitude, t_H divided by the E amplitude, t_E:

$$\rho = \frac{t_H}{t_E} = \tan(\Psi)e^{-i\Delta} \tag{3.4}$$

Since Ellipsometry is measuring the ratio of two amplitudes at various angles, is very accurate and reproducible for thin films but it is an "indirect" method. In general we measure Ψ (amplitude component) and Δ (phase difference) but these cannot be converted directly into the optical constants of the sample so a model analysis must be used which considers the optical constants (refractive index or dielectric function tensor) and thickness parameters of all individual layers of the sample including the correct layer sequence. Using an iterative procedure (least-squares minimization) unknown optical constants and/or thickness parameters are varied, and Ψ and Δ values are calculated. The calculated Ψ and Δ values which match the experimental data best provide the optical constants and thickness parameters of the sample.

The vectors of electric field E and magnetic field H are perpendicular to the direction of the light propagation. Because vectors E and H of electromagnetic wave are perpendicular also to each other, the state of the light anisotropy in the direction perpendicular to the wave propagation can be described by any of these two vectors. Generally, the polarization direction is the direction of the electric field vector E.

VASE was used to analyze only the thin (~2.5-3nm) TiO_2 film deposited on SiO_2 (native oxide) which is on the silicon substrate using the Three Tauc-Lorentz Oscillators to model the TiO_2 and SiO_2 layers resulting in a thickness of 7.32 nm with

an Optical Band Gap of TiO_2=3.01eV. Figure 3.19 shows the VASE data with the top graph plotting Ψ against wavelength and the middle graph plotting Δ against wavelength. The bottom graph shows the optical constant vs. eV used in the modeling.

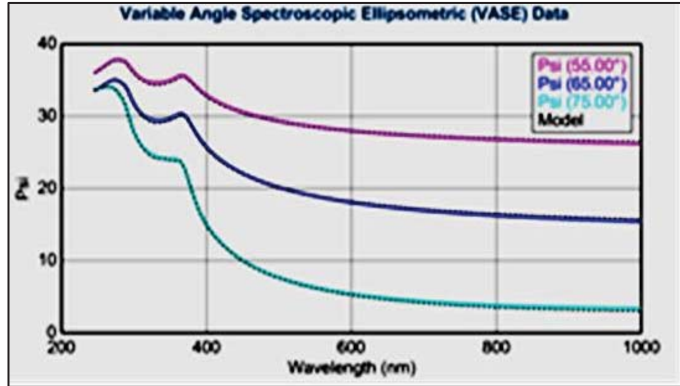

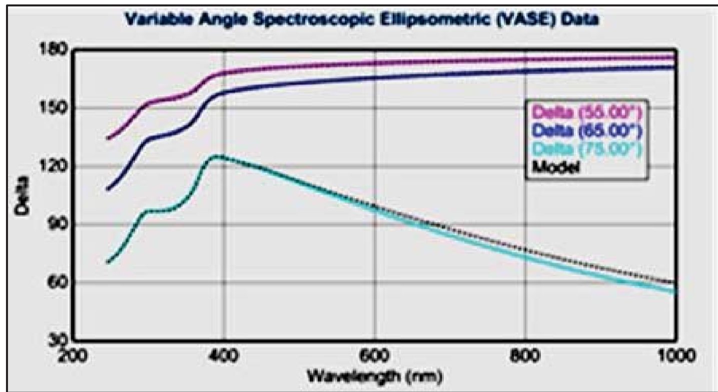

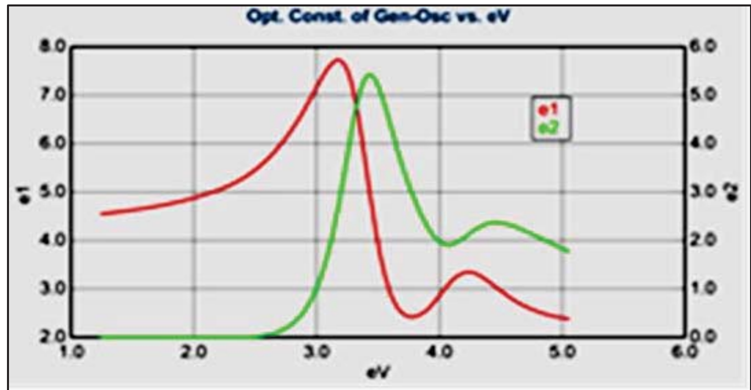

Figure 3.19: VASE data Top: Ψ plotted against wavelength. Middle Δ plotted against wavelength. Bottom: Optical constant vs. eV.

Chapter 4

METHODOLOGY

4.1 Introduction - Data Collection

Determining chemical depth profiles non-destructively involves complex data analysis and well as prior knowledge of the film. To accurately measure a depth profile of the dielectric film using VKE-XPS data, the maximum entropy model will be applied with known boundary conditions (thickness and elements present) determined from alternate analytical techniques previously discussed. These include Auger electron spectroscopy, Angle Resolved–XPS, Rutherford Backscattering Spectroscopy and Variable Angle Spectroscopic Ellipsometry for thickness and elemental composition. To understand the surface structure and uniformity that impacts the detection of escaping electrons, scanning electron microscopy and transmission electron microscopy will be utilized. Thickness and elemental information will be applied to develop the initial model and subsequent chemical depth profile of two actual films.

4.2 Information Entropy

Entropy is the measure of uncertainty or disorder and of information content and is referred to in Information Theory as Shannon entropy; a measure of the average information content one is missing when one does not know the value of the random variable. An extension of this theory is the maximum entropy method with regularization, which brings a significant advance in analyzing VKE-XPS by defining

the most probable solution of limited and noisy data [21, 93, 19, 94]. In creating an accurate depth profile, entropy is maximized with constraining boundary conditions (regularization) to generate the simplest profile that fits the data. *The principle of maximum entropy states that subject to precisely stated prior constraints (testable information), the probability distribution which best represents the current state of knowledge but leaves the largest uncertainty (i.e. the one with the largest or maximum entropy) is the distribution with the least assumptions or* biases [24]. In other words, the selected distribution is the one that makes the least claim to being informed beyond the stated data that admits the most ignorance beyond the stated prior data.

Others have utilized angle-resolved photoemission data in conjunction with a maximum entropy algorithm for converting angle dependent photoemission data into a concentration depth profile. Many algorithms for calculating concentration depth profiles from angle resolved photoemission spectra measurements have been published during the last decade, ranging from simple least-squares fitting to the Tikhonov regularization and maximum entropy methods [85] reviews a variety of techniques and highlights the problems associated with reconstructing the depth profile from the angle resolved data, which is inherently an under-determined problem. We will model all that is known about the variable angle or variable energy data, and use any pre-existing information to develop a depth profile, assuming as little as possible (maximizing entropy).

The generation of accurate depth profiles from XPS date (either ARXPS or VKE-XPS) is a difficult mathematical LaPlace transform that does not have a unique solution, since many generated profiles can fit the data. There exist an extremely high number of model solutions that fit the experimental noisy data within the measurement

precision [65]. Simply minimizing the weighted "sum-of-square differences" between the calculated and measured data is not always adequate for determining the correct sample depth profile, especially if the sample contains a large number of components and the data collection very noisy.

To address the balance of fitting the data without fitting the noise, a regularizer is employed. In this "regularized" procedure, the optimization of the model profile is the minimization of the combined function: **residual norm + α solution norm,** where α is the regularization parameter, discussed below.

The **residual norm** is a measure of the goodness of fit to the experimental data for the proposed depth profile, typically using the χ^2 statistics [23]. A smaller residual norm corresponds to a better fit to the data and a large residual norm corresponds to a poor fit to the data. The **solution norm** is some measure of the complexity of the proposed depth profile, usually appearing as "noise", with the most widely used example being the profile cross-entropy or maximum entropy method, Ent-model [95]. The "regularization parameter" α, balances both sides of this dual function – good fit to the data while minimizing fitting the data to the noise, thus generating the most acceptable and smoothest overall profile.

4.3 Slab Model

Photoelectrons, by interacting with the atoms in the substrate, travel only a short distance before being inelastically scattered. The intensity of the photoelectron signal, I, as a function of depth below the surface, d, can be approximated as

$$I = Io \exp(-z/\lambda \cos \theta) \tag{4.1}$$

where, I_o is the intensity of the emitted photoelectrons in the absence of any inelastic scattering, θ is the collection angle of the emitted photoelectrons relative to the surface normal, λ is the attenuation length of the photoelectrons. The intensity of the photoelectron signal as a function of depth is related to the cosine of the collection angle as can be seen in Figure 4.1. The attenuation length of the photoelectrons sets the depth for photoelectron spectroscopy.

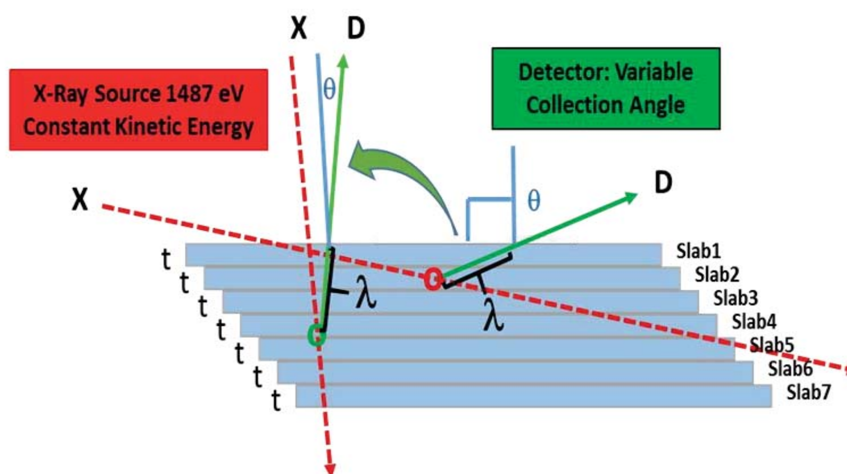

Figure 4.1: AR-XPS slab model. λ= Inelastic Mean Free Path (IMFP)

Photoemission is well suited for examining the depth profiles of these dielectric films because the thicknesses of the films are on the same scale as the attention length of the photoelectrons. With higher x-ray energies (VKE-XPS), one can probe deeper into thicker films and non-destructively characterize the layers of the film down to the substrate.

4.4 Depth Profile Regularization Technique

The standard description of depth sensitivity in XPS is according to Beer-Lambert Law where the intensity of a photoelectron signal varies as a function of depth.

$$I_{j,k} = R_{j,k} \int_0^{\infty} n_j(t) exp\left(-\frac{t}{\lambda_{j,k}\, sin\, \theta_k}\right) dt \tag{4.2}$$

$I_{j,k}$ is the measured intensity for element ‘j’ collected at beam energy ‘k’, $n_j(t)$ is the concentration as a function of the depth, t (from 0 at the surface increasing into the bulk), $\lambda_{j,k}$ is the IMFP for element ‘j’ collected at beam energy ‘k’, and θ_k the takeoff angle. $R_{j,k}$ is the photoemission intensity or sensitivity from a pure sample of the element [82].

The film can be considered as a series of thin 1 nm slabs: slab1, slab2, slab3 down to the substrate with constant in-slab concentration. Slab level and thus electron escape depth, is governed by the incident angle. Applying the “thin slab” model to the simulations, and designating the slab index as ‘i’ and thickness of each slab, Δt for the depth t_i with constant in-slab concentration $n_{i,j}$. So the intensity can be calculated as:

$$I_{j,k} = R_{j,k}\left[1 - \exp\left(-\frac{\Delta t}{\lambda_{j,k}\sin\theta_k}\right)\right]\sum_{i=0}^{\infty} n_{i,j}\exp\left(-\frac{t_i}{\lambda_{j,k}\sin\theta_k}\right) \tag{4.3}$$

It is very difficult to obtain $R_{j,k}$ values at all experimental conditions, but it is simpler to consider only the ratio of $I_{j,k}/R_{j,k}$ to calculate atomic concentrations, as discussed in the next section. For a semi-infinite pure material, the concentration

becomes a constant 1, and equations (4.2) and (4.3) become $I_{j,k} = R_{j,k}$ as expected for a pure material collected at the given beam energy and takeoff angle.

Now with HA-XPS it is possible to use variable kinetic energy to collect spectra at a range of beam energies corresponding to various depth sensitivities, just as varying the angle in AR-XPS corresponds to various depth sensitivities. Using the same slab model calculations as in VKE-XPS, one can provide non-destructive depth sensitive composition information on a sample by detecting excited electrons from deeper and deeper into the film with increasing beam energy (figure 4.2).

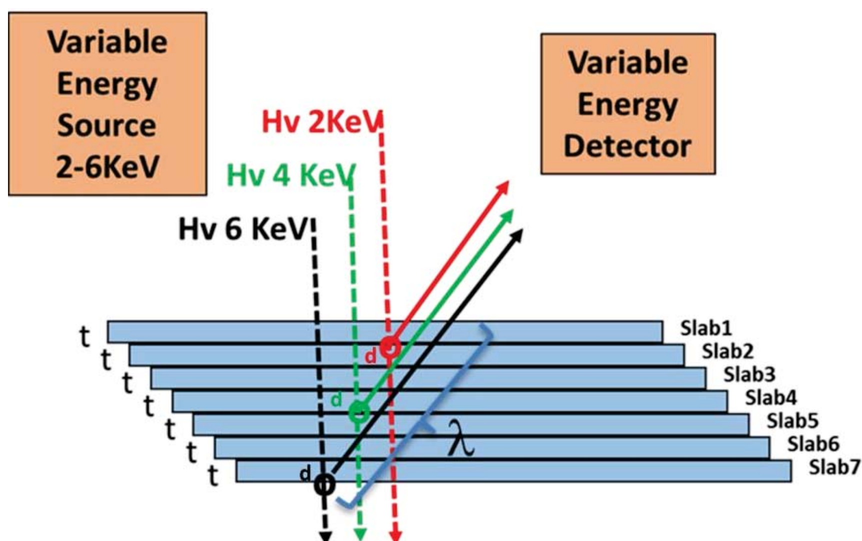

Figure 4.2: VKE-XPS Slab model: Non-destructive depth sensitive composition information on a sample by detecting excited electrons from deeper and deeper into the film with increasing beam energy.

Methods used in this VKE-XPS were based on the similar techniques that were successfully applied to ARXPS. A comprehensive summary of these methods can be found at [23, 96]. There are a variety of algorithms with various advantages and

disadvantages that can be used to achieve better resolution of the data. As stated earlier, the challenge is to select the best of multiple reconstructions that would fit the data by minimizing any artificial correlations in the data while making only minimal assumptions about the sample structure.

4.4.1 Transformation Matrix

The conversion between depth-sensitive concentration of an element and excitation energy dependent data can be taken as a matrix transformation:

$$\mathrm{D} = \mathrm{M} \cdot \mathrm{N} \tag{4.4}$$

Here, N the concentration as a function of depth, (the goal of the VKE-XPS), D matrix represents the concentration as a function of beam energy, which is not easily converted to the concentration vs. depth without M the transformation matrix. For an element j, the elements of the full transformation matrix are given by:

$$M_{k,i} = \left[1 - exp\left(-\frac{\Delta t}{\lambda_{j,k} sin\theta_k}\right)\right] exp\left(-\frac{t_i}{\lambda_{j,k} sin\theta_k}\right) \tag{4.5}$$

The elements $N_{i,j}$ are the concentration of element j at depth i; but the inverse transformation does not exist, i.e. $N^j \neq M^{-1} D^j$. It involves minimizing the difference between the measured VKE-XPS data and the calculated depth profile. The concentration matrix elements become:

$$D_{k,j} = \left[1 - \exp\left(-\frac{\Delta t}{\lambda_{j,k} \sin\theta_k}\right)\right] \sum_i n_i \exp\left(-\frac{t_i}{\lambda_{j,k} \sin\theta_k}\right) \tag{4.6}$$

For an infinite N matrix (bulk concentration), combine eq. 4.3 with eq. 4.4, then $D_{k,j}$ becomes:

$$D_{k,j} = \frac{I_{j,k}}{R_{j,k}} \tag{4.7}$$

Recall the transformation matrices M are dependent on the electron attenuation lengths as well as N, and in practice may be singular, so an inverse transformation does not readily exist. Instead, a solution for N is provided by minimizing the difference between the measured VKE-XPS data and the calculated transformed depth profile [82]. Since the measured VKE-XPS data always contains noise and usually has fewer data points than the ideal depth profile, a regularizer is typically applied to smooth and fit the data. Following Chang et al. [3], this can be accomplished by maximizing a functional Q:

$$Q = \alpha S - {}^{C}/_{2} \tag{4.8}$$

Where S represents the regularization functions as detailed in Table 4.2, α is the regularization parameter, which will be discussed below, and C is the χ^2 value between measured VKE-XPS and that calculated from the transformed depth profile.

The regularization parameter, α, acts as a weighting factor between regularizing the data (smoothing the noise) and fitting to the χ^2 value (fitting the data to a model). An α that is too small will result in over-fitting the data (fitting the noise as real data), while a large α will result in a poor fit to the experimental data. While

this parameter can be optimized analytically [21], it is often easier to perform the regularization routine using various values for α and selecting the result, which provides the simultaneously optimized values for S and C [23]. This is accomplished by minimizing a parameter d:

$$d = \sqrt{S^2 + C^2} \tag{4.9}$$

The parameter d is simply the length of a line from the origin to point (C, S) in a hypothetical C/S space and has no physical meaning, (See L-curve discussion in section 5.1.5). The minimum d will represent the point closest to 0; since S is always negative and C always positive; this will simultaneously provide the optimal S and C for maximized Q [82].

4.4.2 Inelastic Mean Free Path - IMFP (λ)

Inelastic Mean Free Path (IMFP) for the routines are calculated using the Tanuma Powell Penn Algorithm (TPP-2M) [97] and the National Institute of Standards and Technology (NIST) IMFP database [98]. The TPP-2P predictive equation for IMFP as a function of electron energy, E(ev) is

$$\lambda = \frac{\mathrm{E}}{E_p^2\ [\beta \ln(\gamma \mathrm{E}) - (\mathrm{C}/\mathrm{E}) + (\mathrm{D}/E^2)]} \tag{4.10}$$

Where:

$$\beta = -0.10 + 0.944\ (E_p^{\ 2} + E_g^{\ 2}\ )^{-1/2} + 0.069\rho^{0.1}$$

$$\gamma = 0.191\rho^{-1/2}$$

$$C=1.97-0.91U,$$

$$D=53.4-20.8U$$

$$U = N_v\rho/M = E\rho^2/829.4.$$

$E\rho=28.8(N_v\ \rho/M)^{1/2}$ is the free-electron plasmon energy (eV), N_v is the number of valence electrons per atom, ρ is the density $(g/cm)^3$, M is atomic number or molecular weight and E_g is the bandgap energy (eV).

The IMFPs for Ti, O, and Si for the 5 photon energies used are listed in Table 4.1. IMFPs were used in place of effective attenuation lengths (EALs) due to the relative simplicity of modeling and readily available databases for IMFP values. As such the work presented here does not take elastic scattering effects into account, which may lead to an overestimation of thicknesses when interpreting experimental data. However, for the simple film structures presented in this study, the deviation between IMFP and EAL is expected to be minimal [99]. IMFPs were assumed to be independent of local composition. This assumption was chosen to reduce calculation time though may introduce complications in interpretation of experimental data, as discussed below. For more accurate IMFP values, the IMFP for an electron originating in slab “i" would need to be calculated considering all slabs i' < i which cannot be easily accounted for in this model. Simulated VKE-XPS data were produced using the same matrix transformation as in the regularization routine.

Table 4.1: IMFP values for simulated VKE data. All values in nm.

hν	Ti $2p_{3/2}$	O $1s$	Si $1s$
2500	4.21	4.08	1.76
3000	5.03	4.90	2.69
3500	5.83	5.71	3.57
4000	6.61	6.49	4.41
4500	7.38	7.26	5.23

4.4.3 Python Algorithms – Program Flow Diagrams

The algorithms in this work to calculate α and the composition depth profiles were written in Python, a high-level object-oriented, programming language that is easily readable with an uncluttered visual layout [100]. It is versatile for manipulating extended matrixes (multiple slabs, energy levels, elements and input parameters) and coupled with the large standard library of pre-written tools such as "numpy", a numerical routine for dealing with arrays and "scipy" a routine for manipulating scientific formulas, it is optimal for calculating compositional depth profiles from VKE-XPS data. See figure 4.3 for the Python flow diagram outlining the logic for generating the depth profile of the TiO_2 film. (See Appendix A for Python code).

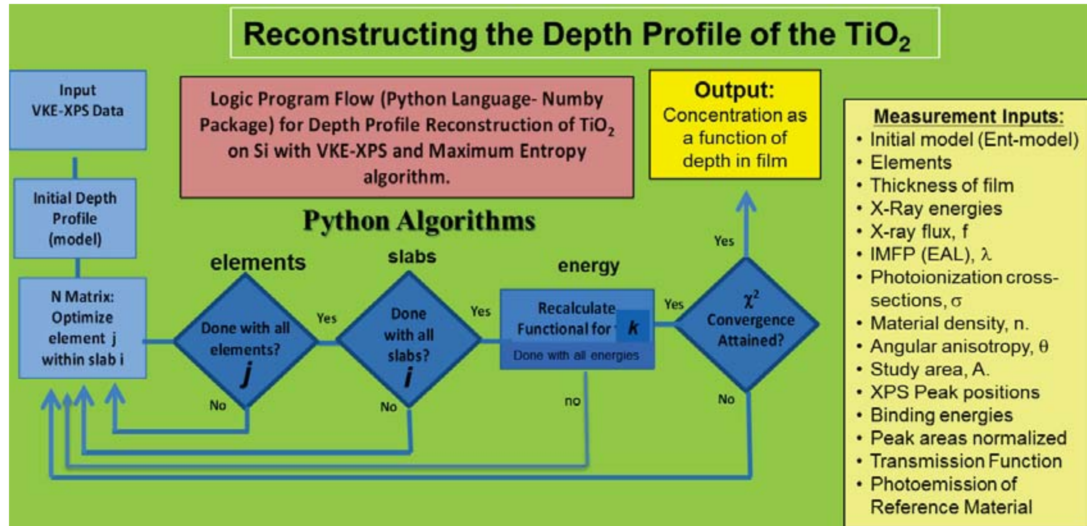

Figure 4.3: Flow of program logic in reconstructing the depth profile of the TiO_2 on Silicon from VKE-XPS data and Maximum Entropy Algorithm.

Inputs to the program include measured (or simulated) VKE data, binding energies, beam energies, and initial model in the Ent-model. The program first calculates the IMFP values, and uses this value to determine the total depth of the calculated profile. The total depth was chosen to be four times the maximum IMFP so that deeper signals would contribute negligibly to the total intensity, as discussed earlier. The routine then steps the elements in the **N** matrix one by one. Adjustments are made by adding or subtracting a small value, typically 0.01 to the value from the previous step. The values are constrained between 0 and 1, and are renormalized so that the sum of all elements is always unity. The new **D** matrix is calculated according to equations 4.6 and 4.7, is used to calculate the atomic concentration VKE profiles and for the calculation of $\chi^{2.}$ The Q functional is then calculated; if it is found to increase, the new **N** matrix is kept since maximizing Q is goal to balance S and χ^2. Otherwise the elemental concentration is stepped in the opposite direction and the

calculations repeated. If neither step improves Q (maximizes), then the initial **N** matrix element is kept. The routine repeats for all N matrix elements and iterates until the change in Q is below a defined convergence limit of 0.01. The maximization routine is performed using $\alpha = 10^x$ where x is an integer value between -9 and 9. The **N** matrix corresponding to the value of α minimizing 'd' as per equation 4.9 was kept as the final result; no further optimization of α was performed (figure 4.4). Following Paynter [23,101] and, various regularization functions, S, listed in Table 4.2, were tested using simulated data and will be discussed in the results section below.

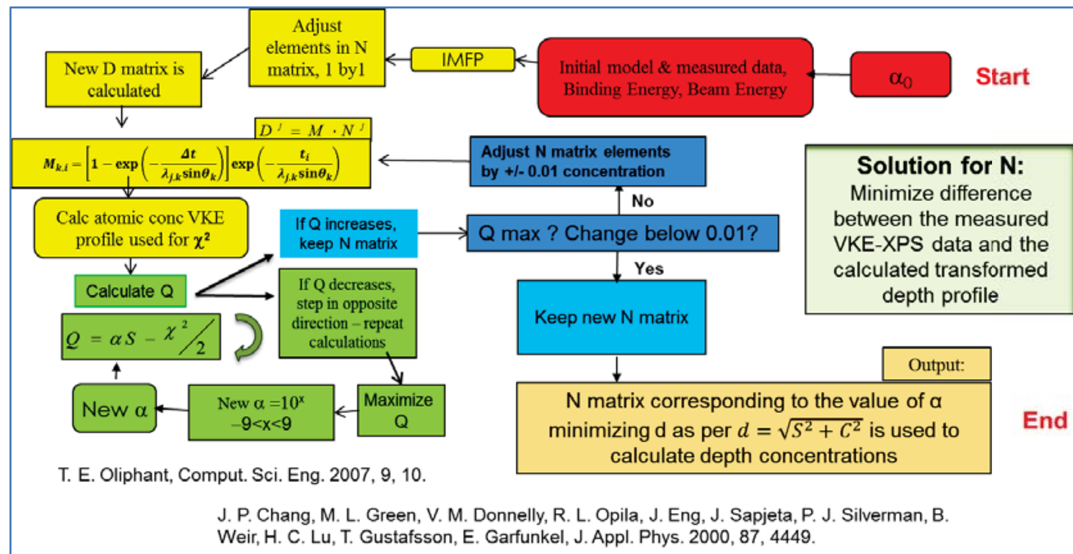

Figure 4.4: Optimizing N-matrix for depth sensitive concentration.

4.4.4 Specific Regularization Functions

The regularization functions used in this study are shown in Table 4.2. The regularizer introduce additional information to solve the "over fitting" the data problem and reduces the complexity through some form of smoothing. The solution

norm considers this complexity as applied to the proposed depth profile. We use the Ent-model, Slopes, Curves and Total Variance Analysis regularizations in this study.

The Ent-model compares the data, $n_{i,j}$ with the model $m_{i,j}$, summed over the all elements j and slab number i, (see Table 4.2). Here an initial model (an estimated guess using prior knowledge) is considered in the regularization function. As we'll see, this will have a great effect on the data analysis. The Slopes regularization function optimizes the slower changes in value of the slopes of the data by using first derivative for smoothing. This is done by fitting neighboring data points (n_i and n_{i+1}) with a low level polynomial according to the least square method (log $[1 + |n_{i+1}-n_i|]$ and summing over i slabs and j elements. Being of higher order, the Curves function is similar to slopes except the larger changes in the values of multiple points ($n_{i+2,j} - n_{i+1,j}$) are used in generating the curvature or second derivative for smoothing; then summed over elements j and slabs i. The Total Variance Analysis (TVA) compares the atomic concentration $n_{i,j}$, to the average, $\langle n \rangle$, similar to χ^2 analysis but addressing the variance $(n_{i,j} - \langle n \rangle)^2$. Each technique addresses a "smoothing" algorithm with the purpose to increase the signal-to-noise ratio and capture important patterns in the data.

Table 4.2: Regularization functions used in this study. For all equations, n_{ij} represents the atomic concentration of element "i" at depth "j", m_{ij} is the atomic concentration of the initial model, and <n>is the average value.

Descriptions of Regularization Functions, S

Description	Function	S
Compares the data, $n_{i,j}$ with the model $m_{i,j}$.	Ent-model	$\sum_i \sum_j \left(n_{i,j} - m_{i,j} - n_{i,j} \ln\left(\frac{n_{i,j}}{m_{i,j}}\right)\right)$
Optimizes the slower changes of slopes of the data by fitting neighboring data points with polynomial and least square method	Slopes	$-\sum_j \sum_{i=1}^{N_{slab}-1} \lvert n_{i+1} - n_i \rvert \log\{1 + \lvert n_{i+1} - n_i \rvert\}$
Optimizes larger changes in the values of multiple points in generating the curvature or second derivative for smoothing;	Curves	$-\sum_j \sum_{i=1}^{N_{slab}-2} \lvert (n_{i+2,j} - n_{i+1,j}) - (n_{i+1,j} - n_{i,j}) \rvert \log\{1 + \lvert (n_{i+2,j} - n_{i+1,j}) - (n_{i+1,j} - n_{i,j}) \rvert\}$
Compares the atomic concentration $n_{i,j}$, to the average, <n> (variance).	TVA	$-\sum_i \sum_j (n_{i,j} - \langle n \rangle)^2$

R. W. Paynter and M. Rondeau, Journal of Electron Spectroscopy and Related Phenomena **184**, 43–51 (2011).

As stated earlier, the "regularization parameter", α, balances the two considerations in the joint function: achieving a good fit to the data, and avoiding unphysical spikes and steps in the depth profile arising from over-fitting the noise in the data (details below) [82].

4.5 Atomic Concentration Measurements for VKE Spectra

Atomic concentrations in XPS can be calculated by normalizing intensities of photoelectron transitions to relative sensitivity factors:

$$X_A = \frac{I_A / R_A}{\sum_j I_j / R_j} \tag{4.11}$$

Here I_j and R_j are the measured intensity and relative sensitivity factor respectively for a species j [65]. For XPS data collected with conventional lab sources, there exist well measured and calibrated sensitivity factors, making the measurement of atomic concentration straightforward. Unfortunately, this is not the case for VKE-XPS. Sensitivity factors are dependent on the photoionization cross-section, X-ray spot size, detector transmission function and other instrument and specimen specific parameters. However, there are a few ways to overcome this limitation.

The most accurate measurement method, even where sensitivity factors exist, is to measure reference specimens along with the specimens of interest under the same experimental conditions. Pure films need not be employed, so long as the composition of the reference specimen is known. The measured intensity from the reference spectra can then be used in place of R in equation 4.11.

4.5.1 Measurement Parameters

Photoionization cross section is the probability that an x-ray photon will excite the photoelectron transition of interest. Photoionization cross-sections extrapolated from calculated values in [102, 103] are shown in table 4.3. Values are normalized to the electron occupation (2j+1).

Table 4.3: Photoionization cross-sections extrapolated from calculated values

hν	Ti $2p_{3/2}$	O $1s$	Si $1s$
2500	2.32	2.80	7.76
3000	1.23	1.55	5.40
3500	0.88	1.15	4.30
4000	0.53	0.75	3.20
4500	0.41	0.58	2.62

4.5.2 Photoionization Cross-section and Sensitivity Factors

Without well-characterized reference materials, the photoionization cross-sections, IMFPs and material densities can be used to estimate the sensitivity factors. The photoemission intensity of the reference material is given in [83] as:

$$R = nf\sigma\Theta\lambda AT \tag{4.12}$$

R is dependent on the atomic density of the reference material, n, the X-ray flux f, the photoionization cross-section, σ, the angular anisotropy, Θ, the area under investigation, A, and the detector transmission function T. As all elements should be measured under the same experimental conditions; f, Θ, and A can be grouped as a constant, F. For accurate measurements, the detector transmission function should be considered in the calculation of R is available from the detector manufacturer. Thus for an element A measured at beam energy hν, R becomes:

$$R_A(h\nu) = F\, n_A \sigma_A(h\nu) \lambda_A(h\nu) T_A(h\nu) \qquad (4.13)$$

The instrument specific terms are taken into the constant F. Thus for a given beam energy, the atomic concentration becomes:

$$X_A = \frac{I_A / n_A \lambda_A \sigma_A T_A}{\sum_j I_j / n_j \lambda_j \sigma_j T_j} \qquad (4.14)$$

Equation 4.13 provides the apparent atomic concentration. The maximum entropy routine then converts these apparent atomic concentrations into ‘real’ atomic concentrations vs. depth.

4.5.3 Peak Intensity Measurements

Peak positions for collecting XPS data for both the thick and thin TiO_2 films are shown in table 4.4. The calculated binding energies are shown in table 4.5, the binding energy shift in table 4.6 and the transmission functions in table 4.7.

Peak intensities (integrated areas) show how much of a particular element is in the sample. The peak positions indicate the chemical bonding. Quantifying the VKE-XPS data requires that the number of recorded electrons is proportional to the number of electron at a given excited state in the film. Quantification of peak area is important in defining the range of elemental signals and allows for the subtraction of background noise not belonging to the element. Here we used the linear Shirley-Sherwood background subtraction method and avoided any overlapping Auger peaks. Results for the thick film can be seen in Table 4.8 and figure 4.9 and shows the normalized areas

for the thick film. Results for the thin film can be seen in Table 4.10 and figure 4.11 and shows the normalized areas for the thin film. Table 4.12 shows the IMFP (lambda) and Table 4.13 shows the values of sigma (photoionization cross section) used in all the calculations. Table 4.14 is R, the photoemission of the reference material.

Table 4.4: Peak positions for collecting XPS data for both the thick and thin TiO_2 films

	Peak Positions				
hv	Ti2p	O1s	C1s	Si1s - Si	Si1s - O
2150	1689.01	1617.61	1862.81		
2500	2035.02	1963.66	2208.84		651.89
3000	2536.68	2465.27	2710.45		1153.44
3500	3045.58	2974.14	3219.31	1665.9	1662.33
4000	3546.91	3475.49	3720.64	2167.24	2163.33
4500	4046.71	3975.3	4220.45	2667.02	2662.75
4950	4499.99	4428.53	4673.82	3120.2	3115.88

Table 4.5: Calculated binding energies.

	Approx. BE:				
hv	Ti2p	O1s	C1s	Si1s - Si	Si1s - O
2150	458.37	530.03	284.8	1838.23	1842.47
2500	458.34	529.83	284.8	1838.04	1842.27
3000	458.33	529.84	284.8	1837.97	1842.31
3500	458.29	529.81	284.8	1837.91	1842.29
4000	458.3	529.82	284.8	1837.87	1842.27
4500	458.242	529.79	284.8	1837.8	1842.17
4950	458.23	529.76	284.8	1837.89	1842.28

Table 4.6: Binding Energy Shift.

hv	Ti2p	O1s	C1s	Si1s - Si	Si1s - O
0	0	0	0	0	0
0.03	0.2	0	0.19	0.2	0.03
0.04	0.19	0	0.26	0.16	0.04
0.08	0.22	0	0.32	0.18	0.08
0.07	0.21	0	0.36	0.2	0.07
0.128	0.24	0	0.43	0.3	0.128
0.14	0.27	0	0.34	0.19	0.14

Table 4.7: Transmission Function, T.

hv	Ti2p	O1s	C1s	Si1s - Si	Si1s - O
2150	2.316766	2.375436	2.18904	2.8978	2.8978
2500	2.079793	2.123224	1.983399	2.8978	4.141269
3000	1.830676	1.861194	1.761775	2.8978	2.889257
3500	1.646783	1.669572	1.594728	2.335321	2.338223
4000	1.507711	1.525573	1.466539	2.005354	2.007452
4500	1.396912	1.411387	1.363322	1.778329	1.779979
4950	1.313626	1.325858	1.285113	1.623864	1.625167

Table 4.8: Peak Areas - Thick TiO_2 Film.

Peak AREAS:					
hv	Ti2p	O1s	C1s	Si1s - Si	Si1s - O
2150	858320.9	654139.5	68909.34		0
2500	207826	90035.95	14700.61		7672.519
3000	877317.9	380711.6	59123.33		13165.45
3500	1037966	505441.3	66921.24	2637.725	9335.688
4000	1992162	1034090	120015.4	23535.5	16543.78
4500	158065.8	85749.36	9241.51	4634.309	1574.454
4950	38587.16	24722.25	2616.219	2438.32	700.6876

Table 4.9: Normalized Areas – Thick TiO_2 Films.

	Norm Area:				
hv	Ti2p	O1s	C1s	Si1s - Si	Si1s - O
2150	33815.93	93446.37	24405.48	0	0
2500	11534.85	17111.2	7082.225	0	708.9958
3000	93335.42	132777.4	56815.87	0	1891.283
3500	156478.1	242070.6	90135.72	491.3088	1738.3
4000	501999.1	772437.8	263992.2	6009.256	4222.598
4500	52952.6	83421.63	26903.53	1466.388	498.0077
4950	19058.81	34118.91	11138.7	1001.225	287.6249

Table 4.10: Areas Thin TiO_2 Film, A.

	AREAS:				
hv	Ti2p	O1s	C1s	Si1s - Si	Si1s - O
2150	683255.7	870020.4	105013.9	5859.79	27620.97
2500	176630.3	85388.78	25003.47	159186.8	99539.33
3000	613860.4	312805.4	89683.92	1162960	378298.6
3500	463221.3	262140	70269.5	1889965	375862.3
4000	948405	573996.5	153675.4	5153588	745642
4500	401288.6	260205.7	72594.97	3165946	455622.9
4950	44563.96	79942.34	18262.36	482347.2	63557.76

Table 4.11: Normalized Areas Thin TiO_2 Film, [A].

hv	Ti2p	O1s	C1s	Si1s - Si	Si1s - O
2150	26918.75	124274.2	37189.9	543.2014	2576.923
2500	9803.721	32455.84	12045.24	14723.11	9192.507
3000	65307.06	218184.1	86179.51	167151.1	54324.56
3500	69834.2	251094.4	94643.26	352050.1	69969.75
4000	238980.4	857485.9	338013.1	1315838	190289
4500	134410.8	506188.5	211293.4	1001545	144080.4
4950	22010.25	110323.5	77747.15	198058.8	26089.06

Table 4.12: Inelastic Mean Free Path, λ.

	lambda				
hv	458	532	285	1840	1843
2150	7.492733	7.327088	7.866394	3.216065	3.200686
2500	8.231166	8.080664	8.572714	4.681439	4.67081
3000	9.183677	9.049027	9.491018	6.204355	6.196331
3500	10.0463	9.92336	10.32801	7.421556	7.414848
4000	10.84051	10.72667	11.10208	8.465623	8.459742
4500	11.58038	11.47388	11.8256	9.394398	9.3891
4950	12.20798	12.10701	12.44084	10.15796	10.15306

Table 4.13: Sigma, σ.

	sigma:				
hv	Ti2p	O1s	C1s	Si1s - Si	Si1s - O
2150	38.602	14.68	6.3128	37.679	37.679
2500	27.785	11.194	4.7	31.05	31.05
3000	14.76	6.214	2.396	21.58	21.58
3500	10.585	4.6	1.7355	17.192	17.192
4000	6.41	2.986	1.075	12.804	12.804
4500	4.8715	2.3168	0.8203	10.499	10.499
4950	3.333	1.6476	0.5656	8.194	8.194

Table 4.14: Photoemission of the reference material, R.

	R				
hv	Ti2p	O1s	C1s	Si1s - Si	Si1s - O
2150	25.38215	7.00016	2.823519	6.327025	6.296771
2500	18.01722	5.261813	2.075705	7.589556	10.82167
3000	9.399625	2.867293	1.040613	6.990746	6.961122
3500	6.633297	2.087992	0.74245	5.368772	5.370586
4000	3.968457	1.338736	0.454617	3.916541	3.917915
4500	2.985043	1.027903	0.343505	3.160356	3.161505
4950	2.024637	0.724591	0.234877	2.435338	2.436116

Chapter 5

RESULTS AND DISCUSSION

The methodology and the calculations to determine the concentration depth profile will be discussed by applying the method to *simulated spectra* and comparing different regularization methods that were described in the previous section. Then, using the insights and understanding acquired from the simulated runs, we will apply a similar technique to *experimental VKE-XPS data* on ~2-3nm and ~25-30nm actual TiO_2 films.

5.1 Simulated Data

5.1.1 Initial Model – Data Generation

The purpose of generating simulated data with a known profile is to test the applicability of various regularization routines to VKE-XPS. See Section 4.4.4 and Table 4.2 for explanation of the details on the specific regularization functions used in this study data that have been successfully demonstrated in AR-XPS [21].

An initial model of a completely homogeneous film was considered, such that the concentration of any element at any point is one divided by the total number of elements, resulting in a uniform distribution of elements, as shown in figure 5.1.

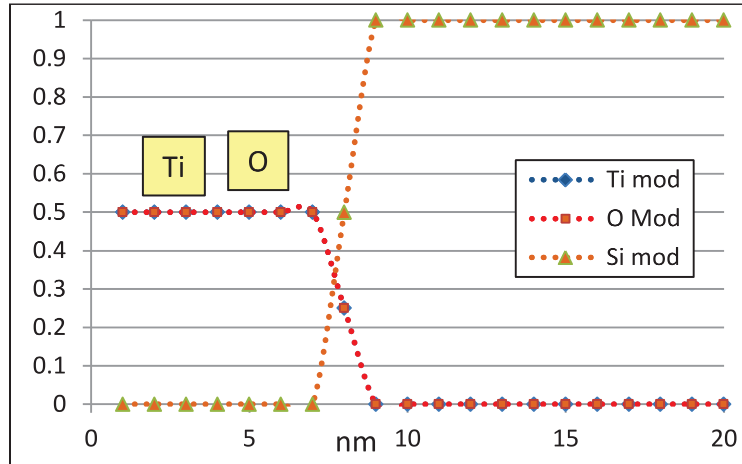

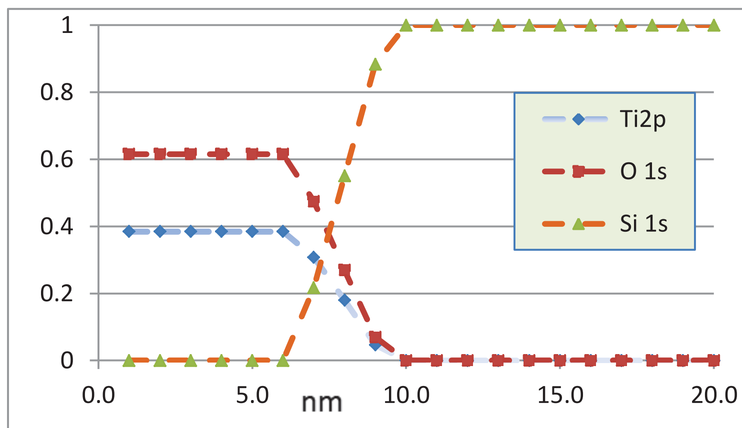

Figure 5.1: Top: Initial Homogeneous Model of 7.5nm film.
Bottom: 7.5nm simulated film for Ti2p, O 1s and Si 1s. Ref.82.

Spectra for each element in each layer were generated assuming a stoichiometry of Ti:O of 1:1. Each spectrum was attenuated by the IMPF given the kinetic energy of the generated electrons, the collection angle and the composition of the layers above. By adding the spectra generated from each layer, a total spectrum for each element at a given x-ray energy was produced. This calculation was repeated for each incident x-ray energy. Over-layer TiO_2 film thicknesses were varied between

1 and 15 nm, and an arbitrary 10% noise level was uniformly added into the spectra by adding a random number between -0.05 and 0.05. New noisy data were calculated prior to each calculation and used to determine the error bars and was also used as the variance for calculation of χ^2. This 10% noise level is typical of the actual measurement with VKE-XPS equipment.

The composition (fraction) of each element was calculated by dividing the integrated intensity, as modeled above, by the elemental sensitivity factors (as described in section 4.5.2) and normalizing. Thus, for each incident x-ray energy and film thickness, a fractional composition was calculated for each element.

Once the "raw data" for each TiO_2 film thickness and x-ray energy was determined, the Ent-model was applied to this system. The relative intensity comparisons for the various regularization functions are shown in figure 5.2. These simple initial models were chosen as it assumes minimal prior knowledge of the film structure, as is the case for any unknown film structure. For Ent-model, using the maximum entropy regularization, some prior knowledge such as film thickness is considered in the calculation, as might verified with other analytical techniques.

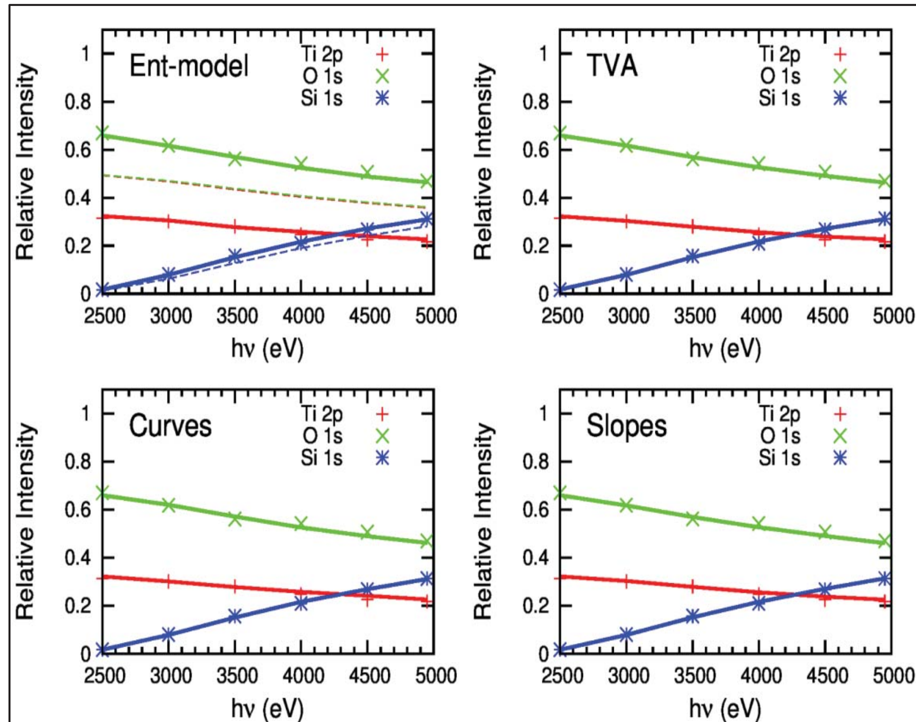

Figure 5.2: VKE-XPS Relative Intensity for simulated films (points), and the resulting regularization results (lines). For "Ent-Model", the initial model is shown in dashed lines. Ref 82.

Ent-model (maximum entropy) calculations may be performed using a homogeneous initial model as with the other regularization functions; however, this will weigh the results towards that model (initial estimate of the film) as the initial model is considered in the Ent-model regularization function in calculating S. If any accurate information about the film is known (prior knowledge) from other analytical techniques, such as specific elements, overall thickness or number of layers, the Ent-model regularization method, as we will see, produces the best concentration profile. This finding will have great impact in the final depth profile and will be discussed further below. Other regularization functions, Slopes and Curves, attempt to

regularize the calculated depth profile by limiting the total slope or curvature (smoothing routines) in the produced depth profiles and TVA regularization minimizes the total variance within the produced depth profiles. See section 4.4.4 for regularization details. These functions have been shown to provide excellent results for ARXPS depth profiling, do not need an initial "model" and will be applied here for comparison with VKE-XPS data [9].

5.1.2 Beam Energies

The accuracy of the final concentration depth profile depends on the intensity of the incident x-rays (improved signal to noise) and the number of beam energies used. To determine the optimum number of x-ray beam energies to scan, simulations on the 7.5 nm film were performed using different numbers of incident beam energies from 2.5 keV to 4.5 keV. The χ^2 (for the intensities calculated vs. measured) are plotted as a function of the number of beam energies in figure 5.3. For the simple 2-layer films considered, the χ^2 using 'Ent-model' is mostly flat with number of photon energies, showing little dependence on the number of beam energies scanned beyond five or six energies. It should be noted that the required number of x-ray energies acquired may be different for more complex film structures and in this case a calculation of the dependence of χ^2should be performed. For Total Variance Analysis (TVA), the χ^2 improves significantly until five beam energies, but it continues to improve subtly above five beam energies; though it never reaches the level of 'Ent-model.'

The observed difference between Ent-model and TVA is due to the nature of the regularization functions. For TVA regularization no initial model is assume. Conversely, a well-chosen Ent-model regularization with good prior knowledge will

ultimately limit the dependence on the number of data points. From these results, it was determined to use five beam energies for simulated and experimental analysis: 2.5KeV, 3.0KeV, 3.5KeV, 4.0KeV and 4.5KeV.

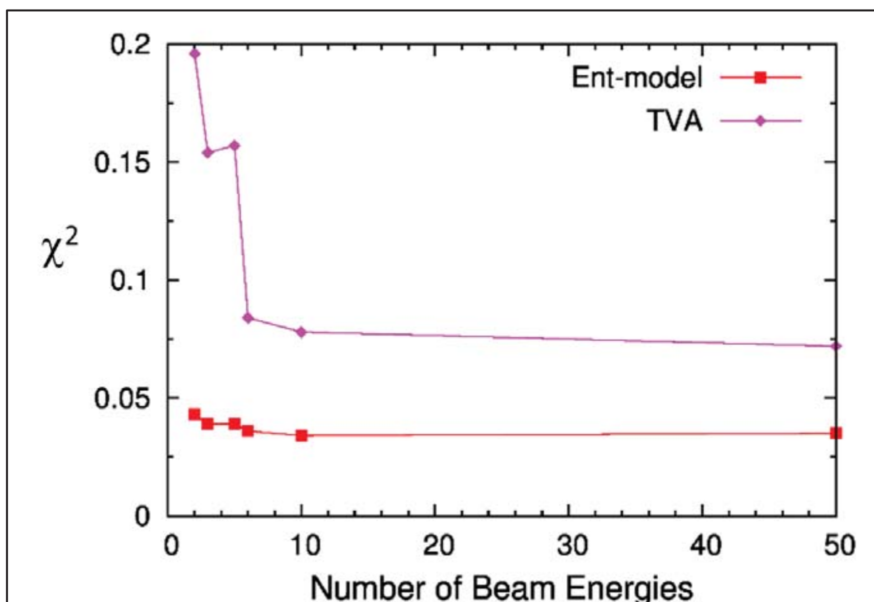

Figure 5.3: Dependence of "Goodness of fit",χ^2, on number of beam energies used for VKE-XPS. Ref. 82.

5.1.3 Depth Profiles

A simulated TiO_2 film of 7.5nm was chosen. Figures 5.4 and 5.5 show the VKE-XPS depth profile for that simulated TiO_2 film (points) compared with the results calculated using different regularization functions (Ent-model, Slopes, Curves and TVA). Calculations were performed with 50 noisy (10% randomly generated) data sets, and the average results are plotted. For Ent-model, the data for the initial model is shown in dashed lines since the other functions, Slopes, Curves and TVA do not need an initial model but the calculations use this as a starting point. The initial

model chosen was an 8 nm homogeneous Ti:O film, but other initial models were also used in subsequent calculations (1,3,5,10 and 15nm films – see below). It should be noted that the simulated film is thicker than the probe depth (commonly about a few nanometers) of a conventional lower energy, lab XPS source using ARXPS; a key advantage of VKE-XPS.

VKE with the Brookhaven system can range from 2.0keV to 6.0keV but the χ^2 for the number of beam energies reveals that five energies would be sufficient for confident data analysis. Figures 5.4 and 5.5 show excellent agreement for the data set for the depth profiles of the simulated 7.5nm film using Ent-model (χ^2=0.38), Slopes (χ^2=0.36), Curves (χ^2=0.18) and TVA (χ^2=0.11). The simulated film is shown in the dotted lines (perfectly covered by the solid regularization line), and the initial model for the Ent-model routine is shown in the dashed lines in Figure 5.4 (top). Similar results are seen for the Curves, Slopes, and TVA regularizations and, in all cases, the average Ti and O concentrations in the film and approximate film thickness are reasonably reproduced. Both the Ti and O signals decay into the Si substrate region. The O fraction appears to remain high at deep calculated depths. However, even using high beam energies, the contribution to the VKE-XPS signal from depths greater than 7.5 nm is not significant for this variation to greatly affect the simulated VKE-XPS intensities calculated as a function of incident x-ray energy (Figure 5.2). While the overall agreement is good, these artifacts in the "simulation" could imply interfacial broadening where none exists.

For Slopes, Curves and TVA, the best results are obtained at simulated film thicknesses less than 5 nm and the quality of calculation worsens as sampling depth increases. The Ent-model continues to have good agreement at depths up to 20-25nm.

This is likely due to the fact that the largest contribution to the VKE-XPS profile occurs in a 5nm or smaller depths with the strongest signal containing the most data. Results for Ent-model vary throughout the range of simulated film thicknesses. For thinner films, Ent-model produces fits similar in quality to Slopes; the 15nm simulated film shows the poorest fitting, while the overall best results were obtained when the simulated model film thickness is close to the simulated target thickness, as discussed above.

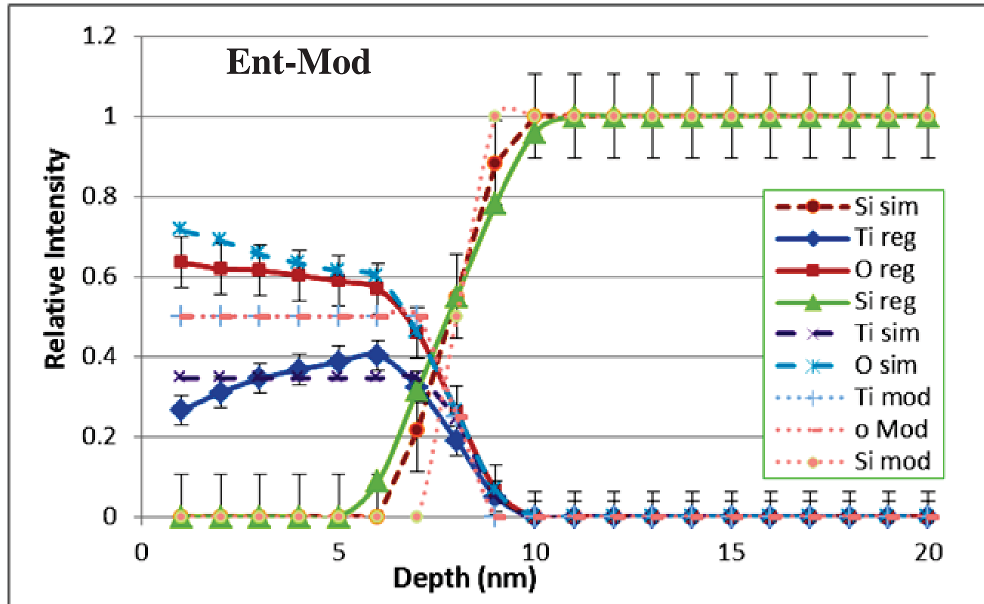

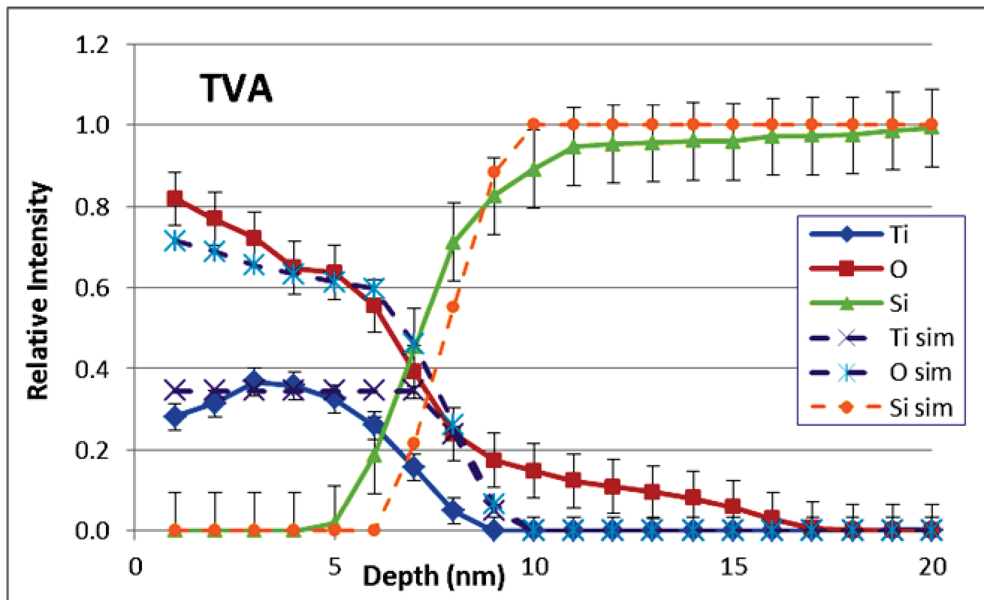

Figure 5.4: Depth profiles resulting from Ent-Mod and TVA regularization routines (solid lines). Initial Model: Dotted lines. Simulated films: Dashed lines. Ref. 82.

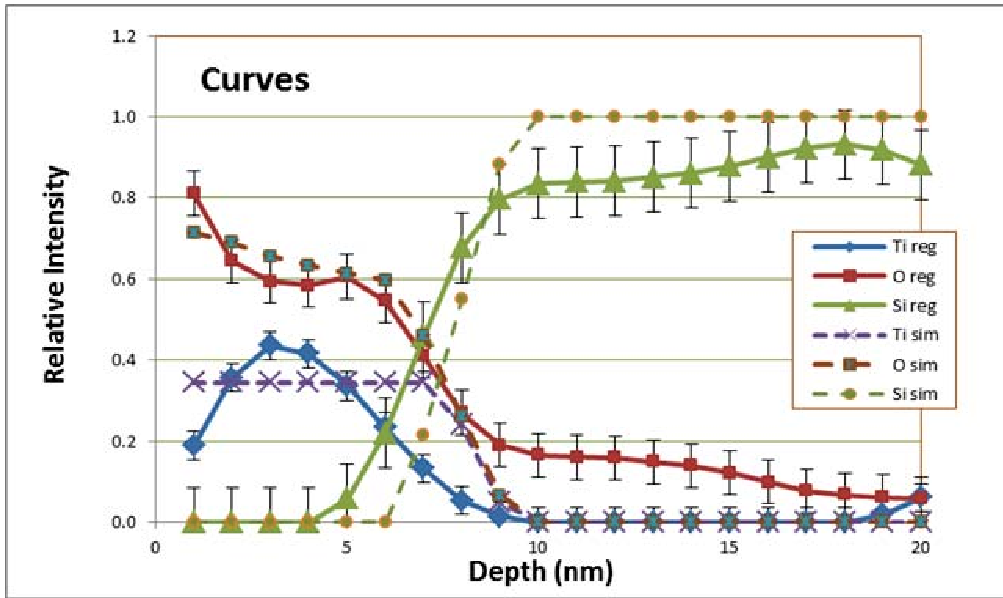

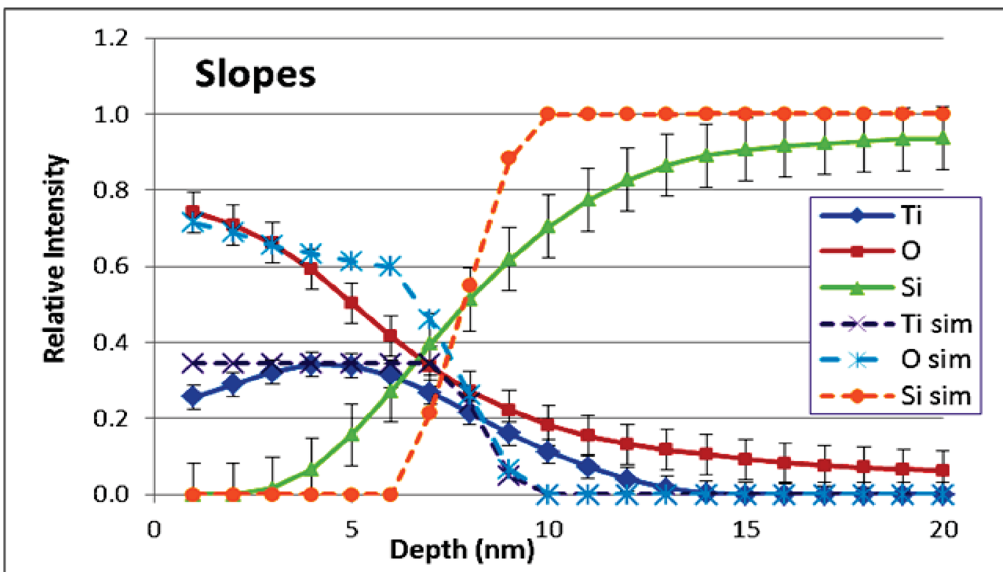

Figure 5.5: Depth profiles resulting from Curves and Slopes regularization routines (solid lines). Simulated films: Dashed lines. Ref. 82.

5.1.4 Ent-model: Maximum Entropy

As stated earlier, when the input model (8nm) is close to the simulated data (7.5nm), the correlation is better than when the model is distant from the simulated data (3nm or 10nm). This will greatly impact the analysis of actual data in that the model will need to be near the actual film thickness (prior knowledge) in order to generate an accurate depth profile. However, to test the utility of this routine when film thicknesses are not previously known, the routine was performed using initial models of 1:1 Ti:O films 1 nm, 3nm, 5nm, 8nm, 10nm and 15nm thick, calculated as described in section 5.1. The χ^2 of the simulated film and resulting depth profiles are plotted as a function of assumed film thickness (figure 5.6). Optimal results are obtained when the initial model is close to the 'real' film thickness, but the χ^2 is still reasonable when the initial model thickness is set to 5nm or 10nm. While there is some variation in the Ti and O concentrations in the film region, very little interface broadening is observed, and both Ti and O signals decay to zero in the substrate region (Ent-model in figure 5.4).

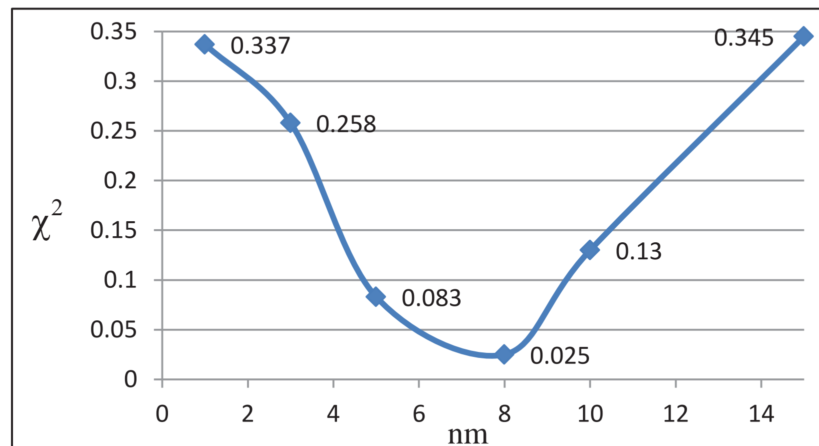

Figure 5.6: Dependence of χ^2 on the initial model thickness for the Ent-mod performed on a simulated 7.5 nm thick film. Ref. 82.

Looking at the regularization functions listed in Table 4.2, some dependence on the initial model is expected for 'Ent-model', as the initial model factors explicitly into the calculation ($m_{i,j}$). When the initial model used is similar to the simulated film, good results may be correspondingly expected but when the initial model is very dissimilar to the simulated film (example: a 100nm initial model for a 1nm film) the program may not converge, thus no depth profile can be generated. Prior knowledge of film thickness is common and the thicknesses can be measured in situ, during deposition or externally via Variable Angle Spectroscopic Ellipsometry, Auger spectroscopy, or Rutherford Backscattering Spectroscopy. However, it is important to note that, in cases where no prior knowledge exists, the 'Ent-model' routine may provide results leaning towards the initial model (even if it is inaccurate) and thus other regularization routines which do not weigh an initial model would be more applicable, such as Slopes and Curves. The χ^2 for the Ent-model routine with a homogeneous initial model (data not shown) was found to be 0.301, considerably worse than the other regularization routines, where χ^2 varied from 0.082 for Curves, to 0.106 for Slopes and 0.134 for TVA regularization [82].

The 'Ent-model' calculates the informational entropy between the produced depth profile and an initial model and will be applied to this data [23]. Since the regularization function for Ent-model has input from the initial model, a good initial model is important and results in significant improvement in the depth profile results. Figures 5.7, 5.8 and 5.9 show a plot of composition dependence on the initial model thickness of 3nm, 8nm and 10nm for the Ent-model routine performed on a simulated 7.5 nm thick film.

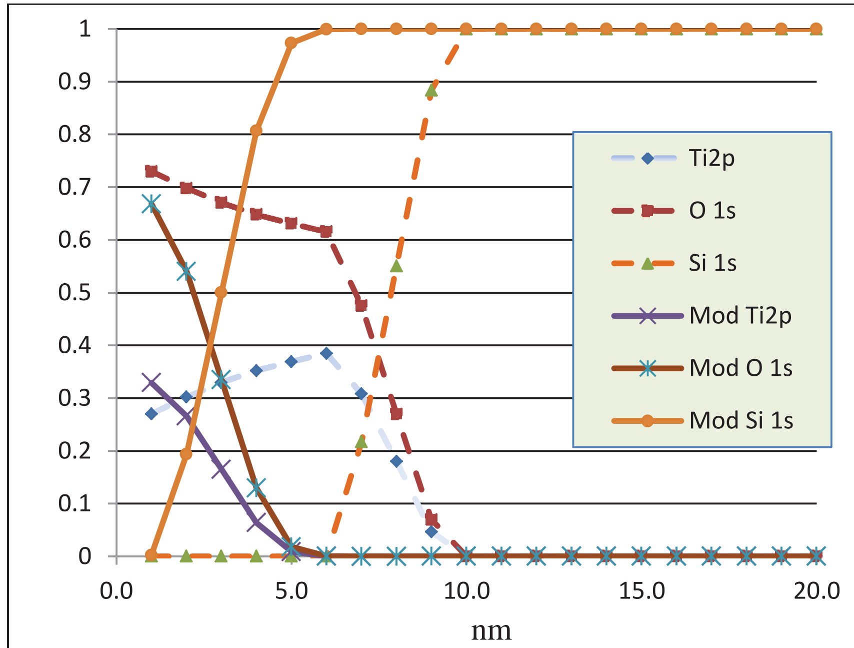

Figure 5.7: Plot of fractional composition for the initial model thickness of 3nm for the Ent-model routine performed on a simulated 7.5 nm thick film.

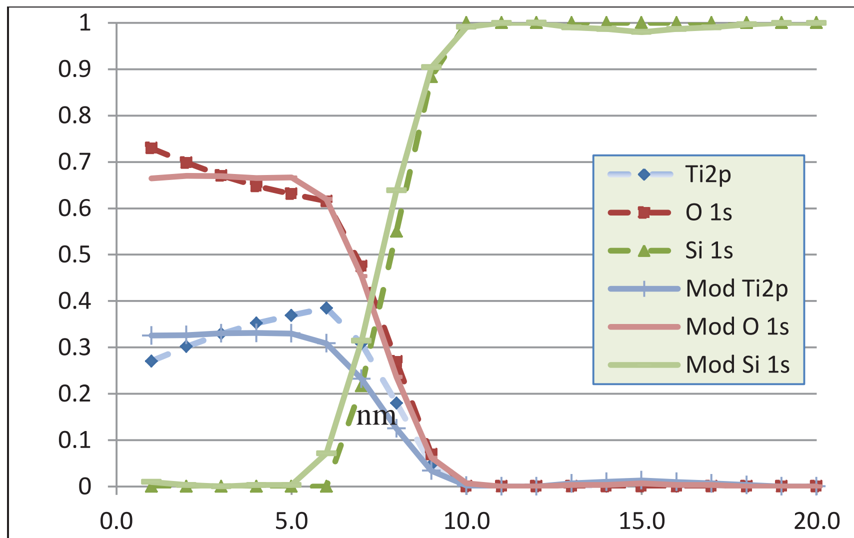

Figure 5.8: Plot of fractional composition of the initial model thickness of 8nm for the Ent-model routine performed on a simulated 7.5 nm thick film.

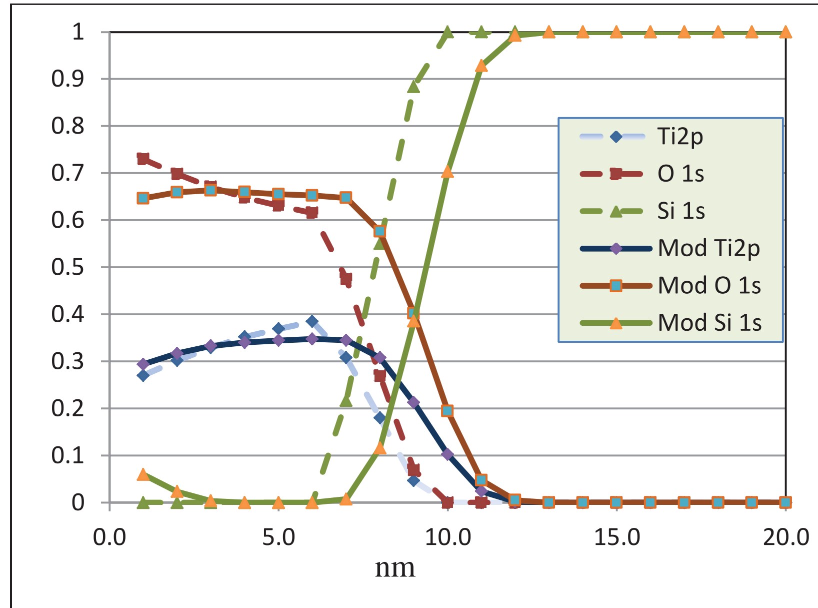

Figure 5.9: Plot of fractional composition for the initial model thickness of 10nm for the maximum entropy routine performed on a simulated 7.5 nm thick film.

It is instructive to consider the contribution to the total signal arising from each slab (equation 4.3) since errors in the calculated concentrations as functions of depth cannot be easily calculated from the routine. But for a material with constant concentration over the entire analysis depth, the slab located at a depth of 2λ contributes just 1% to the total signal. That is, a difference of 100% (Δn/n) in the concentration in the slab at that depth would result in a change of just 1% to the total measured intensity [21]. For heterogeneous films like those simulated here, the total contribution will depend on the concentration profile. For the Ti and O profiles presented here, the contribution to the total signal arising from beyond 2λ is expected to be less than 1%, so the depth profiles in figure 5.4 and 5.5 arising from the

regularization routines of the simulated film accurately fits the data shown in figure 5.6.

5.1.5 Initial Model – The Starting Point

As stated earlier, the other regularization functions tested have no explicit dependence on the initial model and may thus be more useful when there is no prior knowledge on the sample structure. In these cases, (Slopes, Curves and TVA), the initial model is merely the starting point for the $m_{i,j}$ values (see Table 4.2). Even so, some dependence on the initial model may arise due to "local maxima" in Q, that can be avoided by widening the search area and moving the starting $m_{i,j}$ point further away from the initial $m_{i,j}$ and determine if the results are the same. If the new results are different, the original "starting point" restricted the calculations in a local maximum in Q.

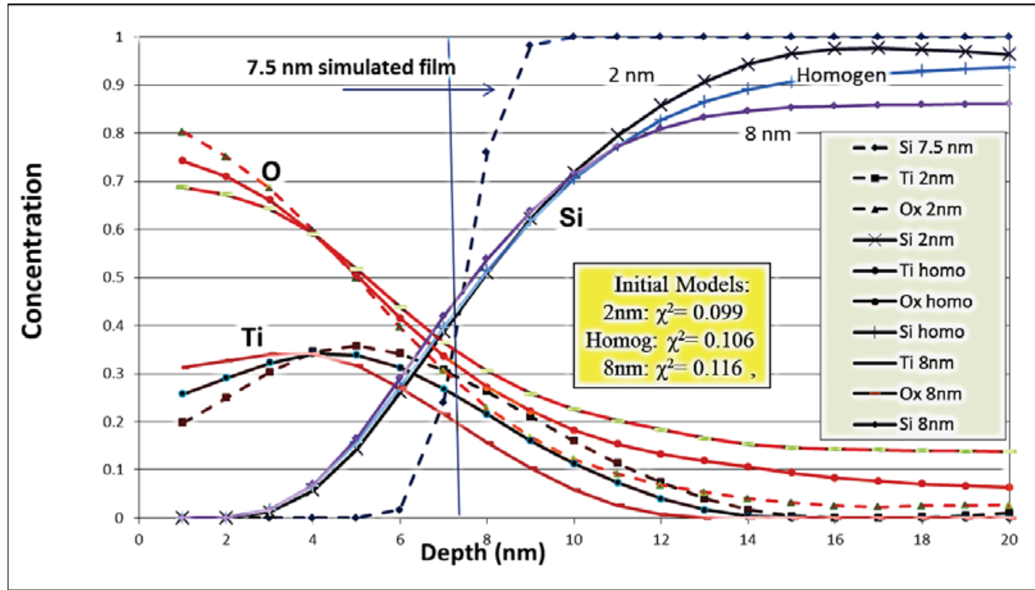

Figure 5.10: "Slopes" depth profile from 7.5nm simulated TiO_2 film. Homogeneous initial model (pluses in blue); 8nm 1:1 Ti:O initial model (diamonds); 2 nm 1:1 Ti:O initial model (crosses);
Simulated film structure (dash line). Ref. 82.

The 'Slopes' regularization function was performed with a 7.5nm thick simulated film, using three initial models: as shown in Figure 5.10: a homogeneous film, an 8 nm 1:1 Ti:O initial model, and a 2 nm 1:1 Ti:O initial model. As above, new noisy data was generated for each calculation. With the homogeneous initial model, the concentrations near the surface of the film are reproduced, yet the result shows significant interface broadening and the Ti and O signals do not decay to zero in the substrate, as they should. This interface broadening is the result of minimizing the slopes since a sharp interface would have a very high slope. Not having the Ti and O signal decay to zero at the interface shows the limitation of the technique when dependent on the initial model. Using the more realistic 8 nm initial model (closer to the 7.5nm simulated data) leads to some improvement, with the Ti and O signals

decaying to or near zero in the substrate region. Note the interface broadening is still present, as it should be with minimizing the slopes. The χ^2 values for the homogeneous initial model is χ^2= 0.106, for the 8 nm initial model is χ^2= 0.116 and finally the 2 nm initial models is χ^2= 0.099; Still very good results. Signals from elements of lower concentration from deep within the sample contribute minimally to the overall measured intensity, and thus do not significantly affect Q in the regularization routine. Thus, in these deeper regions, the program has no impetus to change the values significantly from the initial model, leading to the observed initial model dependence. The results graphed in figure 5.10 demonstrate that the initial model dependence is minimal, yet even so the best results are obtained when there is more prior knowledge available [82]. Note: TVA and Curves regularization function was performed with a 7.5nm thick simulated film, using three initial models and had similar results.

5.1.6 Noise Level vs. Goodness of Fit

Even with a regularization function, some noise-dependence may still exist, especially as noise levels increase [101]. Regularization functions are employed to reduce the dependence of depth profile reconstruction extraction on the collected noise. In other words, the Ent-model solution searched for all S (in table 4.2) for all possible depth profiles $n_{i,j}$, subject to the condition that the calculated data agrees with the measured data, within the noise, [21]. To ensure that the results are consistent with noisy data, the above calculations for each regularization function were repeated fifty times with different simulated 10% random noise; results were shown in figures 5.2 through 5.10.

Recall the χ^2 measures the difference between a model and the data (actually the sum of all the squares of the deviations divided by what was expected), so a low χ^2 is evidence that the model is correct and has a high probability of explaining the measured data. If χ^2, calculated from n vs depth is very large, either the data measurement technique was compromised (incorrect) or the model is wrong. The χ^2 for the Slopes function was found to range from 0.044 to 0.242, with an average value of 0.102. For Curves the range was from 0.040 to 0.240 with an average of 0.092. TVA ranged from 0.033 to 0.235 with an average of 0.072. For Ent-model with an initial model that was homogeneous throughout, the range was from 0.297 to 0.302, with an average of 0.300. Again, the optimal results were found with Ent-model using an initial model with thickness (8 nm) similar to that of the simulated film (7.5 nm), where the χ^2 ranged from 0.033 to 0.036 with an average of 0.036. The best value of χ^2 for Ent-model is well below even the best χ^2 value obtained from the other regularization techniques, showing the observed results are not an artifact due to the noise dependence. These results can be expected from consideration of the regularization functions in Table 4.2. The contribution to the Ti and O signals coming from greater depths to the total intensity is minimal, so there can be large variations in their ni,j without greatly affecting χ^2. The regularization routine has more flexibility to maximize S, resulting in films with minimum Slope, Curvature, or Variance, which do not match the films in these instances. Again it should be stated that the Ent-model routine works best when some prior knowledge of the sample exists; i.e. with an initial model (thickness) similar to actual structure. With no prior knowledge, Slopes and Curves may provide better result, as seen previously with ARXPS data [23].

5.1.7 Selection of Regularization Parameter – Weighting Factor

χ^2 results from all tested regularization functions for simulated films of different thicknesses are plotted in figure 5.11. For Ent-model, the 8nm thick 1:1 Ti:O initial model was used for every simulated film thickness, which explains the poor fit for any thickness other than that. In addition the stoichiometry of real Ti:O films is closer to 2:1 than 1:1. For Slopes, Curves and TVA, best results are obtained for initial film thicknesses less than 5 nm and the quality of fit decays as initial film thickness increases. This is likely due to the fact that the biggest contribution to the VKE-XPS profile occurs in a 5nm depth with the strongest signal containing the most data. Results for Ent-model vary throughout the range of tested initial film thicknesses. For thinner initial films, Ent-model produces fits similar in quality to Slopes; the 15nm thick initial film shows the worst fitting, while the overall best results were obtained when the model film thickness is close to the real thickness, as discussed above. Since thickness measurements were taken by VASE for the TiO_2 films, the Ent-model routine with a good initial model (known thickness) will be considered for experimental data, as discussed below.

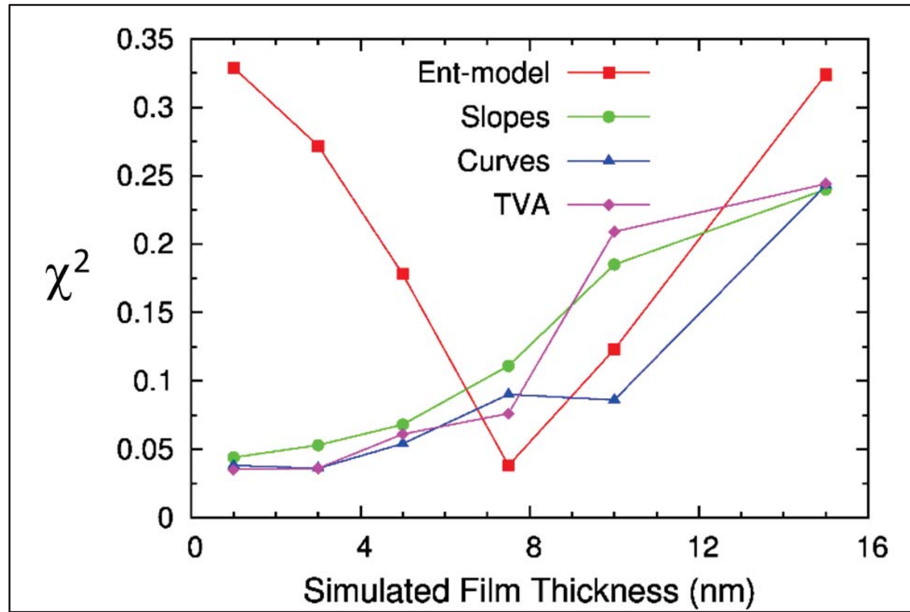

Figure 5.11: "Goodness of fit", χ^2, results for the different regularization functions at different simulated film thicknesses. Ref. 82.

The χ^2 results for the regularization functions using initial film thickness of 7.5 nm for data derived from an 8.0 nm film are graphed in figure 5.11:

- Slopes: 0.044-0.242 (avg 0.102);
- Curves: 0.040-0.240 (avg 0.092);
- TVA: 0.033-0.235 (avg 0.072);
- Ent-mod (initial model ~ actual film): 0.033-0.038 (avg 0.036)

As stated earlier, the regularization parameter, α, acts as a weighting between regularizing the data and fitting to the χ^2 value. To test the robustness of the α selection method, χ^2 values were calculated for depth profiles using each α value. Results are shown in figure 5.12. Since thickness measurements were taken by ellipsometry for the TiO_2 films, the Ent-model routine with a good initial model (known thickness) will be considered for experimental data, as discussed below.

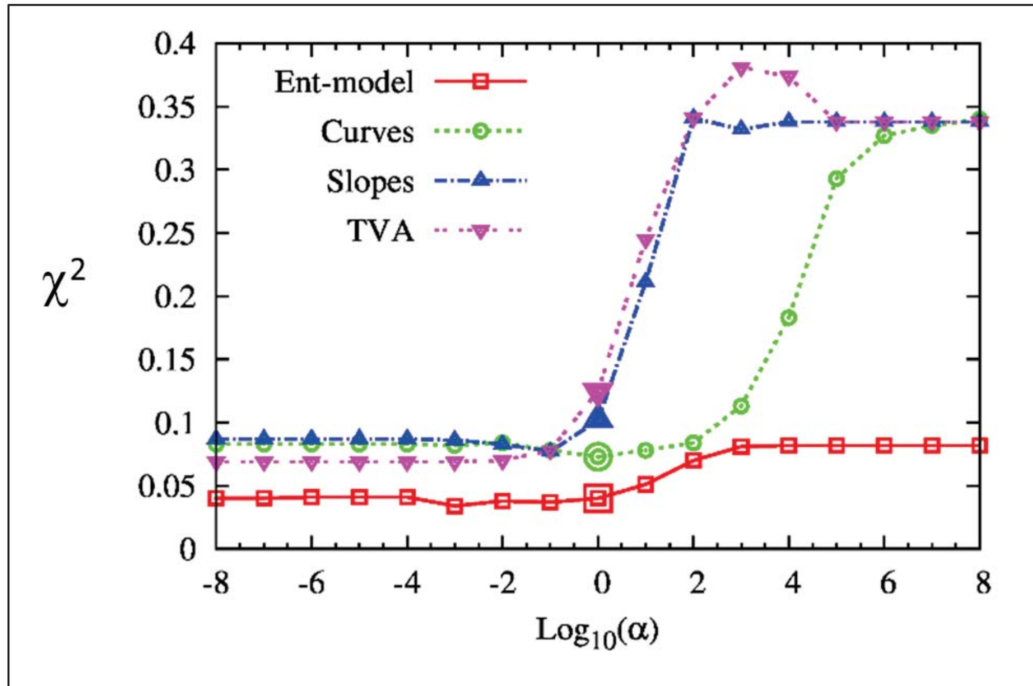

Figure 5.12: Goodness of fit, χ^2, for profiles produced using a 7.5 nm generated TiO_2 film at all values for α. The α values selected by the program are highlighted by the outlined symbol. Ref. 82.

As plotted in figures 5.6 through 5. 9, a 7.5 nm generated film was used, with a homogeneous initial model for the Curves, Slopes, and TVA functions, while an 8 nm 1:1 Ti:O initial model was used for Ent-model. The α values selected by the routine are denoted with double-symbols in figure 5.12. A similar trend is seen for all regularization functions: the Curve regularization begins flat for low α values, where the data is primarily fit by χ^2 (fitting the noise), then increases dramatically towards higher α values, where the data becomes "over-regularized" (not fitting the data). The selected α values lie close to the start of the increase in the χ^2 showing the "balanced weighting" between fitting to χ^2 alone and over-regularization. The χ^2 for the selected value is at or near the lowest obtainable value within the α range, demonstrating the

robustness of the selection parameter. Further verification of this optimum α is obtained with the L-Curve analysis below.

5.2 Experimental Data: Thin and Thick Films

5.2.1 Comparison to Models (Carbon in/on Films)

As described earlier, actual TiO_2 films of two thicknesses: ~2.5 nm (thin) and ~25 nm (thick) were analyzed using Variable Kinetic Energy-XPS at Brookhaven National Labs. Because the interface between the TiO_2 and Si substrate is typically very thin, on the order of $3x10^{15}$atoms/cm^2 or as little as two to three monolayers, understanding the bonding, ordering and intermixing of atoms at the interface is extremely difficult. In CMOS and RAM microelectronics many of these issues are critical in understanding electron injection, and interface traps and charging [2, 7].

Since these films were specifically designed and grown for gate dielectrics using organic precursors, three known elements were studied and a fourth, carbon, was also considered. These elements were verified with alternate analytical techniques that confirmed the presence of all four elements (see Chap 3). Titanium (Ti 2p), Oxygen (1s), Silicon (1s), and Carbon (1s) regions were analyzed at photon excitation energies of 2500, 3000, 3500, 4000, and 4500 eV. Photoemission peaks are shown in figure 5.13 (~2.5nm thin film) and figure 5.14 (~25nm thick film) with the spectra corrected for the variation of the spectrometer transmission function and orbital photoionization cross-section with the photon energy of the Si1S peak. In addition, the Si 1s peak was separated into two components—the one at lower BE is assigned to elemental Si^0, while the higher energy peak is attributed to Si^{+4}, likely SiO_2.

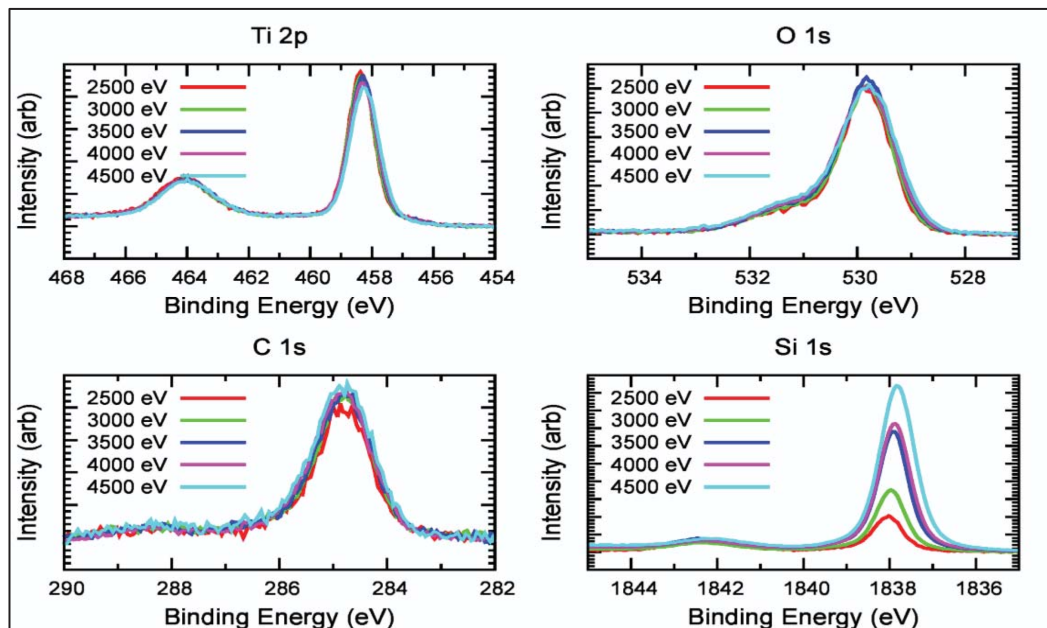

Figure 5.13: Photoemission of 2.5nm TiO_2 film on Si collected at various beam energies. Ref. 82.

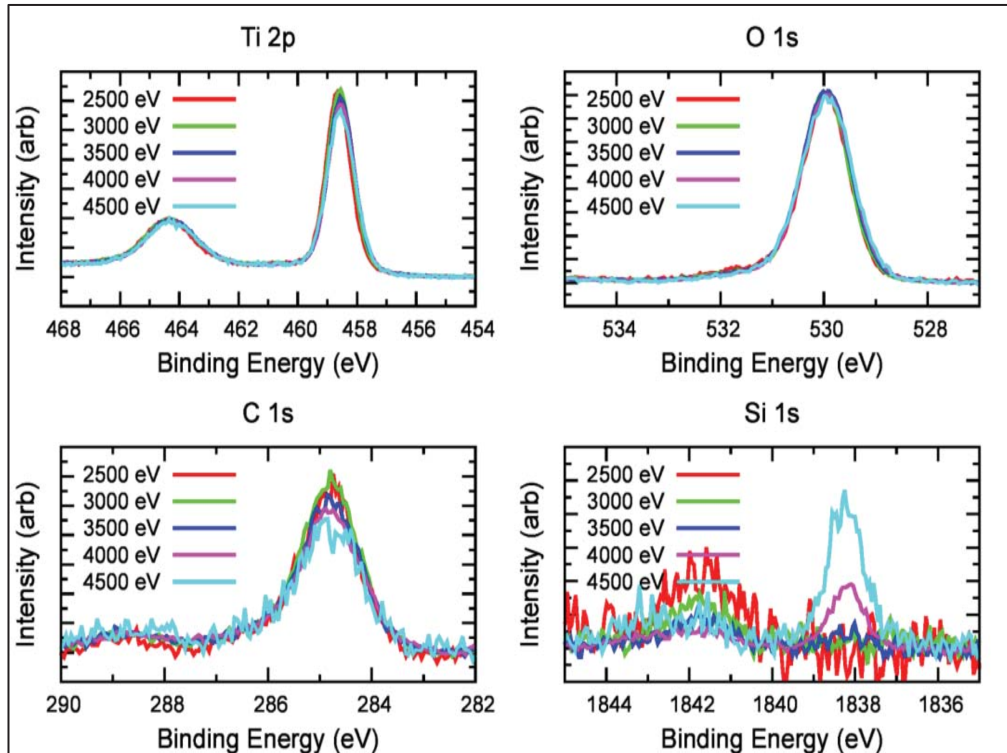

Figure 5.14: Photoemission of 25nm TiO_2 film on Si collected at various beam energies. Ref. 82.

5.2.2 Model Description

Various regularization functions used in the previous section were applied to the VKE-XPS data including Slopes, Curves, TVA and Ent-model as shown in Table 4.2. Except for the Ent-model, an initial starting point of a completely homogeneous film was used, so that the concentration of any element is one divided by the total number of elements. This model was chosen since it assumes minimal prior knowledge of the film. The initial model includes any information applicable to the film and is considered 'prior 'knowledge. Ent-model calculations could use the 'homogeneous' model (no prior knowledge) as used in the other regularization functions but since the initial model figures strongly in the calculations of S, good

prior knowledge must be used to improve the results. This prior knowledge is gathered in measuring and validating the thickness and elemental composition using alternate techniques, as described in chap 3. It will be shown that optimal results with the lowest χ^2 occur when the prior data (thickness, for example) is similar to the actual film. In cases where there is no prior knowledge, the Ent-model routine would not be appropriate as discussed in the "simulated spectra" (section 5.1). As an example, the χ^2 for the Ent-mod routine using a homogeneous prior model (data not shown) is 0.301. This is much worse that the TVA (0.11), Slopes (0.24) or Curves (0.11) which require no prior knowledge or model. But there is usually some knowledge about a film, even if it is only the thickness and elements.

Minimal information from the film vendor stated that the starting materials used in deposition the film contained titanium as an organic precursor, thus leading to the addition of oxygen and carbon into the models for this study. Since no special treatment was used to transport or store the finished films, it would be expected that carbon would adsorb on the surface from the CO_2 from the air or for carbon to be incorporated into the film from the cracking of the organic precursors, or both. There was no high temperature post deposition anneal, so concern about inter-diffusion of carbon at elevated temperature is remote.

5.2.3 Thin TiO_2 Films (2.5 nm)

For the thin film, as expected, the Si 1s photoemission signal shows a significant increase with beam energy, as more and more of the Si substrate is detected with increasing energy (figure 5.13). However, close analysis of the Si^{+4} components shows little variation in intensity (with respect to Ti) with beam energy. This may be suggestive of intermixing of Si^{+4} and TiO_2 at the interface or in the film. The C 1s

signals remain relatively constant (with respect to Ti) with increasing beam energy but the O 1s signal decreases with increasing penetration depth. The carbon does not appear to be surface-only. However, the possibility of a "U-shaped" C profile, with high concentration on the surface (adventitious C) and the film/substrate interface may not be resolvable given the beam energies investigated and the thinness of the film [82]. As the Si wafers were not pre-cleaned prior to TiO_2 deposition, C at the interface would not be unexpected due to adsorbed CO_2.

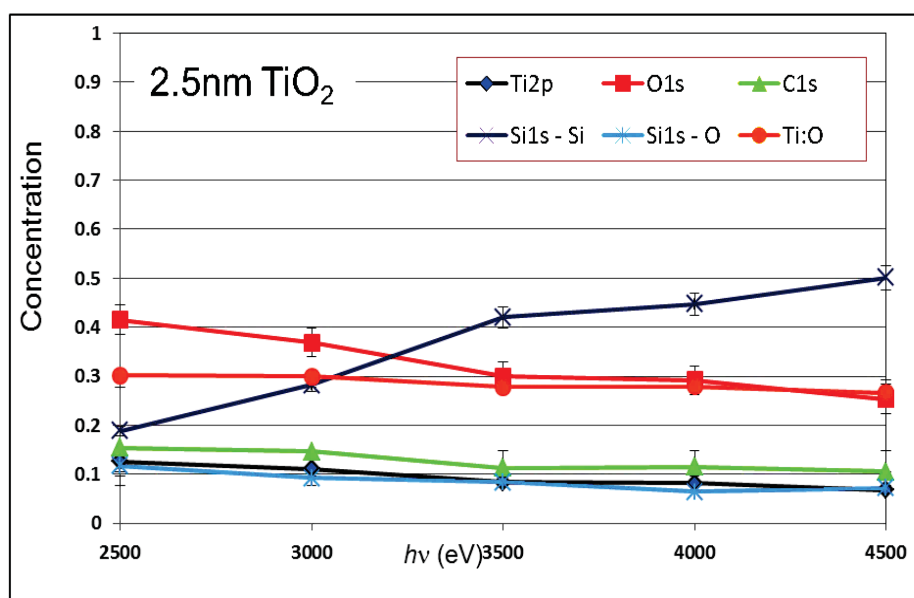

Figure 5.15: Atomic concentration v. depth for **2.5** nm TiO_2 films on Si. Error bars are estimated from the signal to noise ratio of the photoemission peaks.

Atomic concentrations were calculated according to equation 4.11 and are shown in figures 5.15 and 5.16. Error bars in the figure were estimated from the signal-to-noise ratio, by taking that value as the error in the intensity measurement and propagating that error through equation 4.11.

5.2.4 Thick TiO_2 Films (25nm)

Photoemission peaks of the "thick" film are shown in figure 5.14. Here, the O 1s signal remains constant with beam energy while the Si substrate signal increases dramatically, as seen in the "thin" film. In the case of the "thick" film, no Si substrate is observed at lower beam energies, consistent with the TiO_2 film's greater thickness. Only around 3500eV does the Si substrate begin to emerge. Interestingly, though, the Si-O signal is observed at all beam energies and decreases in intensity (relative to Ti 2p) with increasing photon energy, suggesting that the Si-O diffuses into the deposited TiO_2 film, (also seen in the "thin" film) but the high signal to noise and low overall intensity of the feature, (less than 2 atomic percent), makes it difficult to confirm this hypothesis. Finally, the C 1s signal follows a different trend in the "thick" film than in the "thin" film, decreasing in intensity with increasing beam energy, suggesting a higher concentration of C towards the surface, consistent with adventitious C contamination but still present throughout the film.

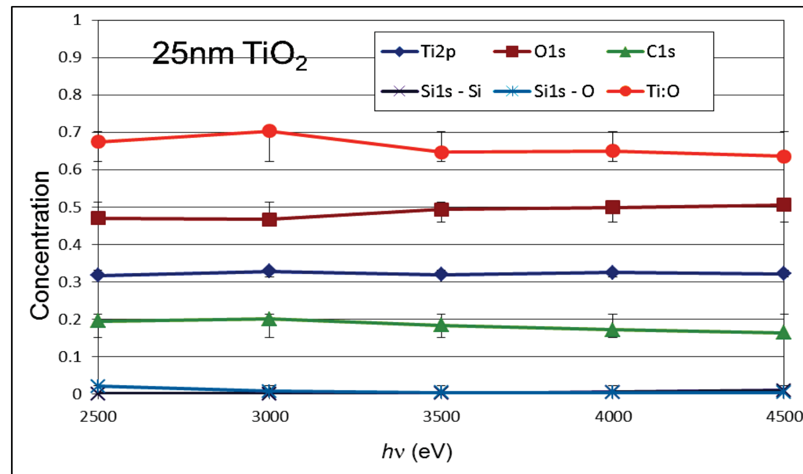

Figure 5.16: Atomic concentration v. depth for **25** nm TiO_2 films on Si. Error bars are estimated from the signal to noise ratio of the photoemission peaks.

5.2.5 Maximum Entropy Applied to Actual VKE-XPS Data

The Ent-model (maximum entropy) routine was applied to the VKE-XPS data from both thin (2.5nm) and thick (25nm) films to provide depth profiles of the two samples. The routine involves optimizing the regularization parameter α, to balance the noise with the data fitting. A verification of the α choice is done with the L-Curve (see below), which consists of plotting the log of the solution norm (S) vs. the log of the residual norm (χ^2) for a wide range of α values. Choose the value of α corresponding to the corner of the L-Curve results in an α used in the calculations to reconstruct of the depth profile, thus minimizing both the residual norm and the regularized solution norm simultaneously. It finds a compromise between the simplicity of the profile and the fit to the data. Figures 5.17-5.20 show the calculated α (insert) and the L-Curve (blue line) that are in excellent agreement for all four scenarios of thick and thin films with carbon on the surface or throughout the film.

5.2.6 L-Curves-Residual Norm vs Solution Norm

L-curve is an alternate method to generate the optimal α and is a graphical plot of the logarithm of the residual norm (entropy) of the functional Q versus the logarithm of solution norm (χ^2) showing the balance between these two functions as α varies. Choosing the value of α near the ‘corner’ of the plot (see blue arrows in figures 5.17 through 5.20) optimizes the function. In other words, the value of α is chosen for the reconstruction of the depth profile that minimizes both the residual norm and the regularized solution norm simultaneously (minimizing “d” in equation 4.9).

$$d = \sqrt{S^2 + C^2} \qquad (4.9)$$

This result creates a compromise between the simplicity of the profile and the fit to the data without incorporating too much noise by exactly fitting the data, noise and all. For this data, the best fit would be a regularization value of $\alpha \sim 0.02$, that balances the two considerations in the functional, Q; achieving a good fit to the data, and avoiding unphysical spikes and steps in the depth profile arising from over-fitting the noise in the data.

As shown in figures 5.17 through 5.20, the calculated value of α and the L-curve representation are aligned to balance both parts of the fitting function. Figure 5.17 depicts the compromise of the two joint functions resulting in an α of 0.001 for the "thin 2.5nm TiO_2 film" with carbon *modeled on the surface* of the film and the same α for the "thick 2.5nm TiO_2 film" with carbon *modeled on the surface* of the film (figure 5.18). Inserts in the figures are calculations from the program and show good agreement with the graphical representation in the L-curve. Similar result can be shown in figure 5.19 and 5.20 for carbon *modeled in the film* for the two different films.

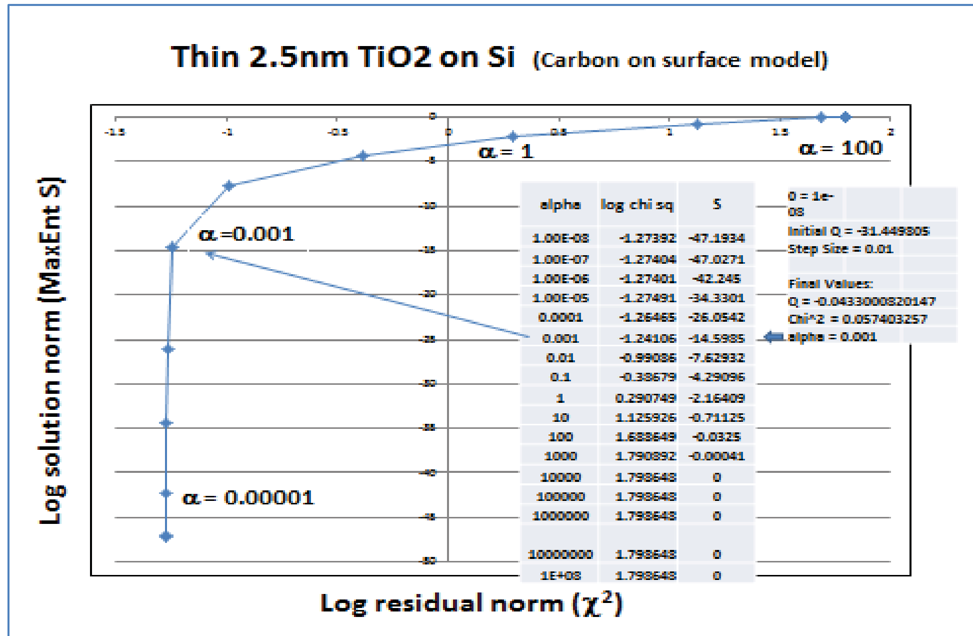

alpha	log chi sq	S
1.00E-08	-1.27392	-47.1934
1.00E-07	-1.27404	-47.0271
1.00E-06	-1.27401	-42.245
1.00E-05	-1.27491	-34.3301
0.0001	-1.26465	-26.0542
0.001	-1.24106	-14.5985
0.01	-0.99086	-7.62932
0.1	-0.38679	-4.29096
1	0.290749	-2.16409
10	1.125926	-0.71125
100	1.688649	-0.0325
1000	1.790892	-0.00041
10000	1.798648	0
100000	1.798648	0
1000000	1.798648	0
10000000	1.798648	0
1E+08	1.798648	0

Figure 5.17: L-Curve for thin (2.5nm): carbon modeled on the surface

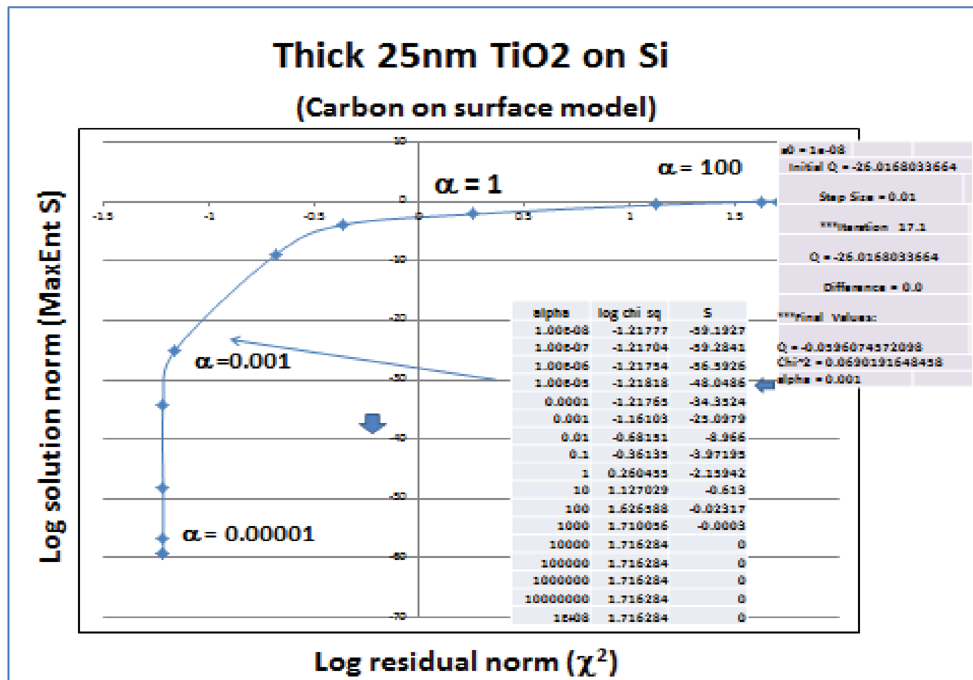

alpha	log chi sq	S
1.00E-08	-1.21777	-59.1927
1.00E-07	-1.21704	-59.2841
1.00E-06	-1.21754	-56.5926
1.00E-05	-1.21818	-48.0486
0.0001	-1.21765	-34.3524
0.001	-1.16103	-25.0979
0.01	-0.68151	-8.966
0.1	-0.36135	-3.97195
1	0.260455	-2.15942
10	1.127029	-0.613
100	1.626588	-0.02317
1000	1.710056	-0.0003
10000	1.716284	0
100000	1.716284	0
1000000	1.716284	0
10000000	1.716284	0
1E+08	1.716284	0

Figure 5.18: L-Curve for thick (25nm): carbon modeled on the surface

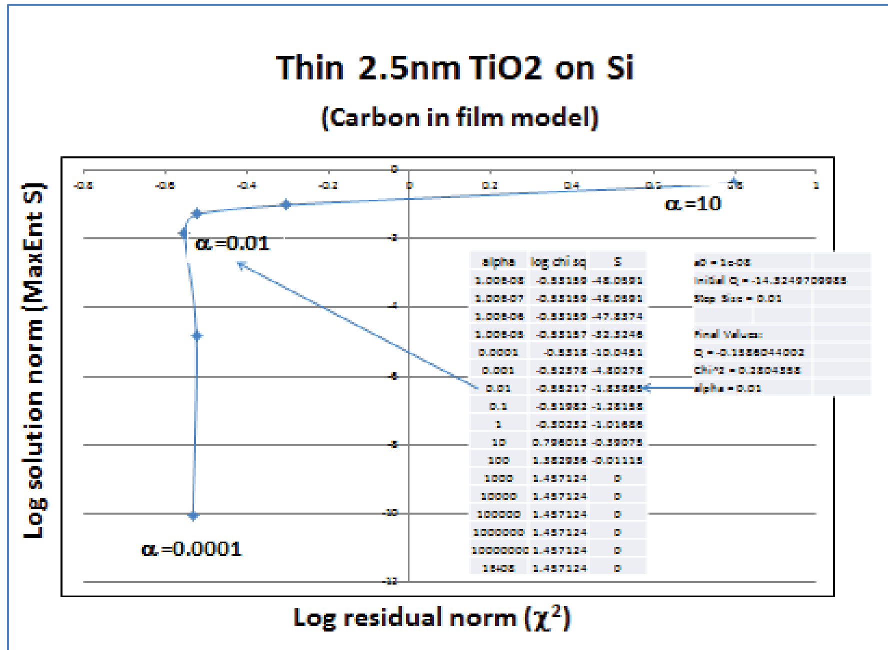

alpha	log chi sq	S
1.00E-08	-0.55159	-48.0591
1.00E-07	-0.55159	-48.0591
1.00E-06	-0.55159	-47.8374
1.00E-05	-0.55157	-32.3246
0.0001	-0.5518	-10.0451
0.001	-0.52578	-4.80278
0.01	-0.55217	-1.83885
0.1	-0.51982	-1.28158
1	-0.30252	-1.01686
10	0.798013	-0.39075
100	1.382936	-0.01115
1000	1.457124	0
10000	1.457124	0
100000	1.457124	0
1000000	1.457124	0
10000000	1.457124	0
1E+08	1.457124	0

a0 = 1e-08
Initial Q = -14.3249709983
Step Size = 0.01

Final Values:
Q = -0.1586044002
Chi^2 = 0.2804558
alpha = 0.01

Figure 5.19: L-Curve for thin (2.5nm): carbon modeled in the film.

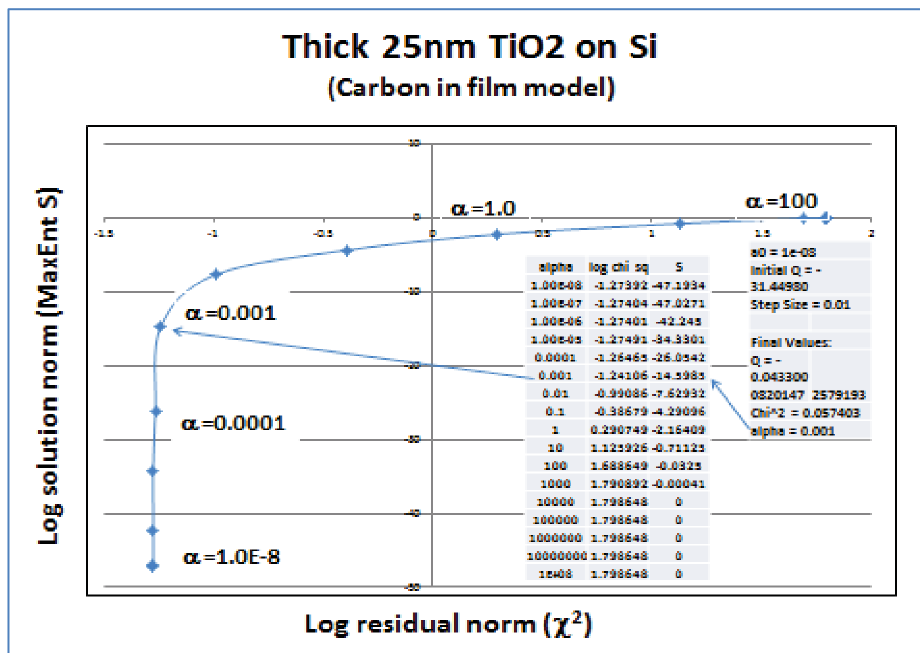

alpha	log chi sq	S
1.00E-08	-1.27392	-47.1934
1.00E-07	-1.27404	-47.0271
1.00E-06	-1.27401	-42.245
1.00E-05	-1.27491	-34.3301
0.0001	-1.26465	-26.0542
0.001	-1.24106	-14.5985
0.01	-0.99086	-7.62932
0.1	-0.38679	-4.29096
1	0.290749	-2.16409
10	1.125926	-0.71125
100	1.688649	-0.0325
1000	1.790892	-0.00041
10000	1.798648	0
100000	1.798648	0
1000000	1.798648	0
10000000	1.798648	0
1E+08	1.798648	0

a0 = 1e-08
Initial Q = -31.44980
Step Size = 0.01

Final Values:
Q = -0.043300 0820147 2579193
Chi^2 = 0.057403
alpha = 0.001

Figure 5.20 L-Curve for thick (25nm): carbon modeled in the film.

The χ^2 results for the different regularization routines are listed in Table 5.1; for the 2.5 nm sample, the optimal χ^2 is obtained for the TVA method, followed by the C through film initial model. For the 25 nm sample, results with the initial model of C through the film and TVA show a slightly lower χ^2 than the surface C initial model, though values for all routines are similar. The best χ^2 values are for models with carbon present throughout the film.

Table 5.1: χ^2 results different regularization routines for thin (2.5 nm) and thick (25 nm) TiO_2 films deposited on silicon

Regularization Function	Model	"Thin"	"Thick"
Ent-model	C on surface	0.660	0.075
Ent-model	C through film	0.445	0.060
TVA	N/A	0.270	0.058

The depth profiles shown in figures 5.21 to 5.23 are from VKE-XPS of 2.5 nm TiO_2 film deposited on Si using Ent-model figure 5.21 and 5.2 and TVA regularization in figure 5.23.

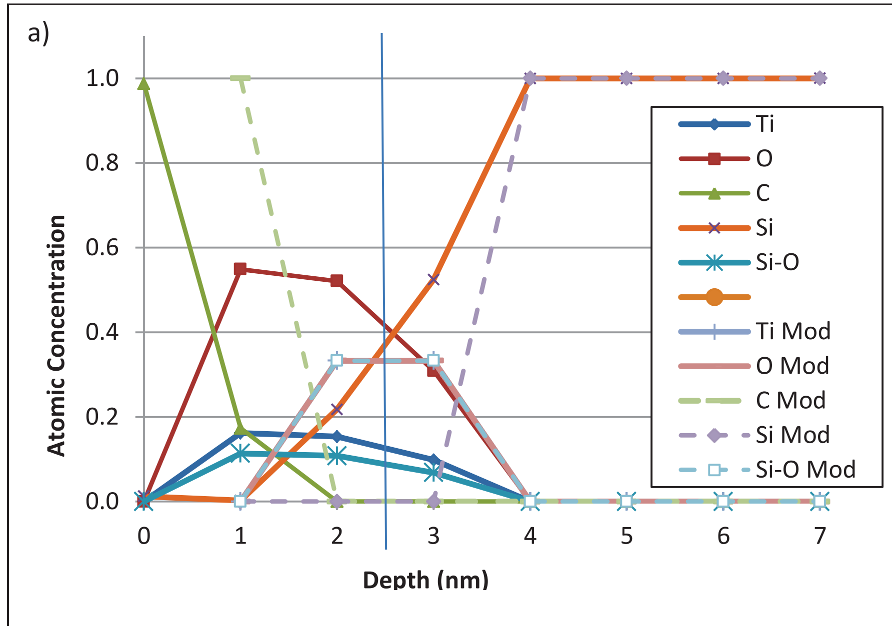

Figure 5.21: Depth Profiles found using Ent-model regularization. Model:1nm C on surface of a 2.5nm homogenous Si-O:Ti:O film. χ^2=0.660

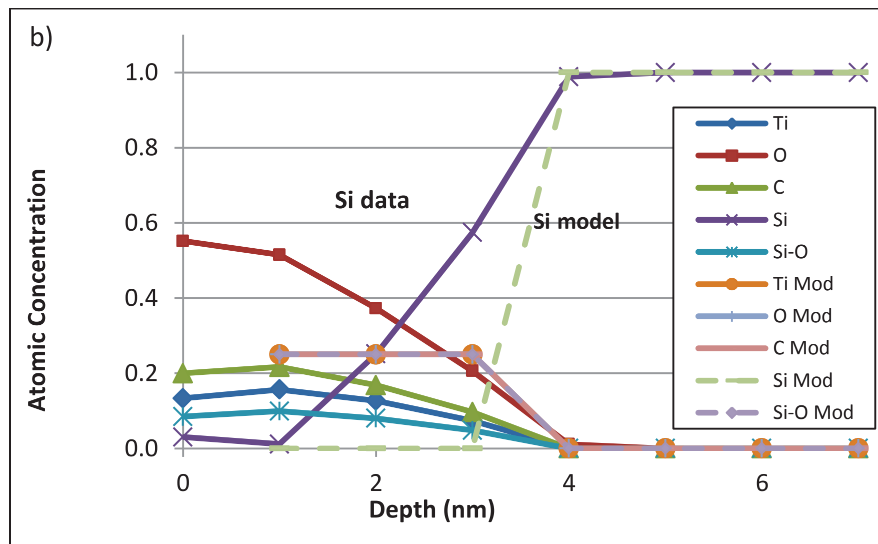

Figure 5.22: Depth Profiles found using Ent-model regularization. Model: C thru film-2.5nm - homogenous Si-O:Ti:O film. χ^2= 0.445

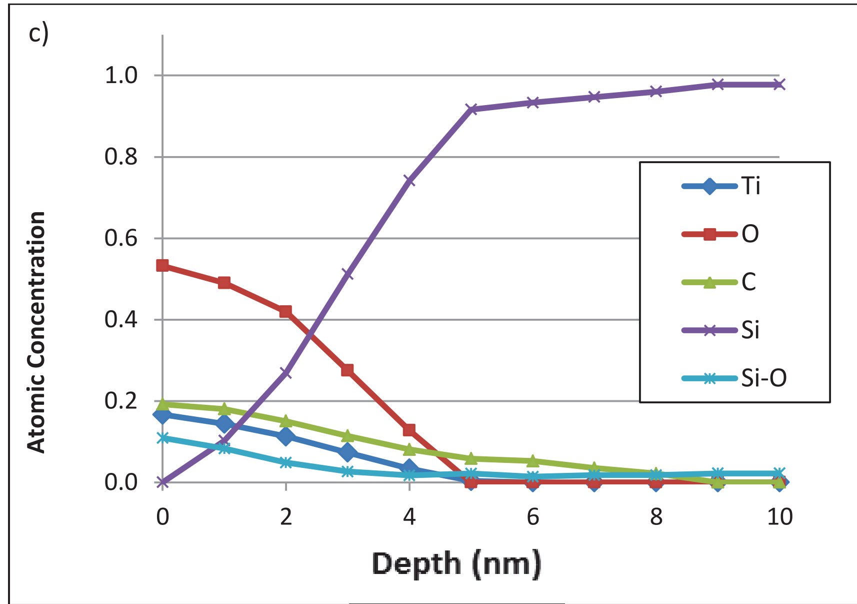

Figure 5.23: Depth Profiles – using TVA regularization on 2.5nm film.
No initial model. $\chi^2 = 0.27$

As described in the simulated data discussion, the Ent-model analysis was performed using a model consisting of 1 nm of surface C followed by homogenous Si-O:Ti:O film (figure 5.21) and a homogenous C:Si-O:Ti:O film (figure 5.22). Initial models are shown in the dashed lines.

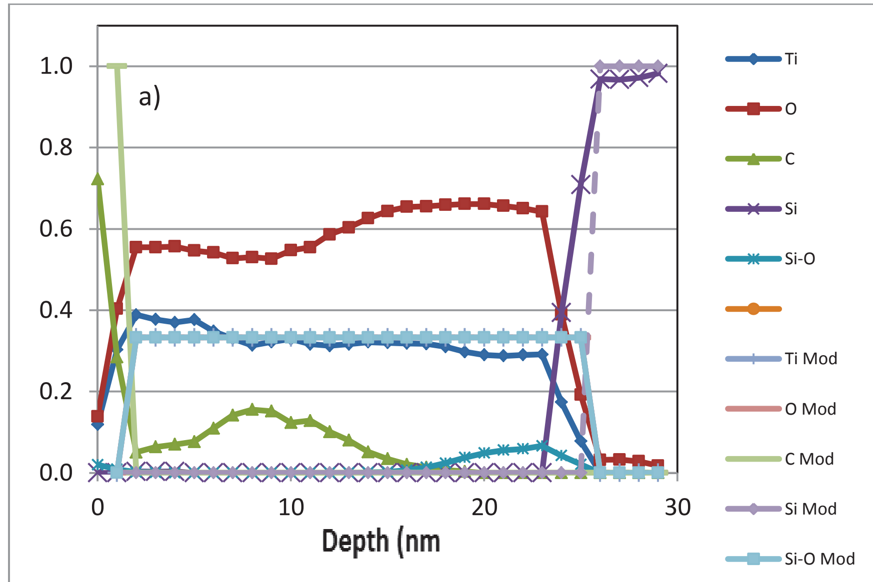

Figure 5.24 Ent-model: 1 nm C on surface- 25nm homogenous Si-O:Ti:O film. χ^2= 0.075. Ref. 82.

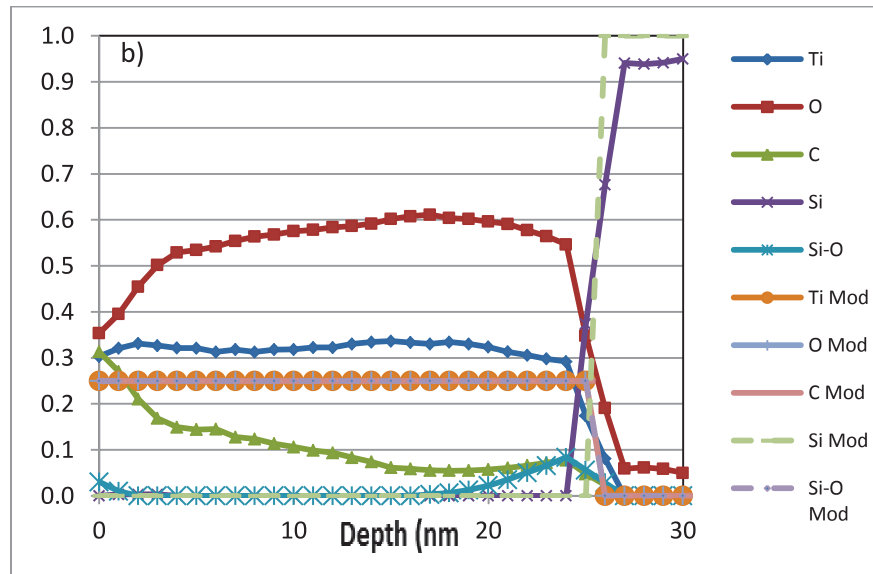

Figure 5.25: Ent-model: C thru film-25nm - homogenous Si-O:Ti:O film. χ^2=0.060. Ref. 82.

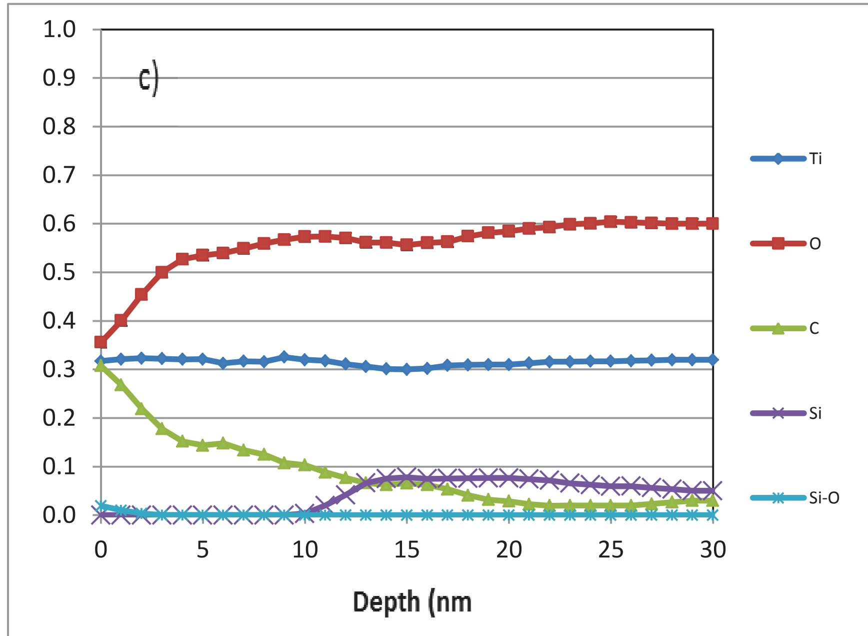

Figure 5.26: TVA regularization 25nm film.χ^2=0.058. Ref. 82.

The depth profiles (solid lines) shown in figures 5.24,5.25 and 5.26 are from VKE-XPS of 25 nm TiO_2 film deposited on Si using Ent-model (5.24 and 5.25) and TVA regularization (5.26). The TVA fit is unphysical but fits the data the best. Ent-model analysis was performed using a model consisting of 1 nm of surface C followed by homogenous Si-O:Ti:O film (figure 5.24) and a homogenous C:Si-O:Ti:O film (5.25). Initial models are shown in the dashed lines.

The routine was applied using two different initial models: first a homogenous Si-O:Ti:O film with all C on the surface, shown in figures 5.21 and 5.24 for the thin and thick films respectively. The second model assumed C throughout the film,

displayed in figures 5.22 and 5.25. The two separate models were chosen to test the dependence of the ultimate fit on the initial conditions. For both films, the overlayer thickness is taken as the total dielectric thickness determined from Ellipsometry. Regularization was also performed using the TVA method, shown in figures 5.23 and 5.26 to provide a further comparison. TVA was chosen as it provided the optimal results for a 3nm film with the simulated data and it does not require an accurate initial model (for thicker films, all regularization methods provided similar results for simulated data). Again, note that the TVA regularization has the best fit to the data (lowest χ^2) but has the least physical fit, confirming the concept that maximum entropy uses prior knowledge to restrict the determined profiles to those that are the most physical.

5.2.7 Concentration Depth Profile of Measured Data

For the "thin" film, figure 5.21-5.23, the Ti, O, and Si profiles exhibit similarities within the film region (except the surface C) for all three analyses, demonstrating the strong correlation between the depth profiles and measured data. The Ti is found to be about 15% in the film, decaying into the sample. The Si-O tracks closely, offset approximately 5% lower than the Ti, as expected given the regularization profile used. The O signal is higher but likewise tracks from around 55% to 0 in the substrate. The major deviations in the Ti, O and Si profiles are at the surface, dependent on the C initial model, and the rate of decay of the O signal into the film, which is due primarily to the decreased C signal for the C on surface initial model.

As suggested, the Si-O signal is found throughout the film and not just at the interface, suggesting the Si-O diffuses into the deposited film or exists as Si-O-Ti as

complex bonds. However, given that the regularization profile assumes that the Si^{+4} oxidation state is distributed uniformly through the film, perhaps this is not surprising. The (Si+Ti):O ratio is found to be about 1:2 as expected for a mixture of SiO_2 and TiO_2. See TEM photo, figure 3.16.

The C profile does show some dependence on the initial model. However, even when the initial model starts with all C on the surface, the C profile shows some broadening into the film, suggesting some C contamination in the film. The χ^2 listed in Table 5.1 suggest a better fit to the measured data when the initial model contains C throughout the film. As mentioned earlier, the C in the film could arise during sample transfer or residual organic precursor on the surface of the film or the "U" profile mentioned above.

Using this technique, over-layer thickness is found to be between 4 and 5 nm, (defined as the point where the Si substrate concentration reaches 80%) as compared to 7.3nm using VASE. The differences between this thickness and the VASE results may be due to the IMFPs used for the calculation; here the calculations are performed assuming bulk-like TiO_2, which may not be accurate for so thin a film. Additionally, as mentioned above, elastic scattering effects have not been considered, which may lead to the thicker film results [96].

The thick film (figures 5.24-5.26) is determined to be between 26 and 27 nm using Ent-model in agreement with the VASE results of 25.5nm. For all three regularization routines, the C profile is strongest on the surface and decays into the film. Again, even with the initial model with all C on surface, some broadening is observed; however, the decay into the film suggests the C is mainly towards the

surface. The Ti:O ratio is found to be about 1:2 throughout the bulk of the film, as expected for TiO_2 [82].

The Si-O signal is confined to the interface for the two Ent-model profiles and shows only a small surface concentration for the TVA calculation, yet as seen in Table 5.1, the χ^2 is similar for all three fits. As mentioned above, the overall low intensity and signal to noise makes it difficult to firmly characterize this peak. This can be seen in figure 5.27, which shows the measured VKE Si-O data overlain with calculated VKE data from the depth profiles in figure 5.24-5.27.

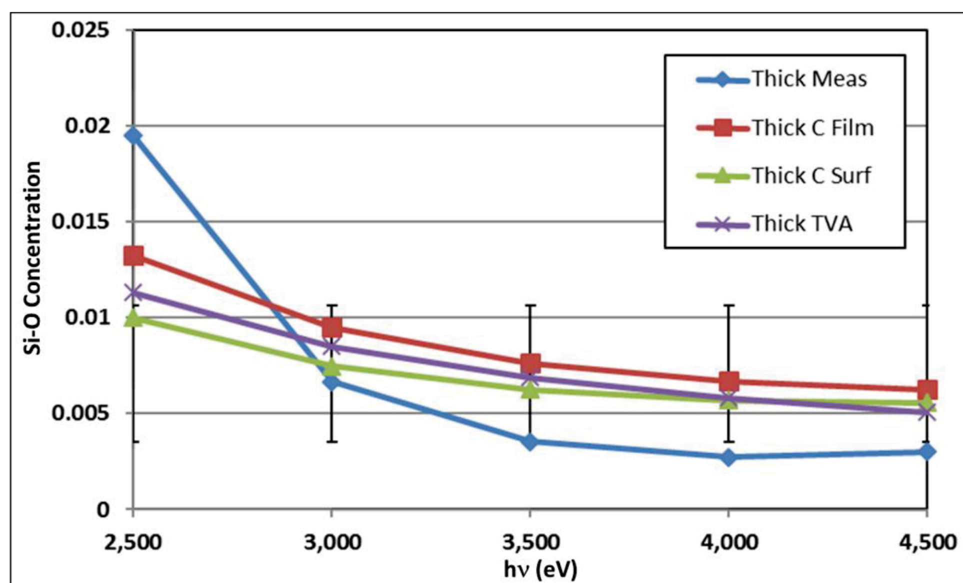

Figure 5.27: Measured and calculated VKE data for Si-O signal from 25 nm film. The error bars are estimated from the signal to noise ratio in the data. Ref. 82.

5.2.8 Limitations of the Technique

The Si profiles in the TVA results are significantly different than those for Ent-model – notably, the Si substrate is not observed in the 25 nm profile (the Si signal

never becomes the dominant feature), and very little to no Si-O is observed. These differences show the limitations of the technique with films of such large thicknesses measured in this beam energy range.

Most of the total photoemission signal for a given element comes from the first 2λ of thickness; for the Si 1s at hν = 4500 eV, that corresponds to slightly over 10 nm. The contribution to the total photoemission signal coming from greater depths is too low to be accurately calculated in the regularization routines without some ‘guidance’ or accurate initial models, as with Ent-model, evident from the χ^2 values in Table 5.1 It is still possible to draw some conclusions from the regularization routines especially within the first 10 to 15 nm of the film where the profiles from both regularization functions are similar. Notably, the C in this sample is located primarily at the surface (adventitious C), and the Ti:O ratio observed is consistent with TiO_2 demonstrating the integrity of the deposition.

5.3 Conclusions

The Ent-model (maximum entropy) algorithm has been utilized to determine depth profiles of actual dielectric films with Variable Kinetic Energy - XPS data. Using simulated noisy model data, the Ent-model regularization function was found to provide better results to regularization functions as compared to Slopes, Curvatures, or Total Variance. While optimal results were seen when the initial model for the Ent-model analysis contained additional knowledge about bulk composition and similar thickness to the simulated film thickness, results for other regularization functions showed little dependence on the initial model. This technique allows for the accurate determination of concentration depth profiles, even with poor or noisy data. The maximum entropy analysis was then applied to two TiO_2 films of different thickness,

and provided depth profiles demonstrating the applicability of the technique to experimentally noisy data.

Chapter 6

FUTURE WORK

6.1 Alternate Regularization Models

Future work will include applying different regularizations functions to better fit the MaxEnt composition depth profile other than Slopes, Curves and Total Variance (Table 4.2) as described in this paper. Although these regularizations adequately represent the correct depth profiles, the plots seem to show a flattening of the curves, signifying interface broadening due to inter-diffusions or possibly an artifact of the curve fitting process itself. It is known from the ALD deposition technique that the interface should be sharp, so better regularization functions that fit the data without this apparent interface broadening needs to be explored.

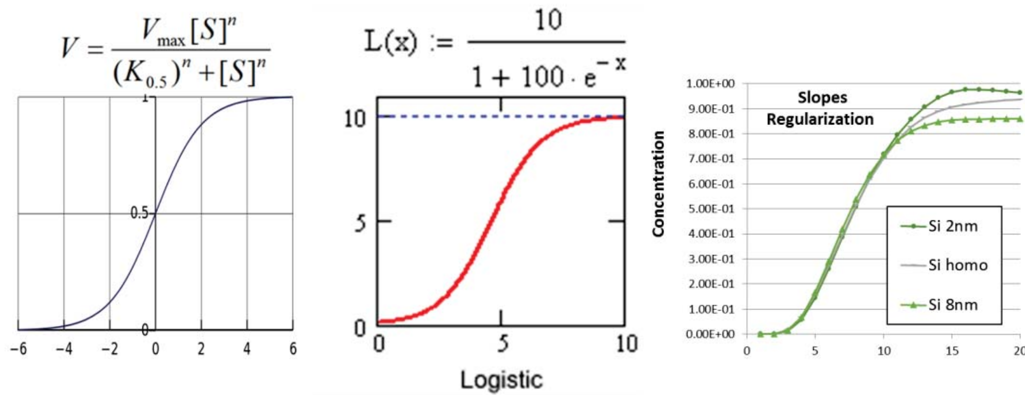

Figure 6.1: Hill Function on left; Logistic Function in center; Slopes Regularization used in this VKE-XPS study [106].

The Hill Function or Logistic Functions may fit this requirement since it's a logistic function or "S" shape sigmoid curve equation. The Hill coefficient controls the steepness of the curve and could generate a better fit to the VKE-XPS data. Further work need to be done to explore these other functions.

REFERENCES

1. R.L. Opila, J. P. Chang, M. Du, J. Bevk, Y. Ma, M. Weldon, Y. Chabal, and A. Gurevich, *Solid State Phenomena*, 65-66,257–260 (1999).

2. R.L.Opila, , G. D. Wilk, M. A. Alam, R. B. van Dover, and B. W. Busch, *Applied Physics Letters*, 81, 1788–1790 (2002).

3. J.P. Chang, M.L. Green, V.M. Donnelly, R.L. Opila, J. Eng, J. Sapjeta, P.J. Silverman, B. Weir, H.C. Lu, T. Gustafsson, E. Garfunkel, *Journal of Applied Physics* 2000, *87*, 4449.

4. A. Herrera-Gomeza, F.S. Aguirre-Tostado, P.G. Mani-Gonzalez, M. Vazquez-Lepe, A. Sanchez-Martinez, O. Ceballos-Sanchez, R.M. Wallace, G. Conti, Y. Uritsky, *Journal of Electron Spectroscopy and Related Phenomena* 184 (2011) 487– 500.

5. A. Herrera-Gomez, J.T. Grant, P.J. Cumpson, M. Jenko, F.S. Aguirre-Tostado, C.R. Brundle, T. Conard, G. Conti, C.S. Fadley, J. Fulghum, K. Kobayashi, L. Kövér, H. Nohira, R.L. Opila, S. Oswald, R.W. Paynter, R.M. Wallace, W.S.M. Werner, J. Wolstenholme, *Surface and Interface Analysis* 2009, *41*, 840.

6. E.H. Lock, D. Y. Petrovykh, P. Mack, T. Carney, R. G. White, S.G. Walton, and R. F. Fernsler, *Langmuir* 2010, 26(11), 8857– 8868.

7. R.L. Opila, J. Eng Jr, *Progress in Surface Science* 2002, *69*, 125.

8. R.W. Paynter, D. Roy-Guay, *Plasma Processes and Polymers* 2007, *4*, 406.

9. C. Claussen, M Sing, M Paul, G Berner, A Wetscherek, A Müller and W Drube, *Journal of Physics* 11 (2009) 125007.

10. C.S. Fadley Nuclear Instruments and Methods in Physics Research A 547 (2005) 24–41.

11. G. Panaccione, G. Cautero, M. Cautero, A. Fondacaro, M. Grioni, C. Henriquet, G. Monaco, M. Mulazzi, F. Offi, L. Paolasini, G. Paolicelli, P. Pittana, M. Sacchi, G. Stefani, P. Torelli, *Nuclear Instruments and Methods in Physics Research B* 246 (2006) 106–111.

12. J. Rubio-Zuazo, E. Martinezc, P. Batude, L. Clavelier, A. Chabli, G.R. Castro, *Applied Surface Science* 257 (2011) 3007–3013.

13. Y. Takata, M. Yabashi, K. Tamasaku, Y. Nishino, D. Miwa, T. Ishikawa, E. Ikenaga, K. Horiba, S. Shina, M. Arita, K. Shimada, H. Namatame, M. Taniguchi, H. Nohira, T. Hattori, S. Sodergreng,B. Wannberg, K. Kobayashi, *Journal of Electron Spectroscopy and Related Phenomena* 144–147 (2005) 1063–1065.

14. J. Rubio-Zuazo, G.R. Castro, *Journal of Physics: Conference Series* 2008, *100*, 012042.

15. J. Rubio-Zuazo, G.R. Castro, *Surface and Interface Analysis* 2008, *40*, 1438.

16. Y.Yonamoto, Y. Inab, N. Akamatsu, *Solid-State Electronics* 64 (2011) 54–56.

17. C.R. Brundle, G.Conti, P.Mack, *Journal of Electron Spectroscopy and Related Phenomena* 178–179 (2010) 433–448.

18. T.D. Bussing, P.H.Holloway, *J. Vac. Sci. Technol.* A 3 (5),p1973 Sep/Oct 1985.

19. P.J. Cumpson., Journal of Electron Spectroscopy and Related Phenomena 73 (1995) 25-52.

20. Mathew, A., K. Demirkan, R. Opila, C.-G. Wang, and G. Wilk, *ECS Meeting Abstracts*, 501, 659–659 (2006).

21. A.K. Livesey, G.C. Smith, Journal of Electron Spectroscopy and Related Phenomena 1994, 67, 439.

22. J.C. Brochon,, *Methods in Enzymology,* Vol40, p262 (1994)

23. R.W. Paynter, M. Rondeau, Journal of Electron Spectroscopy and Related Phenomena 174, 2011, 15-22.

24. U.C. Chung, D. Michau ,C. Elissalde, S. Li, A. Klein, M. Maglione, *Thin Solid Films* 520 (2012) 1997–2000).

25. T.D. Bussing, P.H.Holloway, *J. Vac. Sci. Technol.* A 3 (5),p1973 Sep/Oct 1985.

26. K.S. Butcher, T.L. Tansley, X. Li, *Surface and Interface Analysis*, Vol 25, 99-104 (1997).

27. H. Nohira, S. Shinagawa, M. Kase, T. Maruizumi and T. Hattori, IEEE, 0-7803-9339, 2005, 155.

28. Jaan Aarika,, Aleks Aidlaa, VaÈino Sammelselgb, Teet Uustarea, Mikko Ritalac, Markku Leskela, J. *Thin Solid Films* 370 (2000) 163-172.

29. P. Babelon, A.S. Dequiedt , H. Moste´fa-Sba, S. Bourgeois, P. Sibillot, M. Sacilotti. *Thin Solid* Films 322 _1998. 63–67.

30. V.G. Bessergenev, R.J.F. Pereira, M.C. Mateus, I.V. Khmelinskii, D.A. Vasconcelos, R. Nicula, E. Burkel, A.M. Botelho do Rego,. Saprykin. *Thin Solid Films* 503 (2006) 29 – 39.

31. C. Chaneliere, J.L. Autran, R.A.B Devine, B. Ballard,. *Materials Science and Engineering,* R22 (1998)269-322.

32. M.J. Colgan, M.J. B. Djurfors, D.G. Ivey, M.J. Brett, *Thin Solid Films* 466 (2004) 92– 96.

33. G.K.S. Dalapati, Chatterjee , S.K. Samanta, S.K. Nandi, P.K. Bose, S. Varma, S. Patil, C.K. Maiti, *Solid-State Electronics 47 (2003) 1793–1798*.

34. L. Dreesen, J. Colomer, H. Limage, A. Giguère, S. Lucas *Thin Solid Films* 518 (2009) 112–115.

35. I. E. Dunlop, S. Zorn, G. Richter, V. Srot, M. Kelsch, *Thin Solid Films* 517 (2009) 2048–2054.

36. E.O. Filatova1, I.V. Kozhevnikov, A. Sokolov, E.V. Ubyivovk1, S. Yulin, M. Gorgoi and F. Schäfers, *Sci. Technol. Adv. Mater*. 13 (2012) 015001.

37. D. Franta, I. Ohlıdal, D. Petrydes, *Vacuum* 80 (2005) 159–162.

38. M.-L. Kääriäinen, T.O. Kääriäinen, D.C. Cameron, *Thin Solid Films* 517 (2009) 6666–667.

39. J-H. Kim, S. Fujita, S. Shiratori, *Thin Solid Films* 499 (2006) 83 – 89.

40. J.J. Kim, E. Ikenaga, M. Kobata, A. Takeuchi, M. Awaji, H. Makino, P.P. Chen, A. Yamamoto, T. Matsuoka, D. Miwa, Y. Nishino, T. Yamamoto, T. Yao, K. Kobayashi, *Applied Surface Science* 252 (2006) 5602–5606.

41. Y.S. Liu, Y.H. Lin,Y.S. Wei, and C.Y. Liu, *Journal of Electronic Materials*, Vol. 41, No. 1, 2012.

42. Y. S. Liu, Y. H. Lin, Y. S. Wei, and C. Y. Liu. *J. Appl. Phys*. 111, 043103, 2012.

43. N. Martin, C. Rousselot, C. Savall, F. Palmino, *Thin Solid Films* 287 (1996) 154-163.

44. S.Meyer, R. Gorges, G. Kreisel. *Thin Solid Films* 450 (2004) 276–281.

45. M.G. Nolan, M.E. Pemble, D.W. Sheel, H.M. Yates, *Thin Solid Films* 515 (2006) 1956–1962.

46. J.S.Park, W-J Maeng, H-S Kim, J-Se Park, *Thin Solid Films* 520 (2012) 1679–1693.

47. S.S. Pradhan, S.K. Pradhan, V. Bhavanasi, S. Sahoo , S.N. Saran, S. Anwar, P.K. Barhai, *Thin Solid Films* 520 (2012) 1809–1813.

48. D. Rathee1, S. K. Arya1, M. Kumar, *World Journal of Nano Science and Engineering*, 2011, 1, 84-88.

49. B.S. Richards, S.R. Richards, M.B. Boreland, D.N. Jamieson, *J. Vac. Sci. Technol. A* 22.2., Mar/Apr 2004.

50. M. Ritala, M. Leskela, E. Nykanen, P. Soininen, L. Niinisto, *Thm Solid Films, 225* (1993) 288 295.

51. P. Eiamchai, P. Chindaudom, A. Pokaipisit, P. Limsuwan,*Current Applied Physics* 9 (2009) 707–712.

52. I. Karmakov, A. Konova, E. Atanassova, A. Paskalev, *Applied Surface Science* 255 (2009) 9211–9216.

53. T.W.H. Oates, H. Wormeester, H. Arwin, *Progress in Surface Science* 86 (2011) 328–376.

54. I. Ohlidal, F Lukes, *Applied Surface Science* 35 (1988-89) 259-273.

55. P. Sirok, J. Sobota , J. Seid and L. Jastrabi, *Thin SolidFilms, 234* (1993) 500-502.

56. M. Wimmer, M. Bar, D. Gerlach, R. G. Wilks,. Scherf, C. Lupulescu, F. Ruske, R. Fe´ lix, J. Hupkes, G. Gavrila, M. Gorgoi ,K. Lips,W. Eberhardt and B. Rech, *Appl. Phys. Lett.* 99, 152104 (2011.

57. J. Padayachee, K.A. Meyer, V.M. Prozesky, *Nuclear Instruments and Methods in Physics Research B* 181(2001) 122-127.

58. T.Chen, C. Luo, D. Wang, Y.Xiong, *Physics Procedia* 18 (2011) 136–142.

59. J. Orloff, L.W. Swanson, M.Utlaut, . *J. Vac. Sci. Technol. B* 14(6), Nov/Dec 1996.

60. S. Reyntjens, R. Puers, *Micromech. Microeng.* 11 (2001) 287–300.

61. G.A.Cooke, M.G.Dowsett, P. Phillips, *J. Vac. Sci. Technol. B* 14(1), p 283 Jan/Feb 1996.

62. T. Dyson and S. Rao, *Signal Processing* 2 (1980) 261-270.

63. L.M. Martyushev, V.D. Selznev, *Physics Reports* 426 (2006) 1 – 45.

64. M. Menndez, D. Morales, L. Pardo, *Statistics & Probability Letters* 34 (1997) 85-93.

65. G.C.Smith, A.K.Livesey, Surface and interface Analysis, Vol. 19, 175-180 (1992.

66. R.P. Vasquez, J.D.Klein, J.J.Barton and F.J.Grunthaner, *Journal of Electron Spectroscopy and Related Phenomena,* 23 (1981) 63-81.

67. G.D. Wilk, R. M. Wallace, and J. M. Anthony, *Journal of Applied Physics*, 89, 5243–5275 (2001).

68. C. Dallera, L. Braicovicha, L. Duo, A. Palenzona, G. Panaccione, G. Paolicelli, B.C.C. Cowie, J. Zegenhagen, *Nuclear Instruments and Methods in Physics Research* A 547 (2005) 113–123, U. Diebold, *Surface Science Reports* 48 (2003) 53-229.

69. W. Drube, Nuclear Instruments and Methods in Physics Research A 547 (2005) 87–97.

70. C.S. Fadley, *Progress in Surface Science,* Vol. 16, pp. 275-388, 1984.

71. C.S. Fadley., Nuclear Instruments and Methods in Physics Research A 601 (2009) 8–31.

72. C.S. Fadley Journal of Electron Spectroscopy and Related Phenomena 178–179 (2010) 2–32.

73. C.G. Jin, Y. Sasaki, K. Okashita, H. Tamura, H. Ito, B. Mizuno, T. Okumura, M. Kobata, J.J. Kim, E. Ikenaga, K. Kobayashi, *Symp. On VLSI Tech.* (2004), 178.

74. K. Kobayashi, Nuclear Instruments and Methods in Physics Research A 601 (2009) 32–47.

75. P. Le Fevre, H. Magnan, D. Chandesris, J. Jupille, S. Bourgeois, A. Barbier, W. Drube, T. Uozumi, A. Kotani, *Nuclear Instruments and Methods in Physics Research A 547* (2005) 176–186.

76. Y. Nakatsu, A. Sekiyama, S. Imada, Y. Okamoto, S. Niitaka, H. Takagi, A. Higashiya, M. Yabashi, K. Tamasaku, T. Ishikawa, and S. Suga, *Physical Review B* 83, 115120 (2011).

77. M. Novák, N. Pauly, A. Dubus, Journal of Electron Spectroscopy and Related Phenomena 185 (2012) 4– 12.

78. Panaccione, G., *Surface Science* 606 (2012) 125–129.

79. C. Weiland, P. Lysaght, J. Price, J. Huang, J.C. Woicik, *Applied Physics Letters* 2012, *101*, 061602.

80. N.S. McIntyre, A.R. Pratt, H. Piao, D. Maybury, S.J. Splinter, *Applied Surface Science* 144–145 _1999. 156–160.

81. C. Weiland, P. Lysaght, J. Price, J. Huang, J.C. Woicik, *Applied Physics Letters* 2012, *101*, 061602.

82. C. Weiland, J. Krajewski, R.Opila, V. Pallem, C.Dussarrat and J. C. Woicik. *Surface and Interface Analysis, v46,6, 407 June* 2014.

83. J.F. Moulder, W.F.W. Stickle, P.E. Sobol, K.D. Bomben, *Handbook of X-ray Photoelectron Spectroscpy*, Perkin Elmer Corp, 1978.

84. B. J. Tyler, D. G. Castner, and B. D. Ratner, *J. Vac. Sci. Technol.* A 7 (3), May/Jun 1989.

85. P.J. Cumpson and M.P. Seah., *Surface and Interface Analysis,* Vol. 18, 345-360 (1992*).*

86. B, Lesiak, J. Zemek, A. Jozwik, *Applied Surface Science* 135, 1998. 318–330.

87. F. Reniersa, Craig Tewell, Journal of Electron Spectroscopy and Related Phenomena 142 (2005) 1–25.

88. N.H. Turner, J.A. Schrelifel, *Anal. Chem.* 1994,66, 163R-185R.

89. M. Mayer, R. Fischer, S. Lindig, U. von Toussaint, R.W. Stark, V. Dose, *Nuclear Instruments and Methods in Physics Research B* 228 (2005) 349–359.

90. E. Filatova, E. Taracheva, G. Shevchenko, A. Sokolov, I. Kozhevniko,S. Yuli, F. Schaefer, and W. Braun, *Phys. Status Solidi B* 246, No. 7, 1454–1458 (2009).

91. B.W. Kempshall, L.A. Giannuzzi, B.I. Prenitzer, F.A. Stevie, S.X. Da. *J. Vac. Sci. Technol. B* 20.1., Jan/Feb 2002.

92. S. Reyntjens, R. Puers, *Micromech. Microeng.* 11 (2001) 287–300.

93. N.L. Bonavito, C.L.Gordon, R.Inguva, G.N.Serafino, R.A.Barnes. *Telematics and Informatics,* Vol. 11, No. 4, pp. 295-308, 1994

94. S.F. Gull and J Skilling, . *IEE Proceedings,* Vol. 131, Pt. F, No. 6, OCTOBER 1984, “Maximum entropy method in image processing”.

95. M. Scorciapino, G. Navarra, B. Elsener and A. Rossi, *J. Phys. Chem. C* 2009, *113,* 21328–21337.

96. A.K. Livesey, G.C. Smith, Journal of Electron Spectroscopy and Related Phenomena 1994, 67, 439.

97. A. Jablonski, C.J. Powell, *Surface Science Reports* 2002, *47*, 33.

98. C.J. Zowell, A. Jablonski, *NIST Electron Inelastic-Mean-Free-Path Database*, National Institute Of Standards And Technology, Gaithersburg, MD**2010**.

99. Y.F. Chen, C.M. Kwei, C.J. Tung, *J. Phys. D: Appl. Phys.* 1992, *25*, 262.

100. T.E. Oliphant, Computing in Science & Engineering 2007, 9, 10.

101. R.W. Paynter, M. Rondeau, Journal of Electron Spectroscopy and Related Phenomena 2011, 184, 43.

102. M.B. TRZHASKOVSKAYA, V.I. NEFEDOV, V.G. YARZHEMSKY, *Atomic Data and Nuclear Data Tables* 2001, *77*, 97.

103. M.B. TRZHASKOVSKAYA, V.I. NEFEDOV, V.G. YARZHEMSKY, *Atomic Data and Nuclear Data Tables* 2002, *82*, 257.

104. B.N. De and J.A. Woolan. *Thin Solid Films,* 193/194 (1990) 312-317.

105. J.M. Conny, C.J.Powell, *Surf. Interface Anal*. 29, 444–459 (2000).

106. F. Esaka, K. Furuya, H. Shimada, M. Imamura, N. Matsubayashi,T. Sato, A. Nishijima, T. Kikuchi, A. Kawana, H. Ichimura *Surface Science* 377-379 (1997) 197-200.

107. V. Likhoshvai, A. Ratushny, Journal of Bioinformatics and Computational Biology, v05, 02b (2007) 521-531.

Appendix A

PYTHON COMPUTER PROGRAMMING

Note: Python is an easy to learn, powerful programming language. It has efficient high-level data structures and a simple but effective approach to object-oriented programming. Python's elegant syntax and dynamic typing, together with its interpreted nature, make it an ideal language for matrix manipulation, scripting and rapid application development in many areas on most platforms.

The Python interpreter and the extensive standard library are freely available in source or binary form for all major platforms from the Python Web site, https://www.python.org/, and **may be freely distributed.** The same site also contains distributions of and pointers to many free third party Python modules, programs and tools, and additional documentation.

Python Program for optimizing VKE data for determining α, maximizing Q and solving for matrix N (concentration depth profile).

```
#### BASIC INSTRUCTIONS: ######
#1. Have properly formatted input and initial model files
#2. Set input and material parameters (lines 5 through 23)
#3. Run script.
# input parameters:
Theta = 85
c_sig = 0.3 #sigma for prior normal distribution - in AC
c_wid = 0.4 #spread for prior concentration values - in eV.  Note, if normal distribution, should be >=4x
c_sigc_den = 0.01 #point density for prior concentration - in eV
c_den = 0.01        #point spacing for concentration distribution
E_sig = 0.5 #sigma for EAL normal distribution - in nm
E_wid = 2. #spreadif for prior EAL values - in nm.  Note, if normal distribution, should be >=4x E_sig
E_den = 0.1 #point spacing for EAL distribution
sig = 0.05 #variance in fit - normal distribution - in atomic concentration
# required modules:
import numpy as np
import os, sys, tkFileDialog
from scipy.stats import norm, mode
import Jons_MEM as MEM
# some functions:
def strip(arr_in):  # strips first column & row from data
```

```
	arr_out = np.empty((np.size(arr_in,axis=0)-1,np.size(arr_in,axis=1)-1))
	for x in range(0,np.size(arr_out,axis=0)):
		for y in range(0,np.size(arr_out,axis=1)):
			arr_out[x,y] = arr_in[x+1,y+1]
	return arr_out
def P_meas(I_step,I_meas,sig):	#normal (continuous) distribution - for probability of I_meas with
given c_mod
	return (1./(sig*np.sqrt(2*np.pi)))*np.exp(-(1./2)*(((I_step-I_meas)/sig)**2))

def intensity(Profs,Lam,Theta):
	ACout = np.empty((np.size(Lam,axis=0),np.size(Profs,axis=1)))
	intout = np.empty(np.shape(ACout))
	for k in range(0,np.size(Lam,axis=0)):
		for j in range(0,np.size(Profs,axis=1)):
			int_sum = 0
			for i in range(0,np.size(Profs,axis=0)):
				int_sum = int_sum+(step_size*Profs[i,j]*np.exp(-
((i+1)*step_size)/(Lam[k,j]*np.sin(Theta*np.pi/180.))))
			intout[k,j] = int_sum
		for j in range(0,np.size(ACout,axis=1)):
			ACout[k,j] = intout[k,j]/np.sum(intout[k,:])
	return ACout
def Uniform(lo,hi,dens):
	n_p = int((hi-lo)/dens)
	points = []
	probs = []
	for p in range(0,n_p):
		points.append(lo+(p*dens))
		probs.append(1./n_p)
	return points,probs
def Normal(mu,sigma,lo,hi,dens):
	n_p = int((hi-lo)/dens)
	points = []
	probs = []
	for p in range(0,n_p):
		points.append(lo+(p*dens))
	pd = norm.pdf(points,loc=mu,scale=sigma)
	for p in range(0,n_p):
		probs.append(pd[p]*dens)
	return points,probs
def Unfit(value):
	return [value], [1.]
# Read data in:
print '\nPlease Open Measured hv vs. Concentration Data'
f_in = tkFileDialog.askopenfilename()
indat = np.genfromtxt(f_in)
I_meas = strip(indat)
f_pref = os.path.splitext(f_in)[0]
print 'You opened: ',f_pref
hv = []
for k in range(1,np.size(indat,axis=0)):
	hv.append(indat[k,0])
```

```
BE = []
for j in range(1,np.size(indat,axis=1)):
        BE.append(indat[0,j])
n_spec = len(BE)
n_hv = len(hv)
# Kinetic energy array:
KE = np.empty((n_hv,n_spec))
for k in range(0,n_hv):
        for j in range(0,n_spec):
                KE[k,j] = hv[k]-BE[j]
# read starting profile:
print '\nPlease Open Depth Profile from MEM'
start_f = tkFileDialog.askopenfilename()
start_arr = np.genfromtxt(start_f)
directory = os.path.split(start_f)[1]
print '\nYou opened: ', directory
#Check that columns from Measured data and MEM match
start_arr = MEM.column_Check(BE,start_arr)
start_in = strip(start_arr)
f_in2 = os.path.splitext(start_f)[0]
print 'You opened: ',f_in2
n_slab = np.size(start_in,axis=0)    #number of slabs for calc - for easier typing
#initialize E working arrays:
# EAL array from MEM
print '\nPlease open EAL File from MEM'
EAL_File=tkFileDialog.askopenfilename()
EAL_Array = np.genfromtxt(EAL_File)
E_in = strip(EAL_Array)
print 'You opened: ', os.path.split(EAL_File)[1]
#Retrieve step size in nm
step_size = input('\nWhat step size for the depth profile(nm)?: ')
E_prior = np.empty((n_hv,n_spec),dtype='object')
E_prob = np.empty((n_hv,n_spec),dtype='object')
for k in range(0,n_hv):
        for j in range(0,n_spec):
                Elo = E_in[k,j]-(E_wid/2)
                if Elo <= 0:
                        Elo = 0.00001
                Ehi = E_in[k,j]+(E_wid/2)
                E_prior[k,j] = Normal(E_in[k,j],E_sig,Elo,Ehi,E_den)[0]
                E_name = str('in_EAL_'+str(k)+'_'+str(j))
                E_p_out = np.empty((len(E_prior[k,j]),2))
                for p in range(0,np.size(E_p_out,axis=0)):
                        E_p_out[p,0] = E_prior[k,j][p]
                        E_p_out[p,1] = P_meas(E_prior[k,j][p],E_in[k,j],E_sig)
# np.savetxt(E_name,E_p_out)
#Ask for number of iterations for calculation
n_step = input('\nHow many number of iterations?: ')
E_0 = np.empty(np.shape(E_prior))
E_out = np.empty((n_hv+1,n_spec+1))
E_trace = np.empty(np.shape(E_prior),dtype='object')
for k in range(0,n_hv):
```

```
		for j in range(0,n_spec):
			E_trace[k,j] = np.empty((1,n_step))
#make initial E_0
aE = np.empty((n_hv,n_spec),dtype='int')	#see c0 initialization
for j in range(0,n_spec):
		for k in range(0,n_hv):
			aE[k,j] = int(len(E_prior[k,j])*np.random.rand())
			E_0[k,j] = E_prior[k,j][aE[k,j]]
aE0 = np.array(aE)
E_working = np.array(E_0)
## Define variables ('Priors')
# prior concentrations:
c_prior = np.empty((n_slab,n_spec),dtype='object')
c_prob = np.empty((n_slab,n_spec),dtype='object')
for i in range(0,np.size(start_in,axis=0)):
		for j in range(0,np.size(start_in,axis=1)):
			lo = start_in[i,j]-(c_wid/2)
#			if lo < 0.:
#				lo = 0.
			hi = start_in[i,j]+(c_wid/2)
#		if hi > 1.:
#		hi = 1.
			c_prior[i,j] = Normal(start_in[i,j],c_sig,lo,hi,c_den)[0]
			prior_name = str('in_c_'+str(i)+'_'+str(j))	#file name to write out prior histograms
			prior_out = np.empty((len(c_prior[i,j]),2))
			for p in range(0,np.size(prior_out,axis=0)):
				prior_out[p,0] = c_prior[i,j][p]
				prior_out[p,1] = P_meas(c_prior[i,j][p],start_in[i,j],c_sig)
# np.savetxt(prior_name,prior_out)
#initialize c working arrays:
c_0 = np.empty(np.shape(c_prior))
c_out = np.empty((n_slab+1,n_spec+1))
c_trace = np.empty(np.shape(c_prior),dtype='object')
for i in range (0,n_slab):
		for j in range(0,n_spec):
			c_trace[i,j] = np.empty((1,n_step))
# make initial c_0
a = np.empty((n_slab,n_spec),dtype=int)	#need ixj array of a to keep same register
for i in range(0,n_slab):
		for j in range(0,n_spec):
			a[i,j] = int(len(c_prior[i,j])*np.random.rand())
			c_0[i,j] = c_prior[i,j][a[i,j]]
		c0_sum = np.sum(c_0[i,:])
		for j in range(0,n_spec):
			c_0[i,j] = c_0[i,j]/c0_sum
a0 = np.array(a)	#think I need this to keep register
c_working = np.array(c_0)
# Initial intensity and probability:
I_0 = intensity(c_0,E_0,Theta)
I_step = np.array(I_0)	#Initial working intensity
c0_prob = 1
E0_prob = 1
```

```
P_0 = 1
for j in range(0,n_spec):
    for i in range(0,n_slab):
        c0_prob = c0_prob*P_meas(c_0[i,j],start_in[i,j],c_sig)
    for k in range(0,n_hv):
        E0_prob = E0_prob*P_meas(E_0[k,j],E_in[k,j],E_sig)
        P_0 = P_0*P_meas(I_0[k,j],I_meas[k,j],sig)
P_0 = c0_prob*E0_prob*P_0
# here is the MCMC:
P_arr = np.empty((n_step+1,2))
P_arr[0,0] = 0
P_arr[0,1] = P_0
sys.stdout.write('start\n')
for step in range(0,n_step):
    sys.stdout.flush()
    write_str = str(str(step+1)+' of '+str(n_step)+' steps completed.\r')
    sys.stdout.write(write_str)
    for i in range(0,n_slab):
        for j in range(0,n_spec):
            t = np.random.rand()
            if t < 1./3:
                a[i,j] = a0[i,j]-1
                if a[i,j] < 0:
                    a[i,j] = 0.00001
            elif 1./3 <= t < 2./3:
                a[i,j] = a0[i,j]
            else:
                a[i,j] = a0[i,j]+1
                if a[i,j] >= len(c_prior[i,j]):
                    a[i,j] = len(c_prior[i,j])-1
            c_working[i,j] = c_prior[i,j][a[i,j]]
            for k in range(0,n_hv):
                tE = np.random.rand()
                if tE < 1./3:
                    aE[k,j] = aE0[k,j]-1
                    if aE[k,j] < 0:
                        aE[k,j] = 0.00001
                elif 1./3 <= tE < 2./3:
                    aE[k,j] = aE0[k,j]
                else:
                    aE[k,j] = aE0[k,j]+1
                    if aE[k,j] >= len(E_prior[k,j]):
                        aE[k,j] = len(E_prior[k,j])-2
                E_working[k,j] = E_prior[k,j][aE[k,j]]
    for i in range(0,n_slab):
        c_sum = np.sum(c_working[i,:])
        for j in range(0,n_spec):
            c_working[i,j] = c_working[i,j]/c_sum
    for k in range(0,n_hv):
        for j in range(0,n_spec):
            for i in range(0,n_slab):
```

```
                                        I_step[k,j] = I_0[k,j]+(c_working[i,j]*np.exp(-
((i+1)*step_size)/(E_working[k,j]*Theta)))-(c_0[i,j]*np.exp(-((i+1)*step_size)/(E_0[k,j]*Theta)))
        E_prob = 1
        c_prob = 1
        I_prob = 1
        for j in range(0,n_spec):
                for i in range(0,n_slab):
                        c_prob = c_prob*P_meas(c_working[i,j],start_in[i,j],c_sig)
                for k in range(0,n_hv):
                        E_prob = E_prob*P_meas(E_working[k,j],E_in[k,j],E_sig)
                        I_prob = I_prob*P_meas(I_step[k,j],I_meas[k,j],sig)
        P_step = I_prob*c_prob*E_prob
        P_test = P_step/P_0
        if P_test >= np.random.rand():
                E_0 = np.array(E_working)
                aE0 = np.array(aE)
                c_0 = np.array(c_working)
                a0 = np.array(a)
                P_0 = P_step
                I_0 = np.array(I_step)
        for j in range(0,n_spec):
                for i in range(0,n_slab):
                        c_trace[i,j][0,step] = c_0[i,j]
                for k in range(0,n_hv):
                        E_trace[k,j][0,step] = np.array(E_0[k,j])
        P_arr[step+1,0] = step+1
        P_arr[step+1,1] = P_0
#np.savetxt('P_trace',P_arr)
c_out[0,0] = n_spec
for i in range(0,n_slab):
        c_out[i+1,0] = (i)*step_size
        for j in range(0,n_spec):
                c_out[0,j+1] = BE[j]
#               c_out[i+1,j+1] = mode(c_trace[i,j][0,:])[0][0]
#               c_out[i+1,j+1] = np.median(c_trace[i,j])
                c_out[i+1,j+1] = np.average(c_trace[i,j])
                if c_out[i+1,j+1] < 0:
                        c_out[i+1,j+1] = 0.00001
                elif c_out[i+1,j+1] > 1:
                        c_out[i+1,j+1] = 1
        c_sum = np.sum(c_out[i+1,1:])
        for j in range(0,n_spec):
                c_out[i+1,j+1] = c_out[i+1,j+1]/c_sum
                c_hist,c_bins = np.histogram(c_trace[i,j],range=(-0.5,1.5),bins=200,density=True)
                c_hist_out = np.empty((200,2))
                for x in range(0,200):
                        c_hist_out[x,0] = c_bins[x]
                        c_hist_out[x,1] = c_hist[x]
                c_f_name = str('c_'+str(i)+'_'+str(j))
                c_trace_name = str('tr_c_'+str(i)+'_'+str(j))
                c_tr_arr = np.empty((n_step,2))
                for st in range(0,n_step):
```

```
                    c_tr_arr[st,0] = st+1
                    c_tr_arr[st,1] = c_trace[i,j][0,st]
#               np.savetxt(c_trace_name,c_tr_arr)
#               np.savetxt(c_f_name,c_hist_out)
E_out[0,0] = n_spec
for k in range(0,n_hv):
        E_out[k+1,0] = hv[k]
        for j in range(0,n_spec):
                E_out[0,j+1] = BE[j]
#               E_out[k+1,j+1] = mode(E_trace[k,j][0,:])[0][0]
#               E_out[k+1,j+1] = np.median(E_trace[k,j])
                E_out[k+1,j+1] = np.average(E_trace[k,j])
                E_hist,E_bins = np.histogram(E_trace[k,j],bins=50,density=True)
                E_hist_out = np.empty((50,2))
                for x in range(0,50):
                        E_hist_out[x,0] = E_bins[x]
                        E_hist_out[x,1] = E_hist[x]
                E_f_name = str('EAL_'+str(k)+'_'+str(j))
                E_trace_name = str('tr_EAL_'+str(k)+'_'+str(j))
                E_tr_arr = np.empty((n_step,2))
                for st in range(0,n_step):
                        E_tr_arr[st,0] = st+1
                        E_tr_arr[st,1] = E_trace[k,j][0,st]
#               np.savetxt(E_trace_name,E_tr_arr)
#               np.savetxt(E_f_name,E_hist_out)
vke_out = np.empty((n_hv+1,n_spec+1))
res_vke = intensity(strip(c_out),strip(E_out),Theta)
for k in range(0,n_hv):
        vke_out[k+1,0] = hv[k]
        for j in range(0,n_spec):
                vke_out[0,j+1] = BE[j]
                vke_out[k+1,j+1] = res_vke[k,j]
file_name = directory+'_'+str(n_step)+'it'
#np.savetxt('EAL_out.dat',E_out)
np.savetxt(file_name+'.dep',c_out)
#np.savetxt('result.vke',vke_out)
sys.stdout.write('\nDone\n')
sys.exit()
```

Appendix B

PERMISSION E-MAIL TO RE-USE DATA AND FIGURES

Permission request to re-use in my dissertation the data from our paper published in Surface and Interface Analysis in 2014.

From: Conan Weiland conan.weiland@gmail.com
Sent; Thur 5/12/2016 3:20 PM
To: Krajewski, James J <James.J.Krajewski@questdiagnostics.com>

J.J Krajewski,

I hereby grant permission for re-use of data and figures from our publication "Nondestructive compositional depth profiling using variable kinetic energy hard x-ray photoelectron spectroscopy and maximum entropy regularization" published in Surface and Interface Analysis in 2014.

Conan Weiland

My request to Conan Weiland, a co-author:

On Thu, May 12, 2016 at 8:34 AM, Krajewski, James J <James.J.Krajewski@questdiagnostics.com> wrote:

Conan,

I am in the final stages of writing my dissertation and I am using some of the data we published back in 2014 on the work we did at Brookhaven for the "Non-destructive XPS…" paper.

I am requesting your permission to use some of the data from our paper and adding all of the alternate thin film techniques I did to complete my dissertation.

Since I'm not first author on the paper, can you send me a permission letter (email) stating that I have your permission to use the data from our paper?

I greatly appreciate it.

Best regards,

J.J. Krajewski